

DESIGN AND CHARACTERISATION OF BROADBAND  
MICROSTRIP REFLECTARRAY ANTENNAS

PHUA YEONG NAN

DOCTOR OF PHILOSOPHY (ENGINEERING)

LEE KONG CHIAN FACULTY OF ENGINEERING AND  
SCIENCE  
UNIVERSITI TUNKU ABDUL RAHMAN  
APR 2023

**DESIGN AND CHARACTERISATION OF BROADBAND  
MICROSTRIP REFLECTARRAY ANTENNAS**

**By**

**PHUA YEONG NAN**

A dissertation submitted to the Department of Electrical and Electronics  
Engineering,  
Lee Kong Chian Faculty of Engineering and Science,  
Universiti Tunku Abdul Rahman,  
in partial fulfillment of the requirements for the degree of  
Doctor of Philosophy (Engineering)  
April 2023

## **ABSTRACT**

### **DESIGN AND CHARACTERISATION OF BROADBAND MICROSTRIP REFLECTARRAY ANTENNAS**

**Phua Yeong Nan**

Microstrip reflectarray antennas have the advantages of having a low profile, low loss, and low production cost, making them suitable for high gain and wide bandwidth operation for long-distance communication. However, utilizing the conventional microstrip reflectarray elements such as the rectangular or circular patch elements is difficult to achieve the desired performances. The inherent narrow bandwidth and limited turning ability in such elements have made it difficult to achieve a smooth phase range and broadband reflectarray performance. In this dissertation, three improved designs have been formulated to overcome the mentioned limitations.

The first method comprises the usage of a dumbbell-shaped square ring, combined with the Vivaldi tapered slot antenna, which is used to design a broadband reflectarray for the first time. The use of the travelling-wave radiator has enabled the proposed reflectarray element to achieve a full phase range of  $371^\circ$  and a low phase sensitivity of  $64.6^\circ/\text{mm}$  simultaneously. A  $13 \times 13$  linearly polarized reflectarray is designed and fabricated. Measurement results show an antenna gain of 24.1 dBi with a -1-dB gain bandwidth of 10.6%, and its corresponding aperture efficiency of 40.4% is achievable at the centre frequency of 6.5 GHz.

Next, a single-layer circular patch loaded with two unequal slots is designed to enhance the phase tuning ability and achieved a smooth phase range of  $458^\circ$ . A low profile  $13 \times 13$  linearly polarized reflectarray is designed and fabricated. Measurement results show that an antenna gain of 23.4 dBi is realizable at the centre frequency of 9.3 GHz with an aperture efficiency of 42%. The -1-dB gain bandwidth of 11.8% has shown much improvement compared to the first design.

The third design is a double-layer reflectarray element built using two closely coupled inter-layer ring-patches to improve the phase tuning ability and enhance the broad bandwidth performance. Due to the tight coupling between the inter-layer patches, the coupling between the adjacent reflectarray elements can be significantly minimised. A linear and broad phase range of  $527^\circ$  is achievable, and a  $13 \times 13$  linearly polarized reflectarray is designed and fabricated. Measurement results show an antenna gain of 23.6 dBi at the centre frequency of 9.3 GHz with an aperture efficiency of 43.8%. The reflectarray features a broad -1-dB gain bandwidth of 33.2%.

In conclusion, three unique designs have been demonstrated to overcome the narrow bandwidth of the reflectarray element by improving both the range and linearity of the reflection phase as well as the phase tuning ability. These designs can be employed to design full-fledged reflectarrays and enable wide bandwidth performance.

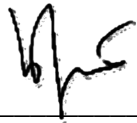
## **ACKNOWLEDGEMENTS**

First of all, I would like to express my sincere gratitude to my supervisor, Prof. Dr. Lim Eng Hock and co-supervisor, Prof. Ir. Dr. Chung Boon Kuan, for spending their precious time discussing with me and guiding me throughout my PhD study. Their valuable advice, guidance and constructive suggestions have contributed to my successful research completion. Also, I would like to thank my family for their love, devotion and understanding. Last but not least, I would like to express my utmost gratitude to Universiti Tunku Abdul Rahman (UTAR) for the encouragement and support in completing my research.

## APPROVAL SHEET

This dissertation/thesis entitled “**DESIGN AND CHARACTERISATION OF BROADBAND MICROSTRIP REFLECTARRAY ANTENNAS**” was prepared by PHUA YEONG NAN and submitted as partial fulfilment of the requirements for the degree of Doctor of Philosophy (Engineering) at Universiti Tunku Abdul Rahman.

Approved by:



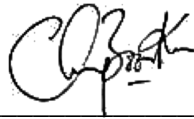
---

(Prof. Dr. Lim Eng Hock)

Date: ..7 April 2023.....

Supervisor

Department of Electrical and Electronic Engineering  
Lee Kong Chian Faculty of Engineering and Science  
Universiti Tunku Abdul Rahman



---

(Prof. Ir. Dr. Chung Boon Kuan)

Date: ..7 April 2023.....

Co-supervisor

Department of Electrical and Electronic Engineering  
Lee Kong Chian Faculty of Engineering and Science  
Universiti Tunku Abdul Rahman

**LEE KONG CHIAN FACULTY OF ENGINEERING AND SCIENCE**  
**UNIVERSITI TUNKU ABDUL RAHMAN**

Date: 7 April 2023

**SUBMISSION OF THESIS**

It is hereby certified that PHUA YEONG NAN (ID No: 15UED01253) has completed this thesis entitled “DESIGN AND CHARACTERISATION OF BROADBAND MICROSTRIP REFLECTARRAY ANTENNAS” under the supervision of Prof. Dr. Lim Eng Hock (Supervisor) from the Department of Electrical and Electronic Engineering, Lee Kong Chian Faculty of Engineering and Science (LKC FES), and Prof. Ir. Dr. Chung Boon Kuan (Co-Supervisor) from the Department of Electrical and Electronic Engineering, Lee Kong Chian Faculty of Engineering and Science (LKC FES).

I understand that University will upload softcopy of my dissertation in pdf format into UTAR Institutional Repository, which may be made accessible to UTAR community and public.

Yours truly,




---

(PHUA YEONG NAN)

## DECLARATION

I hereby declare that the dissertation is based on my original work except for quotations and citations which have been duly acknowledged. I also declare that it has not been previously or concurrently submitted for any other degree at UTAR or other institutions.

Name  \_\_\_\_\_  
(PHUA YEONG NAN)

Date 7 April 2023



## TABLE OF CONTENTS

	<b>Page</b>
<b>ABSTRACT</b>	<b>ii</b>
<b>ACKNOWLEDGEMENTS</b>	<b>iv</b>
<b>APPROVAL SHEET</b>	<b>v</b>
<b>SUBMISSION OF THESIS</b>	<b>vi</b>
<b>DECLARATION</b>	<b>vii</b>
<b>LIST OF TABLES</b>	<b>xi</b>
<b>LIST OF FIGURES</b>	<b>xii</b>
<b>1 INTRODUCTION</b>	<b>1</b>
1.1 Background and Issue	1
1.2 Development of Reflectarray	4
1.3 Broadband Reflectarray Challenges	7
1.4 Problem Statement	9
1.5 Objectives	10
1.6 Publications	12
1.7 Thesis Overview	13
<b>2 LITERATURE REVIEW, REFLECTARRAY THEORY AND DESIGN</b>	<b>14</b>
2.1 Literature review	14
2.2 Design of Reflectarray	18
2.3 Feed Model	19
2.4 Aperture Efficiency	21
2.4.1 Efficiency Model: Geometrical Parameters Definition	23
2.4.2 Spillover Efficiency	25
2.4.3 Illumination Efficiency	26
2.4.4 Effects of Configuration Parameters on the Efficiencies Factors	28

2.5	Radiation Pattern: Array-Theory Method	32
2.6	Phase Shift Distribution	35
2.7	Element Phase Tuning Methodology	39
2.8	Element Modelling Techniques	39
2.9	Element Reflection Phase Curve	41
2.10	Element Design Consideration	43
2.11	Conclusion	46
<b>3</b>	<b>DESIGN METHODOLOGY</b>	<b>47</b>
3.1	Design Method	47
3.2	Unit Element Design	49
3.3	Reflectarray Configuration Design	53
3.4	Measurement Method	57
3.5	Conclusion	59
<b>4</b>	<b>VIVALDI TAPERED SLOT REFLECTARRAY LOADED WITH DUMBBELL-SHAPED RING RESONATOR</b>	<b>60</b>
4.1	Introduction	60
4.2	Reflectarray Unit Element	61
4.3	Reflectarray Design Configuration	69
4.4	Results and Discussion	74
4.5	Parametric Analysis	77
4.5.1	Unit Element Reflection Phase	77
4.5.2	Reflectarray Performance	84
4.6	Comparative Study	88
4.7	Conclusion	89
<b>5</b>	<b>SINGLE-LAYER BROADBAND REFLECTARRAY USING CIRCULAR MICROSTRIP PATCH LOADED WITH TWO UNEQUAL SLOTS</b>	<b>90</b>
5.1	Introduction	90
5.2	Reflectarray Unit Element	91
5.3	Reflectarray Design Configuration	98

5.4	Results and Discussion	103
5.5	Parametric Analysis	106
5.5.1	Unit Element Reflection Phase	106
5.5.2	Reflectarray Performance	112
5.6	Comparative Study	116
5.7	Conclusion	118
<b>6</b>	<b>BROADBAND REFLECTARRAY WITH CLOSELY COUPLED INTER-LAYER CIRCULAR RING-PATCHES</b>	<b>119</b>
6.1	Introduction	119
6.2	Reflectarray Unit Element Design and Analysis	120
6.3	Reflectarray Design Configuration and Analysis	131
6.4	Results and Discussion	135
6.5	Parametric Analysis	138
6.5.1	Unit Element Reflection Phase	138
6.5.2	Reflectarray Performance	140
6.6	Comparative Study	144
6.7	Conclusion	146
<b>7</b>	<b>CONCLUSIONS</b>	<b>147</b>
7.1	Summary	147
7.2	Future Work	150
	<b>REFERENCES</b>	<b>152</b>

## LIST OF TABLES

<b>Table</b>		<b>Page</b>
Table 2.1:	Configuration Parameters.	24
Table 4.1:	Design Parameters.	63
Table 4.2:	Comparison of the Proposed Reflectarray with Other Works.	88
Table 5.1:	Design Parameters.	93
Table 5.2:	Comparison of the Proposed Reflectarray with Other Works.	117
Table 6.1:	Design Parameters.	123
Table 6.2:	Comparison of the Proposed Reflectarray Performance with Other Published Designs.	145

## LIST OF FIGURES

Figure		Page
Figure 1.1:	Conventional reflector antenna (Balanis, 2005).	1
Figure 1.2:	Phased array antenna (Mailloux, 2005).	2
Figure 1.3:	Overall geometric of reflectarray antenna.	3
Figure 1.4:	Configuration of an offset-fed reflectarray.	5
Figure 1.5:	Different types of reflectarray elements. (a) variable-size patches, (b) variable-length phase delay lines, (c) variable-size loops or rings, and (d) variable angular rotations.	6
Figure 2.1:	Coordinates representation of the reflectarray aperture and feeding antenna.	19
Figure 2.2:	The feed radiation pattern for different $q$ -factors.	21
Figure 2.3:	Gain as a function of the aperture efficiency and electrical size of the reflectarray.	22
Figure 2.4:	Configuration parameters and Cartesian coordinate of a reflectarray antenna.	24
Figure 2.5:	Effects of offset angle $\theta_i$ on the efficiencies at $F/D = 0.65$ .	30
Figure 2.6:	Effects of $F/D$ ratio on the efficiencies at an offset angle $\theta_i = 20^\circ$ .	30
Figure 2.7:	2D plot of aperture efficiency varying with $q$ -factor and $F/D$ ratio at an offset angle of $20^\circ$ .	31
Figure 2.8:	Coordinate representation of a reflectarray antenna.	32
Figure 2.9:	Normalised radiation pattern of a $13 \times 13$ reflectarray.	35
Figure 2.10:	Geometrical representation of a reflectarray antenna.	36

Figure 2.11:	Example of the required phase distribution in a square reflectarray. (a) Normal feed and (b) Offset feed.	38
Figure 2.12:	3D model of Floquet cell with a $y$ -polarized electric field excitation.	40
Figure 2.13:	Typical reflection coefficient of a reflectarray element as a function of the geometrical parameter change. (a) Reflection phase, $\angle\Gamma$ , and (b) Reflection magnitude, $ \Gamma $ .	42
Figure 3.1:	Design flow of a reflectarray antenna.	48
Figure 3.2:	Square patch unit element.	50
Figure 3.3:	Unit cell model in CST Microwave Studio. (a) Square patch unit element in a bounding box. (b) Floquet port with de-embedding onto the element surface. (c) Linearly polarized plane wave incident on the element. (d) Floquet cell boundaries.	50
Figure 3.4:	Flow chart for the $S_{11}$ parameter post-processing.	51
Figure 3.5:	$S_{11}$ parameter results and post-processed reflection responses vs phase-shifting parameter at the frequency of 10 GHz. (a) Reflection phase, and (b) reflection amplitude.	52
Figure 3.6:	Side view of a reflectarray configuration.	53
Figure 3.7:	Flow chart of the phase map generation and construction of a 3D reflectarray model in CST Microwave Studio®.	54
Figure 3.8:	$13 \times 13$ grid layout for the arrays.	55
Figure 3.9:	Full 3D reflectarray model.	56
Figure 3.10:	Measurement setup for a reflectarray.	58
Figure 3.11:	3D view of the farfield radiation in the CST Microwave Studio®.	58
Figure 4.1:	(a) Exploded view of the proposed unit element, and (b) top and bottom views of the Vivaldi tapered slot antenna loaded with a dumbbell-shaped microstrip ring resonator.	63

Figure 4.2:	Simulation model of the Vivaldi tapered slot unit element in a Floquet cell.	64
Figure 4.3:	Reflection amplitude and phase responses as a function of ring width $W_r$ for different wave frequencies at the incident angle of $\theta_i = 20^\circ$ .	66
Figure 4.4:	Reflection amplitude and phase responses for different incident angles ( $\theta_i$ ) at $f_o = 6.5$ GHz.	66
Figure 4.5:	(a) Electric field and (b) surface current distributions on the dumbbell-shaped microstrip ring resonator; (c) Electric field and (b) surface current distributions on the Vivaldi tapered slot antenna at 6.5 GHz, for the ring width of $W_r = 4.4$ mm.	68
Figure 4.6:	(a) Side view of the proposed reflectarray with a feeding horn suspended at $\theta_i$ . (b) Simulation model of the full-fledged reflectarray in CST Microwave Studio <sup>®</sup> .	70
Figure 4.7:	Simulation model of C-band pyramidal horn antenna.	71
Figure 4.8:	A 3D farfield plot of the C-band pyramidal horn antenna.	71
Figure 4.9:	Radiation patterns of the C-band pyramidal horn antenna: 2D and cosine- $q$ model.	71
Figure 4.10:	Phase distributions on the proposed reflectarray.	73
Figure 4.11:	Prototype of the proposed reflectarray viewed from different directions. (a) dumbbell-shaped microstrip ring resonator, (b) Vivaldi tapered slot antenna, and (c) top view of the prototype attached to the rotating table.	74
Figure 4.12:	Measured and simulated (a) $E$ - and (b) $H$ - plane radiation patterns of the proposed reflectarray at 6.6 GHz.	75
Figure 4.13:	Measured and simulated radiation gains and aperture efficiencies of the proposed reflectarray as a function of frequency.	76
Figure 4.14:	Effect of total height $h$ on the reflection amplitude and phase responses at the incident angles $\theta_i = 20^\circ$ and $f_o = 6.5$ GHz.	79

Figure 4.15:	Effect of backwall offset distance $L_g$ on the reflection amplitude and phase responses at the incident angles $\theta_i = 20^\circ$ and $f_o = 6.5$ GHz.	79
Figure 4.16:	Effect of circular slot cavity diameter $D_{SL}$ on the reflection amplitude and phase responses at the incident angles $\theta_i = 20^\circ$ and $f_o = 6.5$ GHz.	80
Figure 4.17:	Effect of tapering rate $R$ on the reflection amplitude and phase responses at the incident angles $\theta_i = 20^\circ$ and $f_o = 6.5$ GHz.	81
Figure 4.18:	Effect of opening $H$ on the reflection amplitude and phase responses at the incident angles $\theta_i = 20^\circ$ and $f_o = 6.5$ GHz.	81
Figure 4.19:	Effect of separation gap $d_s$ on the reflection amplitude and phase responses at the incident angles $\theta_i = 20^\circ$ and $f_o = 6.5$ GHz.	82
Figure 4.20:	Wave incident angles $\theta_{i,L}$ and $\theta_{i,R}$ in $xz$ -plane.	83
Figure 4.21:	Effect of opposite wave incident angles $\theta_{i,R}$ on the reflection amplitude and phase responses at $f_o = 6.5$ GHz.	83
Figure 4.22:	Simulated radiation gains of the proposed reflectarray for different feeding angles ( $\theta_i$ ).	84
Figure 4.23:	Radiation patterns of the proposed reflectarray at 6.6 GHz for different feeding angles ( $\theta_i$ ). (a) $E$ - and (b) $H$ - planes.	85
Figure 4.24:	Simulated radiation gains of the proposed reflectarray for different feeding angles ( $\theta_i$ ).	86
Figure 4.25:	Radiation patterns of the proposed reflectarray at 6.6 GHz for different feeding angles ( $\theta_i$ ). (a) $E$ - and (b) $H$ - planes.	87
Figure 5.1:	(a) The proposed unit element. (b) Simulation model of the unit element in a Floquet cell.	92
Figure 5.2:	Reflection phase response of the proposed unit element at $f_o = 9.0$ GHz for different slot length ratios $\xi$ at $\theta_i = 20^\circ$ .	94
Figure 5.3:	Reflection amplitude and phase responses of the proposed unit element as a function of patch radius $R_p$ . (a) Different wave frequencies at $\theta_i =$	



	20°. (b) Different incident angles $\theta_i$ at $f_o = 9.0$ GHz.	95
Figure 5.4:	Current distributions for the cases of (a) $w_t = 8.0$ mm, $S_1 = 0.0$ mm, $S_2 = 0.0$ mm; (b) $w_t = 6.0$ mm, $S_1 = 2.0$ mm, $S_2 = 0.0$ mm; (c) $w_t = 3.0$ mm, $S_1 = 3.4$ mm, $S_2 = 1.6$ mm; (d) $w_t = 0.5$ mm, $S_1 = 4.8$ mm, $S_2 = 2.7$ mm.	97
Figure 5.5:	(a) Side view of the proposed reflectarray with a feeding horn suspended at $\theta_i$ . (b) Simulation model of the reflectarray in CST Microwave Studio®.	99
Figure 5.6:	Simulation model of X-band pyramidal horn antenna.	100
Figure 5.7:	A 3D farfield plot of the pyramidal horn antenna.	100
Figure 5.8:	Radiation patterns of the X-band pyramidal horn antenna: 2D and cosine- $q$ model.	100
Figure 5.9:	(a) Phase distributions on the proposed reflectarray.	101
Figure 5.10:	Prototype of the proposed reflectarray viewed from different directions. (a) Front view, (b) Side view, and (c) side view of the prototype attached to the rotating table.	102
Figure 5.11:	Measured and simulated (a) $E$ - and (b) $H$ - plane radiation patterns of the proposed reflectarray at 9.3 GHz.	105
Figure 5.12:	Measured and simulated antenna gains of the proposed reflectarray as a function of frequency.	105
Figure 5.13:	Effect of $\xi$ on the reflection amplitude and phase responses at $f_o = 9.0$ GHz and $\theta_i = 20^\circ$ ( $h = 5.7$ mm, $w_s = 0.5$ mm, $w_t = 0.5$ mm).	108
Figure 5.14:	Effect of $w_s$ and $w_t$ on the reflection amplitude and phase responses at $f_o = 9.0$ GHz and $\theta_i = 20^\circ$ . (a) $h = 5.7$ mm, $\xi = -0.2$ , $w_t = 0.5$ mm. (b) $h = 5.7$ mm, $\xi = -0.2$ , $w_s = 0.5$ mm.	109
Figure 5.15:	Effect of $h$ on the reflection amplitude and phase responses at $f_o = 9.0$ GHz and $\theta_i = 20^\circ$ ( $\xi = -0.2$ , $w_s = 0.5$ mm).	109

Figure 5.16:	Wave incident at $\theta_i$ ( $xz$ -plane) and $\varphi_i$ ( $yz$ -plane) orientations.	110
Figure 5.17:	Effect of incident angles on the reflection amplitude and phase responses of the proposed unit element at $f_o = 9.0$ GHz. (a) $\theta_{i,R}$ in $xz$ -plane orientation, (b) $\varphi_{i,u}$ in $yz$ -plane orientation and (c) comparison for $\theta_i = 20^\circ$ in $xz$ -plane and $\varphi_i = 20^\circ$ in $yz$ -plane.	112
Figure 5.18:	Simulated (a) $E$ - and (b) $H$ - plane radiation patterns of the reflectarray at 9.3 GHz for different incident angles.	113
Figure 5.19:	Simulated antenna gains of the reflectarray as a function of frequency for different incident angles.	114
Figure 5.20:	Simulated (a) $E$ - and (b) $H$ - plane radiation patterns of the reflectarray at 9.3 GHz for different $F/D$ ratios.	115
Figure 5.21:	Simulated antenna gains of the reflectarray as a function of frequency for different $F/D$ ratios.	116
Figure 6.1:	Simulation model of the unit element in a Floquet cell.	121
Figure 6.2:	(a) The proposed unit element, (b) layouts, and (c) cross-sectional view of the top and bottom circular ring-patches.	122
Figure 6.3:	Reflection phase responses as a function of $\rho_{ur}$ at different frequencies: (a) 8.4 GHz, (b) 9.2 and (c) 12.1 GHz.	125
Figure 6.4:	Mean phase difference $\overline{\delta\varphi}$ and maximum reflection amplitude for different combinations of $(c_{u1}, c_{d1})$ .	126
Figure 6.5:	Mean phase difference $\overline{\delta\varphi}$ and maximum reflection amplitude for different values of $c_{d1}$ .	127
Figure 6.6:	Mean phase difference $\overline{\delta\varphi}$ and maximum reflection amplitude for different values of $\Delta$ .	128
Figure 6.7:	Reflection amplitude and phase responses of the proposed unit element for different frequencies at $\theta_i = 15^\circ$ .	129

Figure 6.8:	Electric field distributions (side and top views) of the radiating element at $f_o = 9.2$ GHz. (a) $\rho_{ur} = 0.66$ and (b) $\rho_{ur} = 0.9$ .	130
Figure 6.9:	(a) Side view of the proposed reflectarray with a feeding horn suspended at $\theta_i$ . (b) Simulation model of the reflectarray in CST Microwave Studio <sup>®</sup> , and (c) front, back, and side views of the fabricated prototype.	132
Figure 6.10:	(a) The required phase distributions at $f_o = 9.2$ GHz. Phase difference of each unit element at (b) $f_i = 9.0$ GHz, and (c) $f_i = 12.1$ GHz, with reference to the design frequency of $f_o = 9.2$ GHz.	134
Figure 6.11:	Measured and simulated (a) $E$ - and (b) $H$ -plane radiation patterns of the proposed reflectarray at 9.2 GHz.	136
Figure 6.12:	Measured and simulated antenna gains of the proposed reflectarray as a function of frequency.	137
Figure 6.13:	Effect of different incident angles ( $\theta_i$ ) on the reflection phase responses at $f_o = 9.2$ GHz.	139
Figure 6.14:	Effect of varying slot width, $S_w$ on the reflection phase responses at $f_o = 9.2$ GHz.	139
Figure 6.15:	Effect of the air layer $h$ on the reflection amplitude and phase responses at $f_o = 9.2$ GHz.	140
Figure 6.16:	Simulated (a) $E$ - and (b) $H$ - plane radiation patterns of the proposed reflectarray at 9.2 GHz for different incident angles.	142
Figure 6.17:	Simulated antenna gains of the proposed reflectarray as a function of frequency for different incident angles.	142
Figure 6.18:	Simulated (a) $E$ - and (b) $H$ - plane radiation patterns of the proposed reflectarray at 9.2 GHz for different $F/D$ ratios.	143
Figure 6.19:	Simulated antenna gains of the proposed reflectarray as a function of frequency for different $F/D$ ratios.	144

# CHAPTER 1

## INTRODUCTION

### 1.1 Background and Issue

High-gain antennas such as reflectors and phased arrays are the primary choices in long-distance wireless communication. Reflector antennas have been used extensively due to their high directivity and low loss, as shown in Figure 1.1. However, due to its parabolically surface, it often requires expensive customised fabrication. The parabolic reflector is generally bulky and large in mass (Huang, 1995a) and may not be ideal for space-borne applications. This system requires a mechanical rotator attached to the reflector to achieve the beam scanning of transmitting/receiving signals, making it very inconvenient.

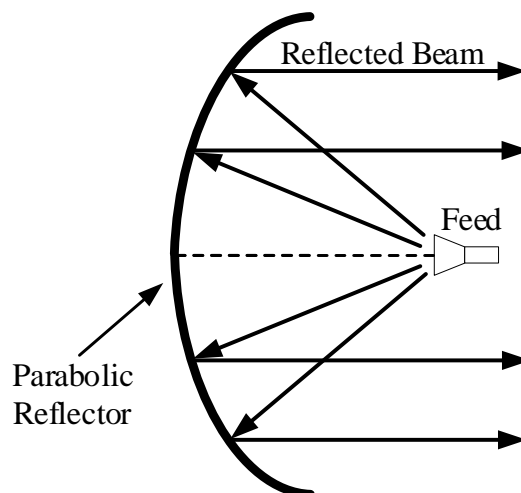


Figure 1.1: Conventional reflector antenna (Balanis, 2005).

Array antennas provide an alternative to reflector antennas. Since the introduction of planar array antenna, which uses microstrip technology to synthesise directive wave beams, it has been possible to obtain lightweight designs. As illustrated in Figure 1.2, it employs electronics to enable beam scanning by providing varied input phases to all the array elements. Although this type of phased array antenna offers the advantage of flexible design freedom, it suffers from high loss due to the use of complex and lossy feeding networks.

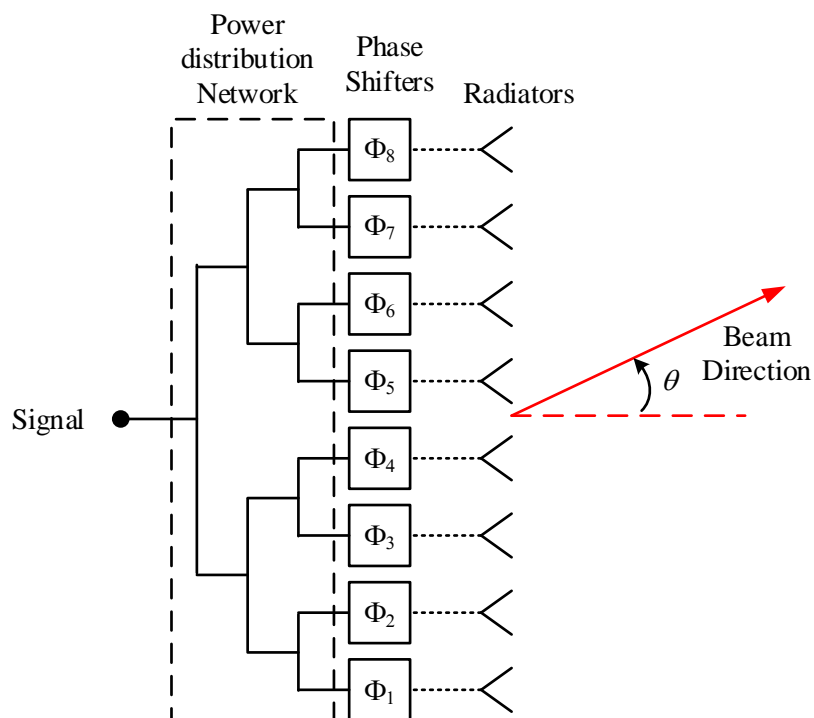


Figure 1.2: Phased array antenna (Mailloux, 2005).

Reflectarray is a new form of antenna that combines the benefits of the reflector antenna and the phased array antenna, while mitigating the drawbacks associated with these high-gain antennas (Nayeri et al., 2018). The reflectarray's

aperture shape is typically square or circular (Bialkowski and Encinar, 2007). Figure 1.3 shows the overall configuration of a reflectarray antenna. It has a flat reflecting surface, which is made up of arrays of scattering elements, with a feeding horn directed onto it at a certain farfield distance. The array of elements is distributed in the form of planar grid topology. The elements are designed in such a way that the incident field from the feed horn is reflected with a specific phase shift to produce a reflected beam in the required broadside direction. Hence, its flat surface, low profile, and lightweight characteristics make it attractive for point-to-point terrestrial and satellite communications. Furthermore, low-cost prototype fabrications are possible with the current advances in the printed-circuit-board (PCB) technology, leading to early commercial implementation.

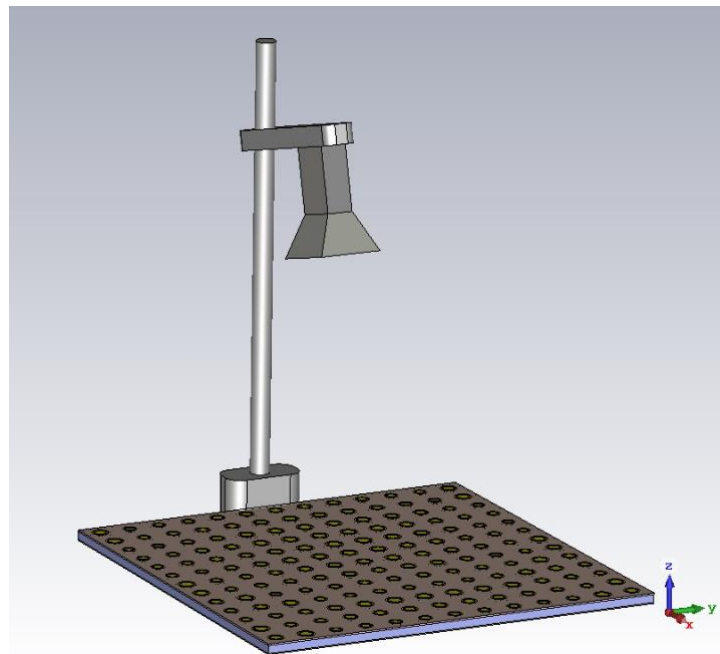


Figure 1.3 Overall geometric of reflectarray antenna.

## 1.2 Development of Reflectarray

Berry was the first to come up with the concept of reflectarray antennas in 1963 (Berry et al., 1963), with the proposed antenna consisting of an array of truncated waveguides. However, such a non-planar structure was very bulky and did not receive much attention until the rapid advancements of printed microstrip antenna technology in the 1980s. The lightweight and low-profile printed reflectarray can be realised, and it has become attractive. The microstrip reflectarray was first introduced by Malagisi (Malagisi, 1978) in 1978 and patented by Munson and Haddad (Munson et al., 1987) in 1987. Later, it was analysed by Huang (Huang, 1991) and demonstrated by Chang (Chang and Huang, 1992). Reflectarray development has grown rapidly since then. Applications such as multi-beam antennas, beam-scanning antennas, and radars have been demonstrated (Nayeri et al., 2018). In the past decade, technological advances in computing power have enabled rigorous phase synthesis and optimisation methods for designing different types of reflectarrays (Chen et al., 2016).

In reflectarray design, the elements are designed to produce a specific reflection phase to compensate for the spatial phase delays of the incident fields from the feed horn. Adjusting the reflection phase of each element produces a progressive phase distribution of the reflected field over the reflectarray aperture so that a planar phase front is generated in the desired direction (Huang and Encinar, 2008), as shown in Figure 1.4.

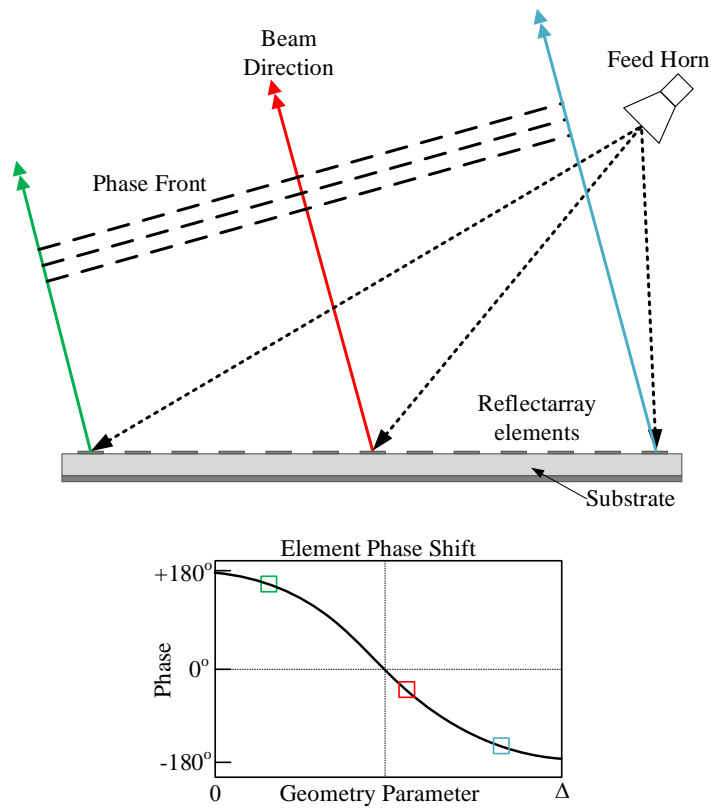


Figure 1.4: Configuration of an offset-fed reflectarray.

Typically, the phase shift is obtained by changing the geometrical parameters of the element, as seen in Figure 1.4. Generally, the phase compensation methods can be categorised into three types. The first method uses variable-size patches (Pozar and Metzler, 1993), loops, or rings (Bialkowski and Sayidmarie, 2008), as depicted in Figures 1.5 (a) and (c), for shifting the phase. Here, the physical dimension of each element is varied to provide a certain reflection phase for compensating the spatial phase delay. It is understood that varying the dimension of the resonant element can generate different scattering impedances, enabling different phase shifts to be realised. The second method, shown in Figure 1.5 (b), utilises phase delay lines (Huang, 1995a), where identical microstrip patches loaded with variable-length phase delay lines are employed for compensating the feed-path delays. In this method,



the microstrip patch element receives an incident field from the feeder and converts it into a guided wave along a terminated open/short-circuited transmission line. The signal is then reflected from the termination line and re-radiated through the patch element. The third method is applicable for circular polarization (CP). This approach uses element rotation (Huang and Pogorzelski, 1998) as a phase shifter, as shown in Figure 1.5 (d). All the elements in the reflectarray are identical but with different angular rotations about their origins. The amount of rotation angle provides a phase shift for the reflected wave to compensate for the spatial delay of the incoming CP wave.

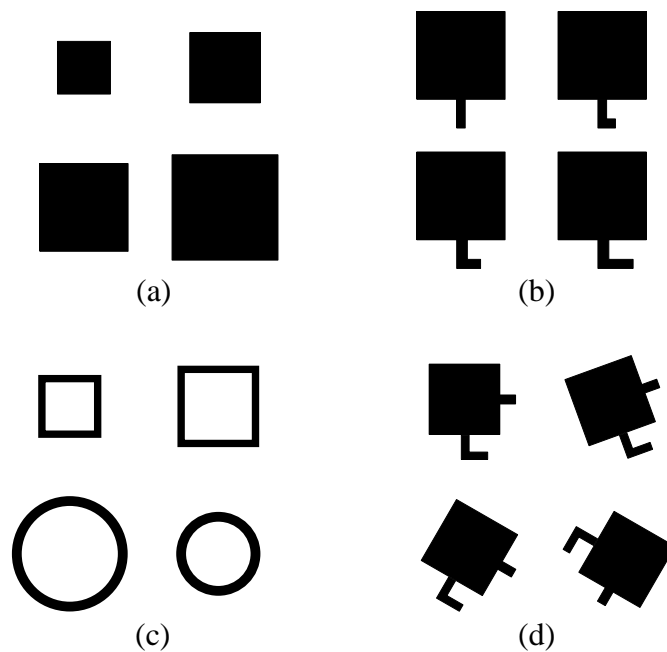


Figure 1.5: Different types of reflectarray elements. (a) variable-size patches, (b) variable-length phase delay lines, (c) variable-size loops or rings, and (d) variable angular rotations.

### 1.3 Broadband Reflectarray Challenges

It is vital to utilise a high-directive antenna to provide sufficient signal strength during transmission and reception in long-distance communication. The printed microstrip reflectarray has a significant advantage over the flat structure, particularly in large spacecraft deployment. This is because it allows a simpler and more reliable folding mechanism than the conventional parabolic reflector. It comes with a distinguished feature by combining a large number of elements, each of which is equipped with elemental phase adjustment capability, to achieve accurate contour beam shaping using the phase synthesis technique. Theoretical models such as phased array theory and aperture field analysis have been used to ease the understanding and evaluation of the reflectarray antenna (Nayeri et al., 2013). Furthermore, full-wave modelling can be applied on a reflectarray antenna by using various commercial electromagnetic simulators. It can accurately simulate the radiation pattern, beam direction, beamwidth, sidelobe, and cross-polarization levels.

Nevertheless, there are still shortcomings associated with the reflectarray antenna that are needed to be addressed. The drawbacks come from its inherent narrow bandwidth characteristic that depends on the element design, aperture size, feed distance, etc. Moreover, the bandwidth performance is still no match for the parabolic reflector (Huang, 1995b; Sze and Shafal, 1998), which is theoretically infinite. The following two factors can primarily limit the bandwidth performance of the printed reflectarray (Huang and Encinar, 2008):

1) The narrow bandwidth of the radiating element, and 2) the spatial phase delays associated with the feed distances to the reflectarray elements.

For the medium and small-size reflectarrays, the bandwidth performance is mainly associated with the radiating element's bandwidth (Poazar, 2003). A conventional microstrip patch element exhibits narrowband behaviour (~3% - 5%), and it can restrict the operating bandwidth of the whole reflectarray (Huang, 1995b). Many methods have been proposed to overcome this limitation by improving the element's phase curve linearity as well as the bandwidth of the radiating element (Bialkowski and Sayidmarie, 2008; Li et al., 2009). Many techniques, such as multilayer designs (Encinar, 2001; Encinar and Zornoza, 2004), multiple resonances structures (Chaharmir et al., 2009; Han et al., 2017), and closely coupled subwavelength radiating elements (Nayeri et al., 2011; Malfajani and Atlasbaf, 2014) have been proposed, with the possibility to improve the bandwidth for more than 20%.

The second limiting factor is the differential spatial phase delay, particularly for a large aperture reflectarray. The spatial phase delay is introduced by the propagation path difference between the feed horn and the respective reflectarray element. The effect of the spatial phase delay is more apparent for a large-sized reflectarray with a smaller focal distance ratio ( $F/D$ ) and centre feed configuration. Since the compensation of the required phase shifts of reflectarray elements are only designed at the centre operating frequency, phase error occurs in the reflected phase-front as the operating frequency changes. Several methods were demonstrated to reduce this

frequency excursion error, such as using time-delay lines to achieve several cycles of  $360^\circ$  phase range to compensate for the actual phase delay (Carrasco et al., 2006). Another method is to use the reflection coefficient phase at a given frequency to compensate for the spatial phase delay error. This approach was demonstrated by Encinar (Encinar and Zornoza, 2003), where three-layer patches are stacked to provide more degrees of freedom for optimisation to achieve the required phase distribution. It means the required phase shift can be optimised at the central frequency and appropriate frequency variation to compensate for the phase delay at other frequencies.

#### **1.4 Problem Statement**

The printed microstrip reflectarray antennas can be easily designed to achieve low profile, low loss, and low production cost, making them suitable for high gain and broad bandwidth operation. For moderate-size reflectarrays, the dominant factor affecting the bandwidth performance is the radiating element's bandwidth, and the effect of differential spatial phase delays is minimal (Pozar, 2003; Carrasco et al., 2008). Conventionally, the reflectarray elements are designed with element size in the order of  $\lambda/2$  and having near resonance operation (Nayeri et al., 2010). Although many research works have demonstrated different ways to improve this narrowband behaviour of the elements, it is still challenging to utilise the conventional reflectarray elements, such as rectangular or circular configurations, to achieve broadband performance. Furthermore, the inherited narrow bandwidth and limited tuning

ability in such elements make them difficult to achieve linear reflection phase response with a broad phase range and, hence, broad bandwidth performance of the reflectarray.

## 1.5 Objectives

In this research, three objectives are set to explore the conventional reflectarray element and explore new ways to improve its narrowband performance. These elements are then used to design moderate-size reflectarrays to achieve broad bandwidth performance.

Objectives:

1. To design a broadband linearly polarized reflectarray using a dumbbell-shaped microstrip ring which is tightly coupled with Vivaldi tapered slot antenna.
2. To design a single-layer broadband linearly polarized reflectarray using a circular patch loaded with unequal slots.
3. To design a broadband linearly polarized reflectarray using closely coupled inter-layer circular ring-patches.

The research work has been carried out through the proposal of three novel reflectarray designs:

- a. The first reflectarray is designed using a Vivaldi tapered slot antenna that is incorporated with a dumbbell-shaped microstrip ring resonator. Here, the size of the ring resonator is functioning as the phase-shifting geometrical

parameter. In this configuration, the incident wave is received from a travelling-wave radiator and coupled to the dumbbell-shaped ring resonator. The proposed reflectarray element is designed to achieve full phase range and low phase sensitivity simultaneously.

- b. The second proposal involves a conventional single-layer circular patch reflectarray element that is loaded with a pair of unequal slots. The aim is to enhance the phase tuning ability and provide a low profile reflectarray design. The phase range and its corresponding phase sensitivity can be optimised by a simple equation that pegs the two unequal slots to the patch radius. Such an approach allows more degrees of freedom for optimising the phase curve. Here, the patch radius serves as a phase-shifting geometrical parameter that can be used to achieve a broad phase range with low phase sensitivity simultaneously.
- c. The third reflectarray design has explored the conventional circular patch reflectarray element for improving the phase tuning ability and enhancing the broadband performance. Here, a double-layer reflectarray element is designed using two closely coupled circular ring-patches for attaining broad bandwidth. The inter-layer coupling has been employed to mitigate the mutual coupling between the reflectarray elements and broaden the operational bandwidth of the phase-shifting elements. Here, the reflection phase curve of the reflectarray element is generated in a unique way from two linear equations that are related to the radii of the top and bottom ring-patches. This design allows more degrees of freedom in the phase tuning.

## 1.6 Publications

Three reflectarrays have been designed and analysed throughout the research, and the results are published/submitted in/to the following peer-reviewed articles.

- a) Phua, Y.N., Lim, E.H. and Chung, B.K., 2018. Vivaldi tapered slot reflectarray loaded with dumbbell-shaped ring resonator. *Microwave and Optical Technology Letters*, 60(2), pp.369–374. (Published)
- b) Phua, Y.N., Lim, E.H. and Chung, B.K., 2020. Design of a single-layer broadband reflectarray using circular microstrip patch loaded with two unequal slots. *AEU - International Journal of Electronics and Communications*, 124, p.153341. (Published)

Other relevant publications:

- a) Phua, Y.N., Lim, E.H. and Chung, B.K., 2018. Broad-range microstrip patch reflectarray element loaded with multiple L-shaped slots. *AEU - International Journal of Electronics and Communications*, 84, pp.123–130.

## 1.7 Thesis Overview

A total of seven chapters are presented in this thesis. It begins with a brief overview of reflectarray technologies, developments, and challenges. At the end of Chapter 1, the research problems are explained, together with the objectives formulated.

Chapter 2 presents a literature study of the reflectarray designs, analysis and synthesis of the reflectarray. The key performance parameters are described.

Chapter 3 presents the design methodology of the element and synthesis of the reflectarray. Prototyping and measurement of the reflectarray are also discussed accordingly.

In Chapters 4, 5, and 6, discussion on the design of the reflectarray is started with a Vivaldi tapered slot radiator that is combined with a dumbbell-shaped square loop, followed by a circular patch loaded with unequal slots and, lastly, a closely coupled inter-payer ring-patches. The detailed reflectarray configurations are illustrated, and the design principles are elaborated. Subsequently, the proposed reflectarrays are fabricated and measured, and their performances are compared to those of the contemporary reflectarrays.

Chapter 7 summarises all the research outcomes and findings in Chapters 4 – 6 as well as future works.



## CHAPTER 2

### LITERATURE REVIEW, REFLECTARRAY THEORY AND DESIGN

#### 2.1 Literature review

Over the years, many single-layer and multi-layer reflectarray elements have been explored for enhancing the reflection phase performances. A full phase range of  $360^\circ$  with a low phase gradient is usually required to provide sufficient phase compensation for minimizing fabrication errors (Pozar et al., 1997). However, it is difficult to obtain both the phase range of  $360^\circ$  and sufficiently low phase sensitivity with the conventional method at the same time. In addition, it is often limited by its tuning ability. Although the single-layer reflectarray is simple and easy to fabricate (Yoon et al., 2014), obtaining a sufficient reflection phase range and good phase linearity is still challenging, even for a conventional single-layer reflectarray.

Much effort has been made to improve the performances of the single-layer patch-type reflectarrays. Since the 90s, patch resonator has been explored for designing various reflectarrays (Pozar et al., 1997). Improved versions, such as different fractal patches (Sayidmarie and Bialkowski, 2011), are explored to lower the phase sensitivity and increase the phase range. Loading a circular patch with two delay lines (Hasani et al., 2010) was found to be able to generate wide bandwidth, with its phase error increasing with incident angle. A circular patch loaded with four semicircular ring slots symmetrically has been reported

by Liu (Liu et al., 2017) to increase the phase range to  $500^\circ$ . However, the sidelobes are pretty high, and the aperture efficiency is low for such an element structure. Another approach that uses two additional phase tuning procedures is introduced to the conventional method (Yoon et al., 2015) to improve the reflection phase range. This approach combines changes of the outer and inner lengths in opposite directions to achieve a sufficient phase range of  $360^\circ$  and low phase sensitivity. Phase sensitivity can also be improved by either employing an air layer or low-permittivity substrates. A thicker substrate or additional foams can improve the phase gradient and achieve smoother reflection phase variation (Bialkowski and Sayidmarie, 2008). However, it can cause the phase range to drop below  $300^\circ$  (Encinar, 2001). On the other hand, the conventional square ring structure is still of interest due to its simple shape and ability to increase the reflection phase, as compared to the square patch (Bialkowski and Sayidmarie, 2008).

Many single-layer multiple-resonances structures, such as circular gapped/split-rings with phase delay lines (Han et al., 2017; Su et al., 2019) and multiple cross/square loops (Chaharmir et al., 2009; Vosoogh et al., 2014), have been proposed to improve the reflectarray performance. These reflectarray structures combine narrow rings-gaps or loops, where the relative lengths of the delay lines or loops are adjusted to produce linear phase responses, for improving bandwidth performance. Although these structures are found to have achieved high aperture efficiency and broad bandwidth, they usually require combining multiple resonators to form a complex-shaped structure, hence, increasing the design complexity.

Another efficient method is to employ closely coupled subwavelength radiating elements such as circular patches with delay lines (Malfajani and Atlasbaf, 2014) and circular coupled rings (Mohammadi et al., 2018), and circular rings with sectorial slits (Yu and Guo, 2019). The main advantage of these designs is that they allow almost equal mutual coupling between the adjacent elements as well as lower reflection loss. Such structures are suitable for small and compact reflectarrays (Nayeri et al., 2011). The downside of this design is that the reflection phase curve is usually highly nonlinear and steep near the resonance, but showing slow variation when moving away from it. Furthermore, they require a high-precision fabrication process, which can increase the fabrication costs.

The multi-layer structure is well-known for effectively improving the phase range for more than  $360^\circ$ , offering a smooth phase slope, which enhances the operational bandwidth of the entire reflectarray antenna (Bialkowski and Sayidmarie, 2008). Double-layer rectangular patches which are placed in conventional topology by stacking the phase-shifting elements are shown to have multiresonance behaviour (Encinar, 2001; Tienda et al., 2013), where a progressive phase shift of more than  $360^\circ$  is achievable by varying the element size in both layers. Superior performance in terms of phase linearity, phase range, and bandwidth has been observed. The bandwidth can be further improved by incorporating the subwavelength technique (Nayeri et al., 2010). A different multilayer structure was demonstrated by combining a conventional square patch and a slot (Chaharmir et al., 2003). However, it would require the use of an additional substrate to smoothen the phase slope, with a limited phase

range of less than  $360^\circ$ . An improved method was also introduced by coupling a ring with a ring-shaped slot on the ground (Oh et al., 2009). This design could overcome the limited phase range of the conventional ring element, and it could achieve a smooth phase of over  $680^\circ$  with good gain performance. However, stacking resonators requires precise alignment. Incorporating more substrates into the reflectarray design can also result in additional mass, material costs, and reflection losses.

## 2.2 Design of Reflectarray

Designing a reflectarray antenna involves several steps: (1) Designing the phasing element, (2) aperture selection, (3) phase distribution mapping, and (4) feeding consideration. In addition, most of the reflectarray elements need to be optimised to meet the performance requirement, particularly the reflection phase. The optimum reflection phase can then be used to synthesise the phase distribution of the reflectarray aperture to produce a collimated beam. Then, the antenna performance of interest, such as radiation pattern, gain, and bandwidth, is analysed.

Typically, the design starts with a specific gain requirement, where the gain is obtained by multiplying the aperture efficiency with the maximum directivity (Balanis, 2005). As a result, the aperture efficiency analysis can be applied to determine the aperture size of the reflectarray. The geometrical parameters of the reflectarray, such as the location of the feed, incident angle, and  $F/D$  ratio, can be optimised accordingly. In addition, factors influencing the reflectarray design, such as feed blockage and edge taper, can be minimised. Nevertheless, some compromises can be made in the reflectarray design to realise optimum performance. The following sections outline the basic working principle of the reflectarray. Important design parameters will be discussed here (Yu et al., 2010).

### 2.3 Feed Model

Figure 2.1 illustrates a reflectarray with a square aperture in the  $xy$ -plane, which is positioned at the centre of  $(x, y, z)$ . A feed antenna is located at  $(x', y', z')$ , being positioned at farfield distance and directed towards the centre of the aperture. The location and radiation characteristics of the feed are important in the aperture illumination analysis, which in turn governs the reflectarray gain performance.

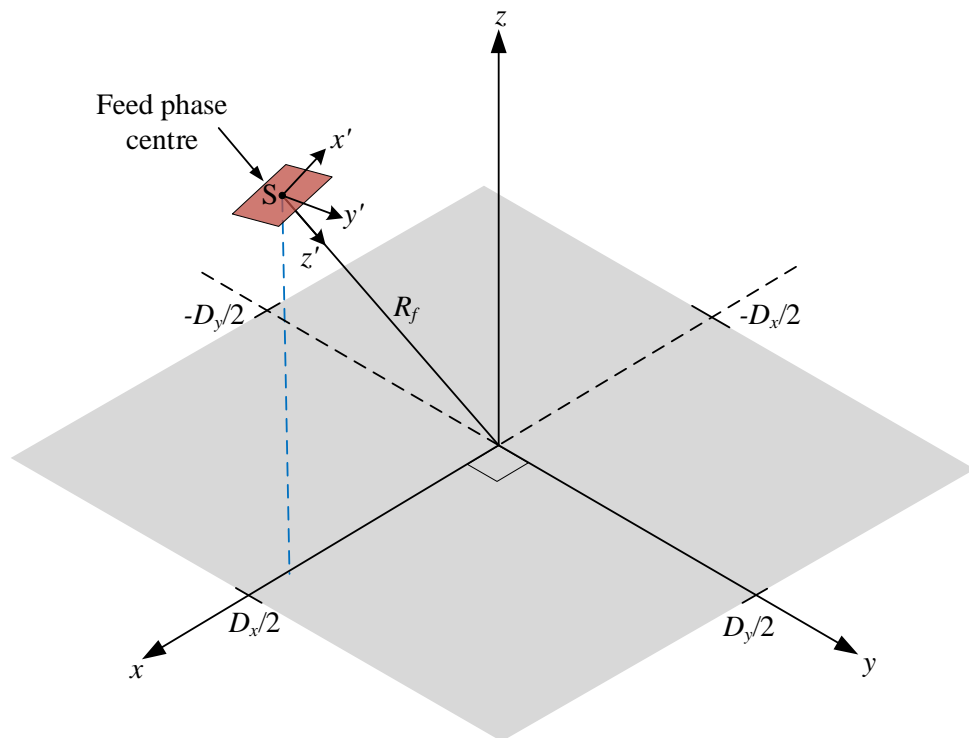


Figure 2.1: Coordinates representation of the reflectarray aperture and feeding antenna.

The feed radiation pattern can be modelled using the cosine- $q$  function due to its simplicity in describing the pattern types (Stutzman and Thiele, 1998; Lo and Lee, 1993). For an ideal linearly polarized feed antenna, the radiation

field can be represented by the two components along their respective principle planes (assuming the rotationally symmetrically pattern and constant phase centre), and is expressed as (Nayeri et al., 2018):

$$E_x(R_f, \theta_f, \varphi_f) = \frac{A_0 e^{-jkR_f} \cos^{q_f} \theta_f}{R_f} [\hat{\theta} \cos \varphi_f - \hat{\varphi} \sin \varphi_f], \text{ for } x\text{-polarized} \quad (2.1)$$

$$E_y(R_f, \theta_f, \varphi_f) = \frac{A_0 e^{-jkR_f} \cos^{q_f} \theta_f}{R_f} [\hat{\theta} \sin \varphi_f + \hat{\varphi} \cos \varphi_f], \text{ for } y\text{-polarized} \quad (2.2)$$

where  $R_f$  is the distance vector from the phase centre of the feed S to a point on the reflectarray aperture.  $\theta_f$  and  $\varphi_f$  are the angles at the feeding coordinate point  $(x', y', z')$ . From Figure 2.1, the maximum radiation of the feed is directed toward the centre of the aperture. At the feed region, the radiation pattern is assumed to have a normalised power pattern, and it can be expressed as:

$$U_f(\theta_f, \varphi_f) = \begin{cases} \cos^{2q_f} \theta_f & \text{for } 0 \leq \theta_f \leq \pi/2 \\ 0 & \text{elsewhere} \end{cases} \quad (2.3)$$

The power factor parameter  $q_f$  can then be used to describe the directivity and pattern shape of the feed. Figure 2.2 illustrates a radiation pattern of the feed model as a function of the  $q$ -factor. As the  $q$ -factor increases, the beamwidth of the radiation pattern decreases.

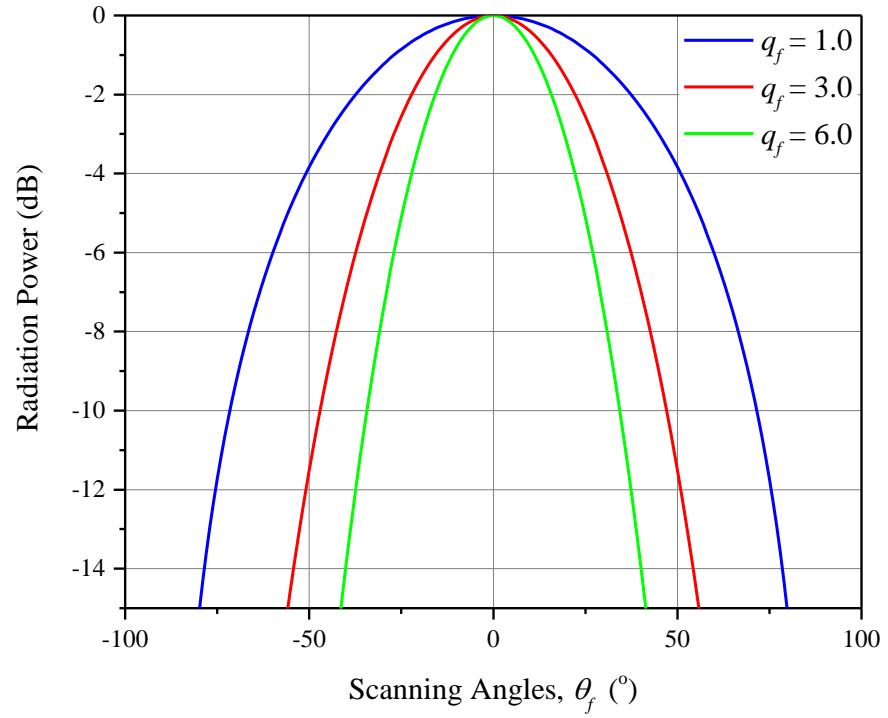


Figure 2.2: The feed radiation pattern for different  $q$ -factors.

## 2.4 Aperture Efficiency

The directivity of an antenna is defined as the ratio of radiation intensity in a given direction from the antenna to its overall radiation intensity (Stutzman and Thiele, 1998). Hence, the maximum directivity of a reflectarray antenna is expressed as:

$$\Omega_{\max} = \frac{4\pi A_{\text{aper}}}{\lambda^2} \quad (2.4)$$

where  $A_{\text{aper}}$  is the physical aperture area of the antenna and  $\lambda$  is the wavelength of the electromagnetic wave obtained from the design frequency.



The gain of a reflectarray antenna can be calculated by multiplying the directivity with the aperture efficiency (Stutzman and Thiele, 1998), and is expressed as:

$$G = \frac{4\pi A_{\text{aper}}}{\lambda^2} \eta_{\text{aper}} \quad (2.5)$$

where  $\eta_{\text{aper}}$  is the aperture efficiency of the antenna. Using this relationship, one can estimate the aperture size at a particular design frequency with the target gain and aperture efficiency. Figure 2.3 shows an example of this relationship for a square aperture (side lengths,  $D_x = D_y = D$ ) with different electrical sizes as a function of the reflectarray  $D/\lambda$ , at a design frequency of 9.0 GHz. Hence, the aperture size primarily affects the antenna gain (Huang and Encinar, 2008), and more elements in a reflectarray can lead to a higher antenna gain.

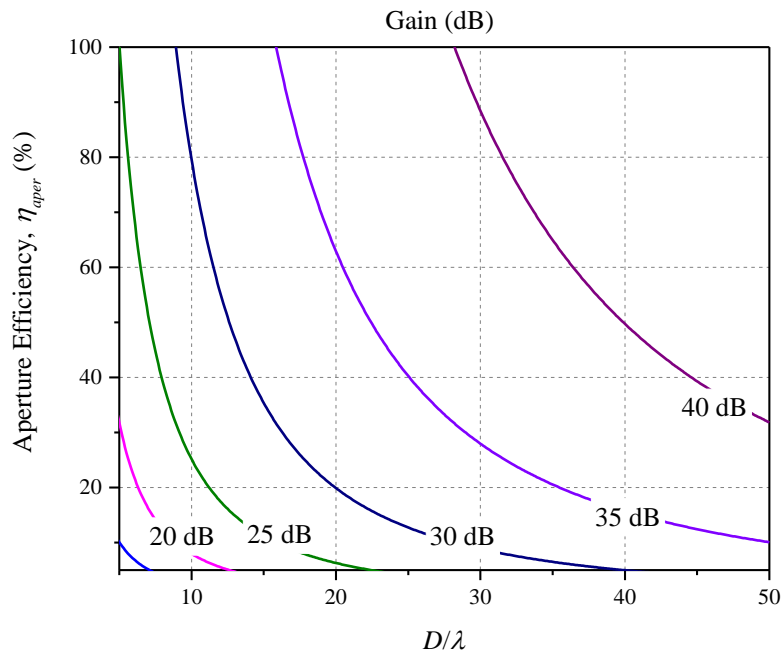


Figure 2.3: Gain as a function of the aperture efficiency and electrical size of the reflectarray.

The aperture efficiency of a reflectarray antenna is a product of spillover efficiency, illumination efficiency, and other efficiency factors such as phase efficiency, material loss, polarization efficiency, blockage efficiency, and feed efficiency (Nayeri et al., 2018; Yu et al., 2010). Evaluating the relationship between the configuration parameters and efficiencies can result in optimum gain performance at the reflectarray system level. The spillover efficiency ( $\eta_s$ ) and illumination efficiency ( $\eta_i$ ) are the two major efficiency factors that are intrinsically linked to the antenna parameters (Nayeri et al., 2018). Hence, the aperture efficiency can be expressed as:

$$\eta_{\text{aper}} = \eta_s \eta_i \quad (2.6)$$

#### 2.4.1 Efficiency Model: Geometrical Parameters Definition

Before beginning the efficiency factors' analysis, the reflectarray's configuration parameters and coordinates system are established. Figure 2.4 illustrates the configuration parameters and coordinate system, with the important quantities involved listed in Table 2.1. An offset feed pointing towards the centre of a square aperture at an incident angle  $\theta_i$  is considered. The feed lies on the  $xz$ -plane, having a phase centre located at S, with a height of  $h$  from the aperture plane.

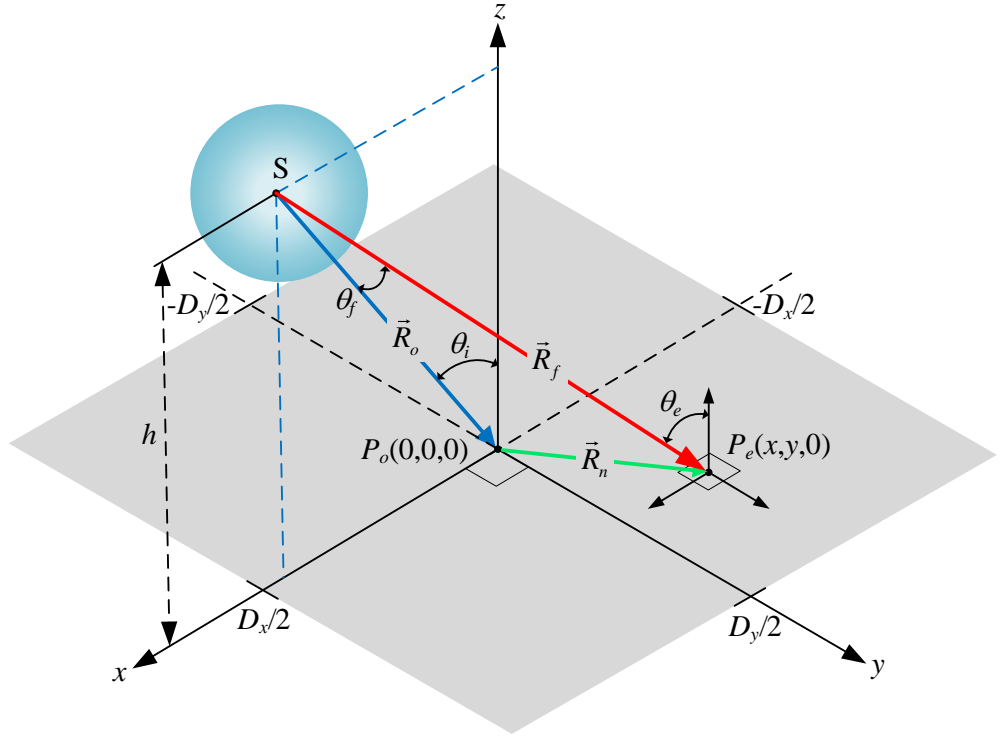


Figure 2.4: Configuration parameters and Cartesian coordinate of a reflectarray antenna.

Table 2.1: Configuration Parameters.

Quantity	Geometrical Relation
Feed location, S	$S(h \tan \theta_i, 0, h)$
Feed beam point, $P_o$	$P_o(x_o, y_o, z_o) = P_o(0, 0, 0)$
Element location, $P_e$	$P_e(x, y, 0)$
Position Vector of the $n^{\text{th}}$ element	$\vec{R}_n = \hat{x}x + \hat{y}y$
Position vector from the feed point S to the centre of the aperture $P_o$ , $\vec{R}_o$	$\vec{R}_o = -\hat{x}h \tan \theta_i - \hat{z}h$
Magnitude, $ \vec{R}_o $	$ \vec{R}_o  = \sqrt{(h \tan \theta_i)^2 + h^2} = h \sec \theta_i$
Position vector from the feed point S to the $n^{\text{th}}$ element $P_e$ , $\vec{R}_f$	$\vec{R}_f = \hat{x}(x + h \tan \theta_i) + \hat{y}y - \hat{z}h$
Magnitude, $ \vec{R}_f $	$ \vec{R}_f  = \sqrt{x^2 + y^2 + 2xh \tan \theta_i + h^2 \sec^2 \theta_i}$

Unit vector, $\hat{R}_f$	$\hat{R} = \frac{\hat{x}(x+h \tan \theta_i) + \hat{y}y - \hat{z}h}{\sqrt{x^2 + y^2 + 2xh \tan \theta_i + h^2 \sec^2 \theta_i}}$
Distance between $P_o$ and $P_e$ ,	$ \vec{R}_n  = \sqrt{(x-x_o)^2 + (y-y_o)^2}$
Feed pattern parameter $\theta_f$ : elevation angle in the feed coordinate frame	$\cos \theta_f = \frac{R_o^2 + R_f^2 - R_n^2}{2R_o R_f}$
Element pattern parameter $\theta_e$ : elevation angle in the local coordinate frame of the $n^{\text{th}}$ element	$\cos \theta_e = \frac{h}{R_f}$

#### 2.4.2 Spillover Efficiency

The spillover efficiency ( $\eta_s$ ) can be described by the following equation (Nayeri et al., 2018):

$$\eta_s = \frac{\iint_A \vec{P}(\vec{R}_f) \cdot d\vec{A}}{\iint_S \vec{P}(\vec{R}_f) \cdot d\vec{A}} \quad (2.7)$$

where  $\vec{P}$  is the Poynting vector of the feed.  $\eta_s$  is the fractional of the overlapped radiated power, which is generated from the feed with the reflectarray aperture to the power radiated by the feed. The radiation power can be defined using Equation (2.3) can be expressed as:

$$\vec{P}(\vec{R}_f) = \hat{R}_f \frac{\cos^{2q_f} \theta_f}{R_f^2} \quad \text{for } 0 \leq \theta_f \leq \pi/2 \quad (2.8)$$

The denominator integral in Equation (2.7) can be evaluated analytically using spherical coordinates over the entire surface area of a sphere  $S$ , and it has a closed-form expression as:

$$\iint_S \vec{P}(\vec{R}_f) \cdot d\vec{A} = \int_0^{2\pi} \int_0^{\pi/2} \cos^{2q_f} \theta_f \sin \theta_f d\theta_f d\varphi_f = \frac{2\pi}{2q_f + 1} \quad (2.9)$$

For the numerator, the integral is performed over the reflectarray's aperture area  $A_{aper}$ . By substituting the quantities defined in Table 2.1 and Equation (2.8), the numerator expression is expressed as:

$$\iint_{A_{aper}} \vec{P}(\vec{R}_f) \cdot d\vec{A} = \int_{-D_x/2}^{D_x/2} \int_{-D_y/2}^{D_y/2} \left[ \frac{h}{R_f^3} \left( \frac{R_o^2 + R_f^2 - R_n^2}{2R_o R_f} \right)^{2q_f} \right] dx dy \quad (2.10)$$

In summary, the numerator is dependent on the feed location and aperture geometry. Hence, by substituting Equations (2.9) and (2.10) into (2.7), the spillover efficiency can be expressed as:

$$\eta_s = \left( \frac{2q_f + 1}{2\pi} \right) \int_{-D_x/2}^{D_x/2} \int_{-D_y/2}^{D_y/2} \left[ \frac{h}{R_f^3} \left( \frac{R_o^2 + R_f^2 - R_n^2}{2R_o R_f} \right)^{2q_f} \right] dx dy \quad (2.11)$$

### 2.4.3 Illumination Efficiency

Illumination or taper efficiency ( $\eta_i$ ) is defined as the field amplitude distribution of the feed pattern over the reflectarray aperture, and it is expressed as (Nayeri et al., 2018):

$$\eta_i = \frac{1}{A_{aper}} \frac{\left| \iint_{A_{aper}} I(x, y) dA \right|^2}{\iint_{A_{aper}} |I(x, y)|^2 dA} \quad (2.12)$$

where  $I(x, y)$  is the amplitude distribution over the aperture. The aperture amplitude distribution for reflectarray is a function of the feed radiation pattern over the aperture and the element radiation pattern, which gives smaller energy radiated from the aperture than the energy illuminated on the aperture.

For the reflectarray element, its radiation pattern is modelled using the cosine- $q$  function (Yu et al., 2010), and the normalised power pattern is expressed as:

$$U_e(\theta_e, \varphi_e) = \begin{cases} \cos^{2q_e} \theta_e & \text{for } 0 \leq \theta_e \leq \pi/2 \\ 0 & \text{elsewhere} \end{cases} \quad (2.13)$$

Here,  $q_e$  is the power factor of the element, and  $\theta_e$  is the elevation angle of the element at the local coordinate on the reflectarray aperture. Generally, the values of  $q_e$  are much lower as compared to the case of the feed power factor. Hence, the element pattern has a broader beamwidth (Nayeri et al., 2018) with a nominal value of approximately equal to 1. By combining Equations (2.3) and (2.13), the normalised amplitude distribution is given as:

$$I_{norm}(x, y) = \frac{\cos^{q_f} \theta_f \cos^{q_e} \theta_e}{R_f} \quad (2.14)$$

where  $R_f$  is the path length taken by the feed radiation to reach a certain point on the aperture. By substituting the quantities defined in Table 2.1 and Equation (2.14), the illumination efficiency is expressed as:

$$\eta_i = \frac{1}{D^2} \frac{\left[ \int_{-D_x/2}^{D_x/2} \int_{-D_y/2}^{D_y/2} \left[ \frac{(R_o^2 + R_f^2 - R_n^2)^{q_f}}{2R_o^{q_f} R_f^{q_f+q_e+1}} \right] dx dy \right]^2}{\int_{-D_x/2}^{D_x/2} \int_{-D_y/2}^{D_y/2} \frac{(R_o^2 + R_f^2 - R_n^2)^{2q_f}}{2R_o^{2q_f} R_f^{2(q_f+q_e+1)}} dx dy} \quad (2.15)$$

#### 2.4.4 Effects of Configuration Parameters on the Efficiencies Factors

In the practical design of a reflectarray, the feed location is an important parameter. From Figure 2.1, the feed position is defined by the offset angle  $\theta_i$  (wave incident angle) and the focal distance  $F(\theta_i, H) = |\vec{R}_o|$  (Table 2.1). Figures 2.5 and 2.6 show the efficiency factors ( $\eta_s, \eta_i$ ) and the total aperture efficiency ( $\eta_{aper}$ ) for different offset angles and focal distances to the aperture dimension ratios,  $F/D$ , respectively. The shape of the reflectarray aperture is square, with a width of 325 mm. The power patterns of the feed and element are fixed at  $2q_f = 6$  and  $q_e = 1$ , respectively.

In Figure 2.5, the offset angle ( $\theta_i$ ), varies while the  $F/D$  ratio is fixed at 0.65. When  $\theta_i$  increases, the spillover efficiency decreases, and the illumination efficiency has little effect. The maximum aperture efficiency is optimum for the centre feed. An offset feed over the centre feed is typically

preferred to minimise feed blockage (Wu et al., 2018). The detrimental effect of feed blockage will give rise to the side-lobe levels, causing a decrease in antenna gain (Budhu and Rahmat-Samii, 2011). In addition, a large offset angle results in a large oblique angle excitation, particularly the edge elements, which further degrades the performance of the reflectarray. As a result, keeping the offset angle to minimum while compromising the feed blockage is important.

Figure 2.6 shows that the efficiency varies with the  $F/D$  ratio, with the offset angle set at  $20^\circ$ . As the feed focus distance increases, the reflectarray aperture angle subtends from the feed reduces, causing the spillover efficiency to decrease. At the same time, a more uniform field is distributed on the aperture plane, leading to an increase in the illumination efficiency (Yu et al., 2010). In this example, the maximum aperture efficiency is located at 0.65.

Figure 2.7 shows the 2D plot of the aperture efficiency varying with  $q$ -factor and  $F/D$  ratio at an offset angle of  $20^\circ$ . It can be seen that the feed distance is linked to the  $q$ -factor. Generally, good aperture efficiency can be obtained with a large  $q$ -factor as well as a high feed position. However, a highly directive feed pattern of a large value of  $q$ -factor is usually undesirable. This is because the associated feed antenna has a large physical dimension which causes substantial aperture blockage (Nayeri et al., 2018) and leads to a large reflectarray antenna profile (Dahri et al., 2020). For a compact reflectarray antenna profile, a broad feed pattern of lower  $q$ -factor is suitable to be used. Hence, designing a reflectarray system should also consider a manageable reflectarray antenna profile.



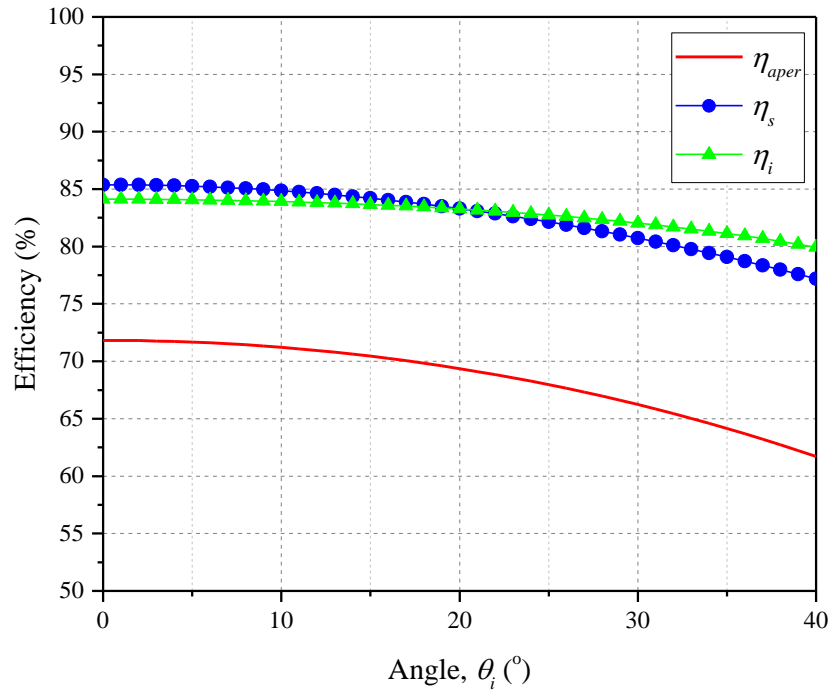


Figure 2.5: Effects of offset angle  $\theta_i$  on the efficiencies at  $F/D = 0.65$ .

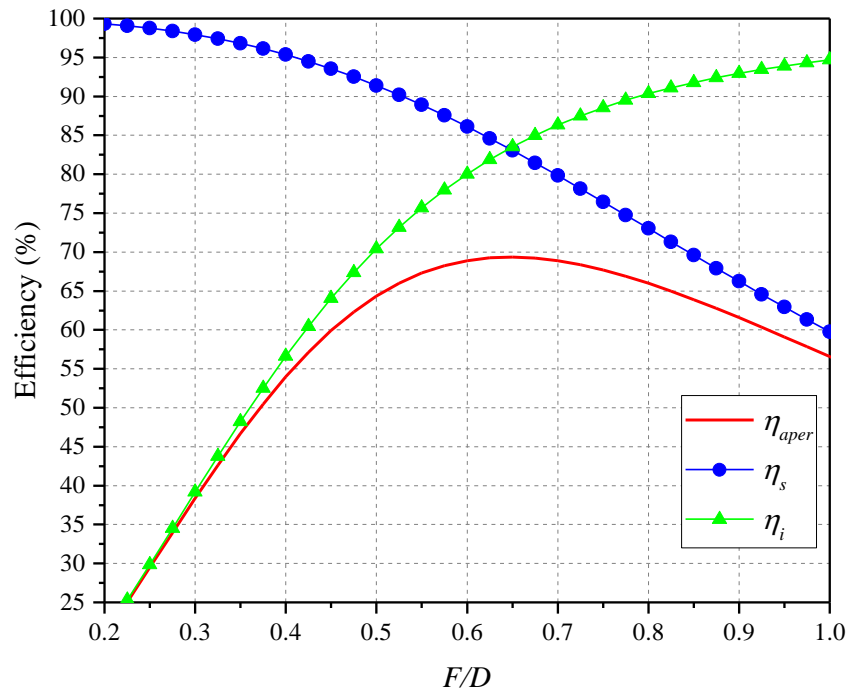


Figure 2.6: Effects of  $F/D$  ratio on the efficiencies at an offset angle  $\theta_i = 20^{\circ}$ .

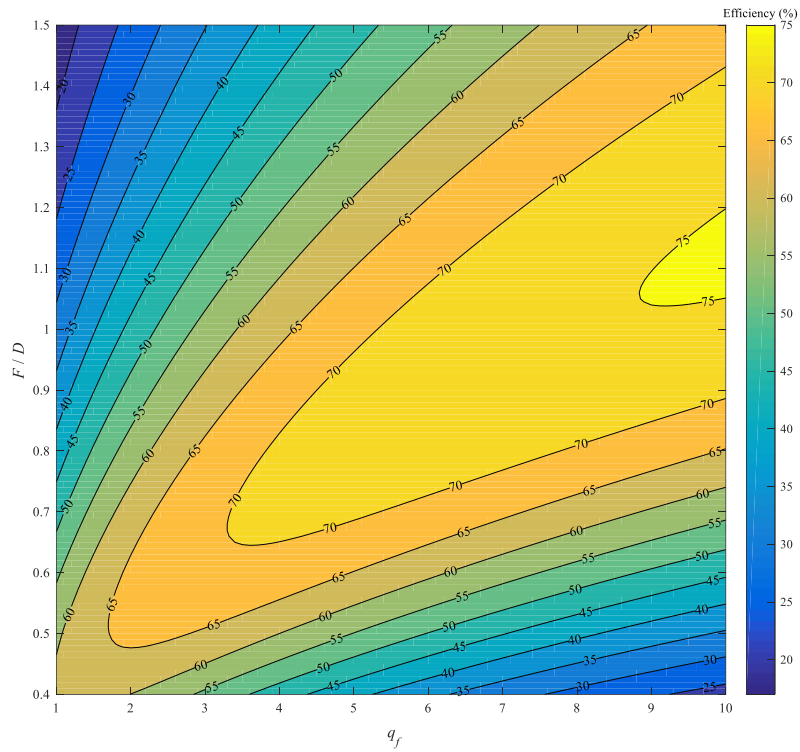


Figure 2.7: 2D plot of aperture efficiency varying with  $q$ -factor and  $F/D$  ratio at an offset angle of  $20^\circ$ .

It is important to note that the feed pointing position is typically chosen to be at the centre of the reflectarray aperture. Although the optimum feed pointing position is slightly offset from the centre, it does not affect the overall efficiency (Nayeri et al., 2018) significantly. Like reflector antennas, the shape of the aperture also plays a vital role in maximising the aperture efficiency of the reflectarray antenna. The typical reflectarray aperture shape being used is either circular or rectangular. Although the aperture efficiency of the circular aperture surpasses the rectangular one in the case of normal feed, the efficiency degrades with the offset feed (Nayeri et al., 2018).

## 2.5 Radiation Pattern: Array-Theory Method

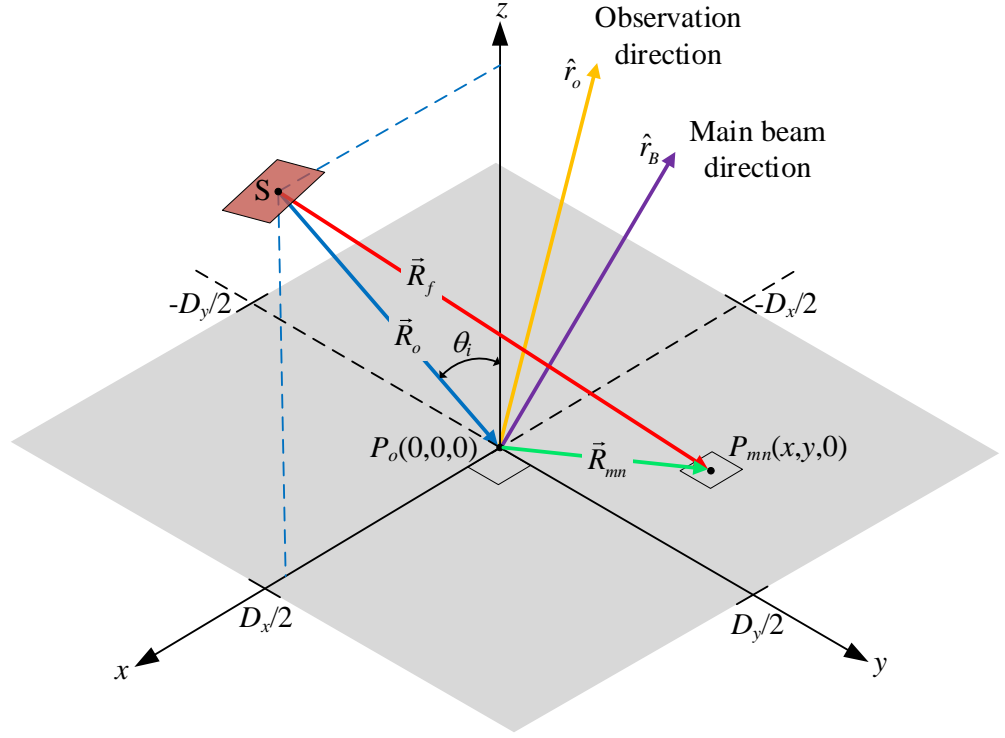


Figure 2.8: Coordinate representation of a reflectarray antenna.

The farfield radiation pattern of a reflectarray antenna can be computed using the conventional phased array theory (Balanis, 2005). Figure 2.8 shows the coordinate representation of the reflectarray antenna radiation analysis. The radiation field distribution of a 2D array with  $M \times N$  elements is given as:

$$\vec{E}(\hat{r}_o) = \sum_{m=1}^M \sum_{n=1}^N \vec{A}_{mn}(\hat{r}_o) \cdot \vec{I}_{mn}(\vec{R}_{mn}) \quad (2.16)$$

$$\hat{r}_o = \hat{x} \sin \theta \cos \varphi + \hat{y} \sin \theta \sin \varphi + \hat{z} \cos \theta$$

where  $\vec{A}_{mn}$  is the element pattern vector function,  $\vec{I}_{mn}$  is the element excitation vector function, and  $\vec{R}_{mn}$  is the position vector of the  $mn^{\text{th}}$  element (Huang and Pogorzelski, 1998; Nayeri et al., 2013).

The radiation field of an element can use the cosine- $q$  function as described in Section 2.4.3, and it can be expressed as:

$$E_e(\theta_e, \varphi_e) = \begin{cases} \cos^{q_e} \theta_e & \text{for } 0 \leq \theta_e \leq \pi / 2 \\ 0 & \text{elsewhere} \end{cases} \quad (2.17)$$

where  $\theta_e$  is the elevation angle in the local coordinate frame of the  $n^{\text{th}}$  element on the reflectarray aperture, as shown in Figure 2.4.

For simplicity, a scalar approximation for each element pattern is expressed as:

$$A_{mn}(\theta, \varphi) \approx \cos^{q_e} \theta \cdot e^{jk(\vec{R}_{mn} \cdot \hat{r}_o)} \quad (2.18)$$

The element excitation function  $I_{mn}$  can be obtained from the incident field and the element's properties. The incident field from the feed can be approximated using the cosine- $q$  model as described in Section 2.3, and it can be expressed as:

$$E_f(\theta_f, \varphi_f) = \begin{cases} \cos^{q_f} \theta_f & \text{for } 0 \leq \theta_f \leq \pi / 2 \\ 0 & \text{elsewhere} \end{cases} \quad (2.19)$$

where  $\theta_f$  and  $\varphi_f$  are the elevation angles at the feed coordinate system.

In addition, each element that is being excited takes account of receiving mode pattern  $|\Gamma_{mn}|$ . This pattern model is also modelled using the cosine- $q$  function and expressed as:

$$|\Gamma_{mn}| = \cos^{q_e} \theta_e(m, n) \quad (2.20)$$

The excitation of the element can be written as:

$$I(m, n) \approx \frac{\cos^{q_f} \theta_f(m, n)}{|\vec{R}_{mn} - \vec{R}_o|} e^{-jk(|\vec{R}_{mn} - \vec{R}_o|)} |\Gamma_{mn}| e^{j\phi_{p, mn}} \quad (2.21)$$

$|\vec{R}_{mn} - \vec{R}_o|$  is the spatial delay caused by the Euclidian distance between the feed and the  $mn^{\text{th}}$  element.  $\phi_{p, mn}$  is the required phase delay of the  $mn^{\text{th}}$  element, and it is used to set the main beam in the  $\hat{r}_B$  direction. The analysis of the reflectarray element using the infinite-array approach to obtain the phase delay will be discussed in Section 2.8.

Hence, the scalar form of the radiation field pattern can be written as:

$$\begin{aligned} E(\theta, \varphi) &= \sum_{m=1}^M \sum_{n=1}^N \text{Cos}^{q_e} \theta \frac{\text{Cos}^{q_f} \theta_f(m, n) \text{Cos}^{q_e} \theta_e(m, n)}{|\vec{R}_f|} e^{-jk(|\vec{R}_f| - \vec{R}_{mn} \cdot \hat{r}_o)} e^{j\phi_{p, mn}} \\ &= (\text{Cos}^{q_e} \theta) \sum_{m=1}^M \sum_{n=1}^N \frac{\text{Cos}^{q_f} \theta_f(m, n) \text{Cos}^{q_e} \theta_e(m, n)}{|\vec{R}_f|} \\ &\quad \times e^{-jk(|\vec{R}_f| + \phi_{p, mn})} e^{jk(x \sin \theta \cos \varphi + y \sin \theta \sin \varphi)} \end{aligned} \quad (2.22)$$

Figure 2.9 shows an example of the normalised radiation pattern of a 13×13 reflectarray. Although this formulation is simple, it does not take into consideration the polarization of the reflectarray antenna.

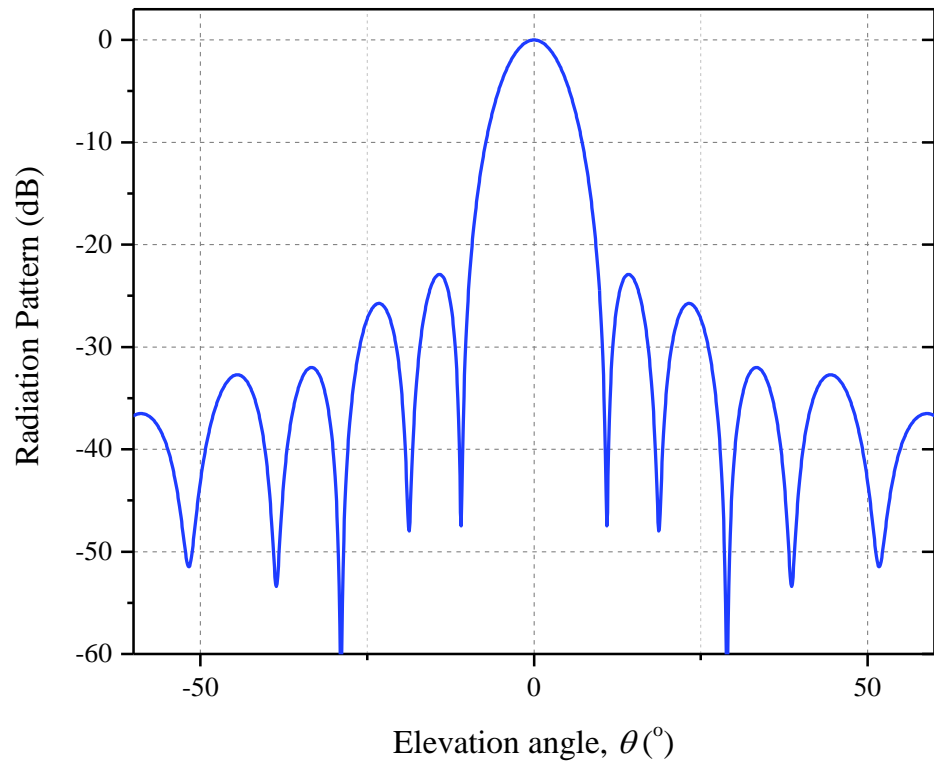


Figure 2.9: Normalised radiation pattern of a 13×13 reflectarray.

## 2.6 Phase Shift Distribution

The distribution of phase shift over the reflectarray aperture requires proper synthesis of the element's reflection phase response so that it can realise a reflected beam in the desired direction. Hence, it is paramount to design and analyse the reflectarray element to obtain an optimised reflection phase response.

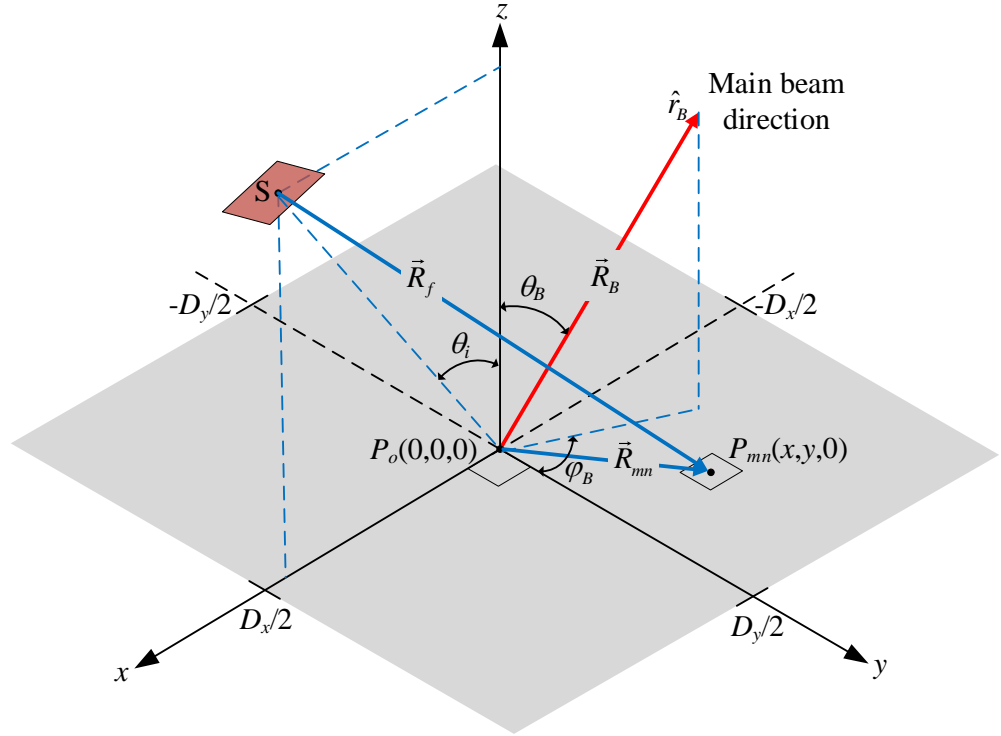


Figure 2.10: Geometrical representation of a reflectarray antenna.

Figure 2.10 illustrates the geometrical layout of a reflectarray. The feed is located at a farfield distance from the reflectarray planar aperture, and it points towards the centre of the aperture at a certain angle  $\theta_i$ . The incident plane wave on each element has a phase directly proportional to the distance travelled from the feed. The distance from the phase centre of the feed to the element is referred to as spatial phase delay. To achieve a collimated beam, this spatial delay needs to be compensated by a specific reflection phase shift generated from each element and is expressed as:

$$\phi_{s,mn} = -k_o R_{mn} \quad (2.23)$$

where  $k_o$  is the wavenumber in free space at the design frequency,  $R_{mn}$  is the distance from S to the  $mn^{\text{th}}$  element. In order to produce a reflected wave in a particular direction  $(\theta_B, \varphi_B)$ , a progressive phase needs to be introduced by each element (Huang and Encinar, 2008), and it is expressed as:

$$\begin{aligned}\phi_{p,mn} &= -k_o \vec{R}_{mn} \cdot \hat{r}_B \\ \hat{r}_B &= \hat{x} \sin \theta_B \cos \varphi_B + \hat{y} \sin \theta_B \sin \varphi_B + \hat{z} \cos \theta_B\end{aligned}\quad (2.24)$$

where  $\vec{R}_{mn}$  is the position vector of the  $mn^{\text{th}}$  element, and  $\hat{r}_B$  is the unit vector of the reflected main beam.

Hence, the required phase shift of the reflectarray element must satisfy the following equation:

$$\begin{aligned}k_o (R_{mn} - \vec{R}_{mn} \cdot \hat{r}_B) - \phi_{mn} &= 2N\pi \\ \phi_{mn} &= k_o (R_{mn} - \vec{R}_{mn} \cdot \hat{r}_B) - 2N\pi\end{aligned}\quad (2.25)$$

where  $\phi_{mn}$  is the phase of the reflection coefficient or phase shift for the  $mn^{\text{th}}$  element and  $N$  is an integer. In the reflectarray design, the reflection coefficient phase must be adjusted in each element to match with the required phase given by Equation (2.25). The ability of an independent phase adjustment for each reflectarray element can be used to shape the beam.



For broadside collimation  $\hat{r}_B \equiv \hat{z}$ , Equation (2.25) becomes

$$k_o R_{mn} - \phi_{mn} = 2N\pi$$

$$\phi_{mn} = k_o R_{mn} - \phi_o - 2N\pi \quad (2.26)$$

Under this condition, only the spatial phase delay is considered in the phase compensation process. A constant phase  $\phi_o$  is added here, indicating that it is a relative reflection phase rather than an absolute reflection phase required in the reflectarray design (Nayeri et al., 2011). Figure 2.11 shows an example of the ideal required phase distribution of a reflectarray of  $15 \times 15$  elements that produces a pencil beam in the broadside direction. The feed is focused at the centre of the aperture with (a) normal and (b) oblique incidents.

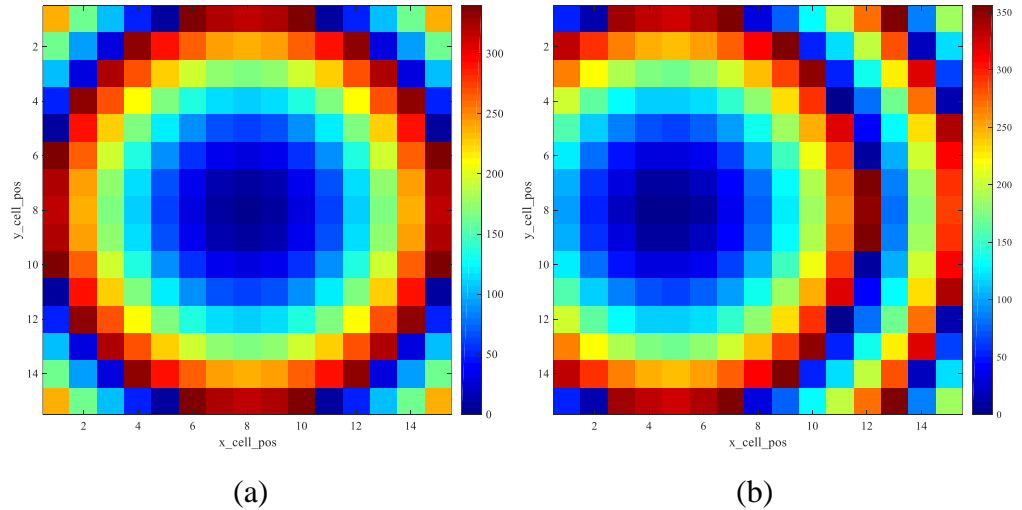


Figure 2.11: Example of the required phase distribution in a square reflectarray. (a) Normal feed and (b) Offset feed.

## **2.7 Element Phase Tuning Methodology**

The phase shift that needs to be introduced by the reflectarray element can be achieved by varying one of the geometrical parameters of the radiating element, as discussed in Section 1.2. Generally, it can be grouped into three methods: 1) delay lines, 2) variable sizes, and 3) variable rotation angles. It is crucial to select a phase-tuning approach to allow the elements to attain the required phase response characteristics. The analysis of the phase characteristics is carried out using the unit cell analysis and is described in the following section.

## **2.8 Element Modelling Techniques**

A reflectarray antenna typically involves a large number of periodically spaced elements arranged in a grid manner. Therefore, mutual coupling between the adjacent elements should be considered in designing the reflectarray elements. However, the simulation/modelling of a full-fledged reflectarray requires an intensive computational process. Typically, the infinite-array approach is used to characterise and analyse reflectarray (Rajagopalan et al., 2012). This method evaluates the reflectarray element using Floquet's theorem (modes), and the overall analysis can be reduced to the unit cell environment (Bhattacharyya, 2005). This infinite-array model provides the periodic boundary condition so that the element can be virtually extended into an infinite array, and it accounts for the mutual coupling between elements. This technique provides an efficient way to characterise reflectarray elements

accurately. Figure 2.12 shows the unit cell model formed by placing the unit element inside a 3D rectangular boundary. The unit element is a square patch with the patch width ( $\Lambda$ ) as the geometrical parameter change. A plane wave ( $y$ -polarized) emerges from the source plane known as Floquet port, which is usually located at a distance of  $\lambda/2$  at the minimum frequency (Nayeri et al., 2018). A set of Floquet modes are excited by the port, and they impinge on the unit element, either normal or obliquely. The port can be de-embedded close to the unit element surface, where the reflected field with a set of amplitude and phase information is captured at the reference plane. The unit cell implementation will be discussed in detail in CHAPTER 3.

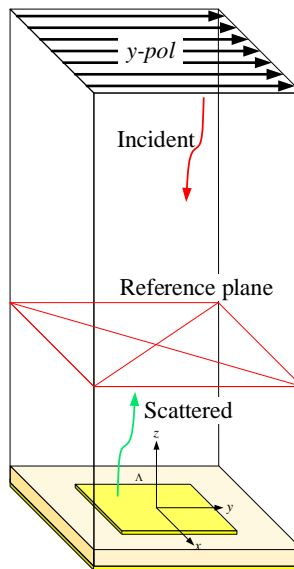
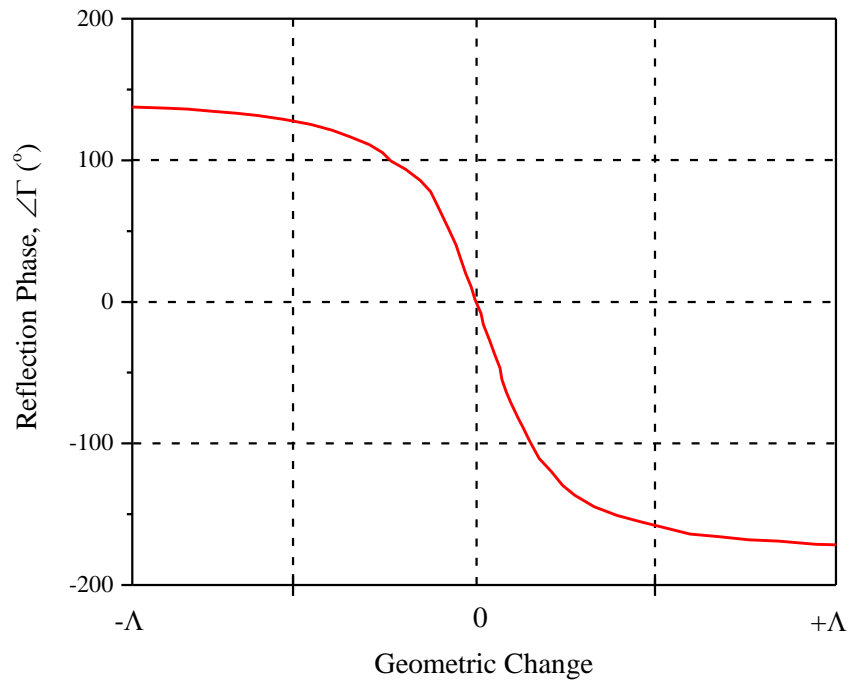


Figure 2.12: 3D model of Floquet cell with a  $y$ -polarized electric field excitation.

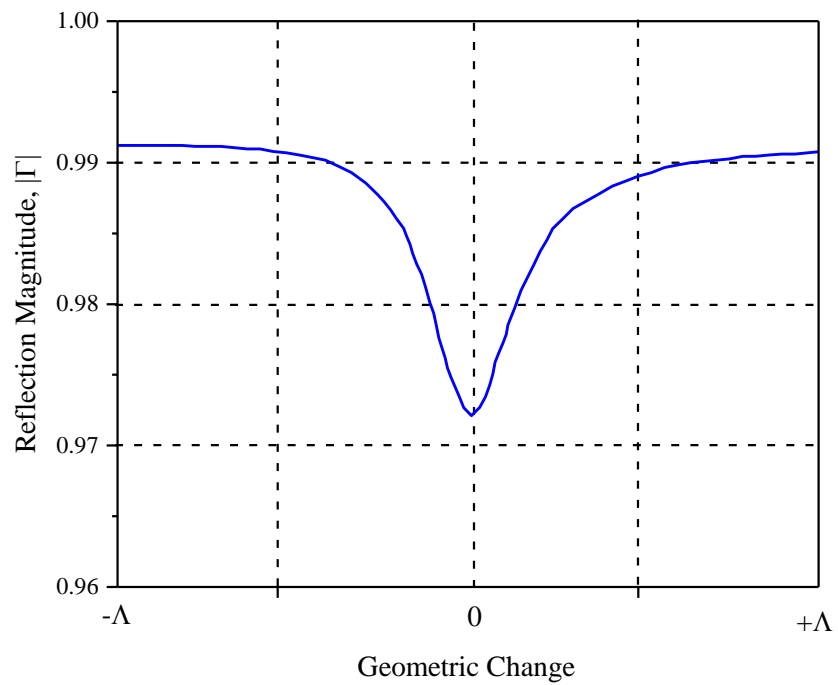
## 2.9 Element Reflection Phase Curve

As discussed previously, the analysis and design of a reflectarray involve the utilization of the reflection phase curves obtained from the unit cell simulation. These phase curves correlate the phases from the reflectarray element through geometrical parameter changes. A good reflectarray element design should be capable of achieving a  $360^\circ$  reflection phase range with low reflection loss. The reflection phase and its corresponding magnitude can be derived from the reflection coefficient ( $\Gamma$ ) versus element geometrical parameter change ( $\Lambda$ ), which is generally an S-shaped curve with a nonlinear relationship (Huang and Encinar, 2008). Figure 2.13 shows a reflection phase response of a variable-size square patch element.

When a wave impinges on the reflectarray element, all energy will be scattered back due to the presence of a ground plane under an ideal condition (Rajagopalan et al., 2012). However, some losses are usually introduced by the reflectarray element itself, and they are primarily comprised of metallic ohmic loss and dielectric loss (Bozzi et al., 2004). The loss tangent and thickness of a substrate can also significantly affect the reflection characteristics (Rajagopalan and Rahmat-Samii, 2010). The information on reflection loss can be obtained from the magnitude of the reflection coefficient in the unit cell simulation at a particular frequency. In general, the loss factor should be minimised when designing a reflectarray.



(a)



(b)

Figure 2.13: Typical reflection coefficient of a reflectarray element as a function of the geometrical parameter change. (a) Reflection phase,  $\angle\Gamma$ , and (b) Reflection magnitude,  $|\Gamma|$ .

## 2.10 Element Design Consideration

As discussed in Section 1.3, the bandwidth of reflectarray is primarily limited by the narrow bandwidth of the radiating element and the spatial phase delays associated with the feed distance to the element. For a medium or small-size reflectarray, the bandwidth performance is mainly associated with the element design and substrate thickness (Bialkowski and Sayidmarie, 2008).

Two main parameters of the phase characteristics are important in the phase compensation process. One is the phase range, and the other is the phase curve gradient (or slope). In order to provide suitable compensation for every element on the reflectarray without approximation errors, the phase range needs to be  $> 360^\circ$  at a given frequency. This phase error can be avoided with the use of stacked patches or multi-resonance configurations (Encinar, 2001; Vosoogh et al., 2014). Practically, fabrication tolerance plays an important role, as it can introduce random phase errors to the flatness of the array elements (Pozar et al., 1997). A slower phase slope is less sensitive to tolerance errors, thus offering smaller manufacturing errors. Also, the phase slope is responsible for a larger operational bandwidth of the phase-shifting element (Bozzi et al., 2003). A smooth phase slope with a low gradient can be obtained using a double-stack configuration or by increasing the substrate thickness (Encinar, 2001; Bialkowski and Sayidmarie, 2008). The two types of phase errors will cause the gain and the efficiency to reduce (Chaharmir et al., 2003).

The reflection coefficient of the reflectarray element is essentially frequency-dependent (Huang, 1995b; Pozar, 2003), leading to a phase curve that varies with frequency. Besides, the reflectarray element is chosen to provide the necessary phase compensation at the design frequency. Thus, when operating at the other frequency, the required phase compensation as well as the reflection phase response of the reflectarray element will change. A mismatch of the two phases, which is usually the case, will result in gain reduction and bandwidth limitation when designing the reflectarray. The phase error is suggested to be no more than  $\sim 45^\circ$  from the nominal frequency (Bozzi et al., 2003). For a moderate-size reflectarray, the phase-shifting (radiating) element design is the most significant factor in determining the element bandwidth. However, it is well known that the microstrip reflectarray element has a narrow bandwidth of around a few per cents (Huang and Encinar, 2008). In turn, it limits the operational bandwidth of the reflectarray. In order to overcome the element's bandwidth limitation, the design of the phase-shifting element has to produce a smooth phase curve with good linearity. This can be achieved using a thick substrate with low dielectric constant (Bozzi et al., 2003) or a multi-resonant configuration (Moustafa et al., 2011).

Furthermore, the reflection phase of the reflectarray element is dependent not only on the individual geometry but also on the mutual coupling between the adjacent elements. The mutual coupling level varies with the inter-element spacing (Karnati et al., 2012). From Karnati's work, it has been shown that a closer inter-element spacing causes a higher mutual coupling level, leading to a change in the resonant frequency to become more pronounced. The

frequency shift renders a change in the reflection phase in the element as well as the corresponding reflection phase curve. Also, as the inter-spacing increases, variation in both the resonant frequency and phase becomes smaller due to the reduction in mutual coupling level. Moreover, the electric field distribution closely resembles individual element's radiation, which is less affected by its adjacent elements. When the inter-spacing is larger than  $0.6\lambda$ , the effect of the spacing on the resonant frequency of the element is relatively less. An efficient method to overcome the abrupt geometry variation between the adjacent elements in the conventional design was proposed using an I-shaped dipole covered with a circular ring (Chen et al., 2013). This approach achieves almost equal mutual coupling between the adjacent elements, improving the bandwidth performance of the reflectarray.

Conventionally, an element spacing of around  $0.5\lambda$  at the centre design frequency is expected to produce a reflection phase curve with a suitable phase slope and sufficient phase dynamic range. Nevertheless, all elements in the reflectarray must have proper spacing between adjacent elements to avoid grating lobes (Huang and Encinar, 2008). The spacing requirement is governed by the conventional array relation and is expressed as:

$$\frac{d}{\lambda} \leq \frac{1}{1 + \sin \theta_i} \quad (2.27)$$

where  $d$  is element spacing and  $\theta_i$  is the incident angle from the feed to the element. For an offset feed configuration, a spacing of much larger than  $0.5\lambda$  is



more susceptible to grating lobe issues. A large focal distance ratio  $F/D$  could help to minimise the grating lobe issue.

## **2.11 Conclusion**

The bandwidth performance of a moderate-sized reflectarray largely depends on the element's structure. Hence, exploring new elements for obtaining a good reflection phase performance and achieving a wider bandwidth in the reflectarray is crucial and necessary. Most reflectarray elements need to be optimised to meet the performance requirements. Typically, the analysis is performed using simulation software, such as CST Microwave Studio, and it is simulated over a frequency range of interest. Iterative simulations and design optimizations can be performed on the reflectarray elements. When translated to full-fledged reflectarray, a broadband performance can be realised.

## CHAPTER 3

### DESIGN METHODOLOGY

#### 3.1 Design Method

A practical approach for designing a reflectarray requires the proper selection of the right phase tuning method in the element design for achieving a linear and broad phase response. The full-fledged reflectarray is then synthesised using this phase information and optimised for its farfield performance. The overall design flow is illustrated in Figure 3.1.

The element design begins with defining the configuration and its geometrical dimensions. The element design has to provide appropriate phase-shifting geometrical changes to achieve a sufficient phase range and linearity. The unit element modelling is carried out using the commercial full-wave 3D electromagnetic analysis software, CST Microwave Studio<sup>®</sup> (CST MSW), and modelled using a Floquet cell (Section 2.8). The reflection phase curve (S-curve) and amplitude are then derived from the reflection coefficient ( $S_{11}$  parameter). Parametric analysis is then carried out to analyse the reflection performance. This element design process repeats until the optimised parameters are obtained, where a broad linear phase curve with a slow gradient and low reflection loss is achieved.

The next step is the reflectarray design, which starts with determining the aperture size and feed location. With these inputs, the required reflection phase shift of each element on the reflectarray used for the phase delay compensation can be determined. The phase-shifting parameters of the element can then be extracted from the reflection phase curve (S-curve) and used to synthesise a full-fledged reflectarray model. Parametric analysis of the reflectarray performance, including radiation pattern, gain, efficiency, bandwidth, cross-polarization, and side lobe level (SLL), is then carried out. This reflectarray design process repeats until reflectarray performance is optimised.

Lastly, a prototype is fabricated using the standard PCB fabrication technology and assembled with the feeding source. The radiation pattern and antenna gain are then measured to verify the prototype's performance with the simulation results. Each step of the design process shown in Figure 3.1 will be explained in the following sections.

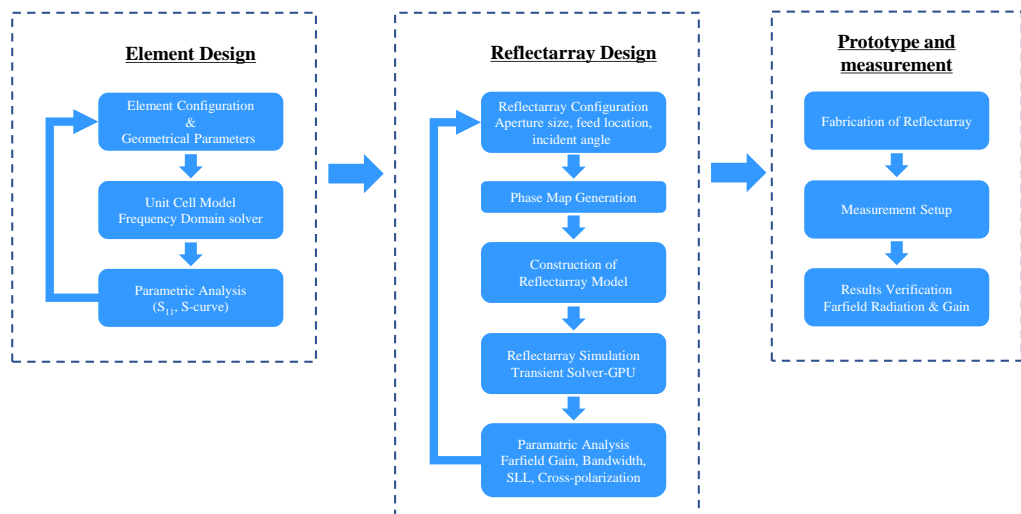


Figure 3.1: Design flow of a reflectarray antenna.

### 3.2 Unit Element Design

The unit element simulation is carried out using the unit cell model. As mentioned previously, designing an appropriate phase-shifting element is vital in the process of reflectarray design. The element must provide an adequate phase response to compensate for the spatial delay as well as the desired progressive phase to form a collimated beam in a particular direction.

Typically, the unit element is square in shape, and the size is kept within  $0.5\lambda$  to avoid grating lobes issues (Huang and Encinar, 2008). An example (Rajagopalan et al., 2012) of a unit element of variable size square patch, with the phase-shifting parameter change of patch width ( $\Lambda_x = \Lambda_y = \Lambda$ ) and element size of  $L_x = L_y$ , is shown in Figure 3.2. The unit cell model is implemented using the CST Microwave Studio<sup>®</sup> (Figure 3.3 (a)). The wave port ( $Z_{\max}$ ), located 80 mm from the reference plane ( $\boxtimes$ ), excites a linearly polarized plane wave (TE<sub>00</sub> mode), impinging obliquely on the unit element (Figure 3.3 (b)). The reflection properties of the unit element are monitored by de-embedding the Floquet port onto the unit element surface (Figure 3.3 (c)). Figure 3.3 (d) shows the periodic boundary condition used in the CST Microwave Studio<sup>®</sup>, with the unit cell repeating itself infinitely. Once the unit cell model is configured correctly, the phase-shifting parameter is pre-configured for the parametric sweep. The Frequency Domain Solver is used to simulate the unit cell across the frequency band of interest. The reflection coefficient ( $\Gamma$ ) information is then obtained from the  $S_{11}$  parameters.

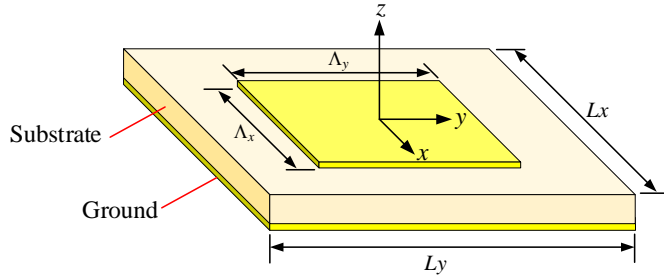


Figure 3.2: Square patch unit element.

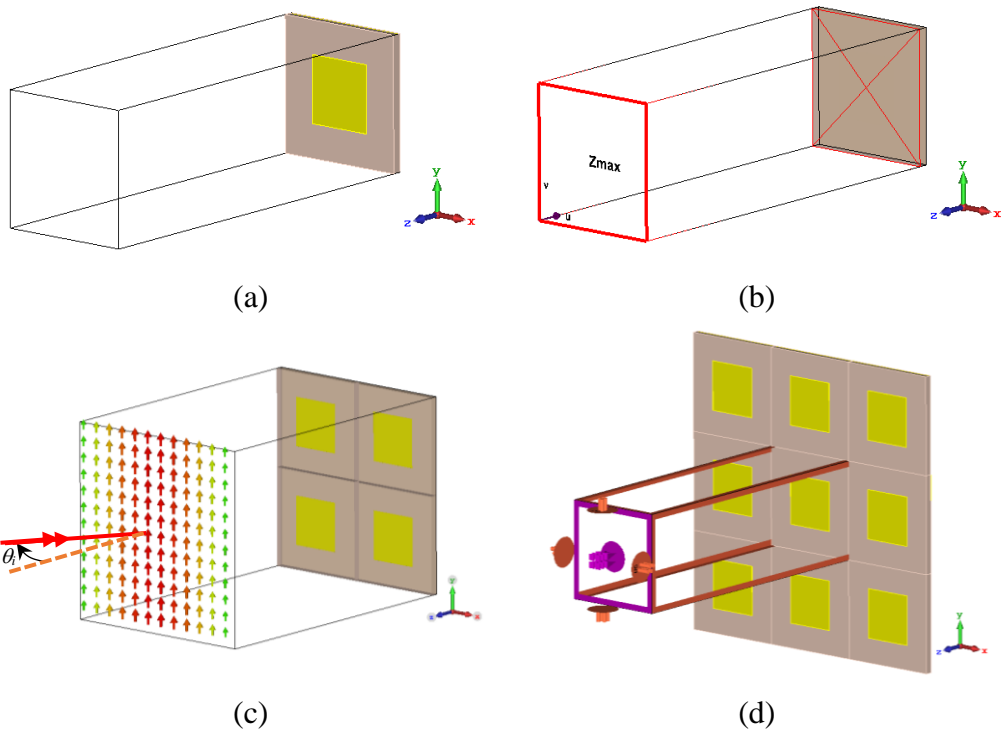


Figure 3.3: Unit cell model in CST Microwave Studio. (a) Square patch unit element in a bounding box. (b) Floquet port with de-embedding onto the element surface. (c) Linearly polarized plane wave incident on the element. (d) Floquet cell boundaries.

A MATLAB<sup>®</sup> program is developed to post-process the reflection phase and magnitude of the  $S_{11}$  parameters. The post-processing flow is illustrated in Figure 3.4. The  $S_{11}$  parameters, which are frequency-dependent,

are exported and followed by the generation of the reflection phase curves and amplitudes. Figures 3.5 (a)(i) and (b)(i)) show the  $S_{11}$  parameters for the phase and magnitude of the square patch element at different values of  $\Lambda$ . The extracted S-curve ( $\angle S_{11}, \Lambda$ ) and reflection amplitude profile ( $|S_{11}|, \Lambda$ ), according to the frequencies of interest, are shown in Figures 3.5 (a)(ii) and (b)(ii), respectively.  $\Lambda$  is varied from 7 – 11 mm to achieve a phase range of  $\sim 360^\circ$  at the design frequency of 10 GHz.

The parametric analysis will then be carried out to optimise the reflection phase curves to cover a broad phase range with a low phase gradient. In addition, the unit element should provide a reflection loss as low as possible, typically lower than -1-dB, which implies that the power incident on the reflectarray is mostly reflected.

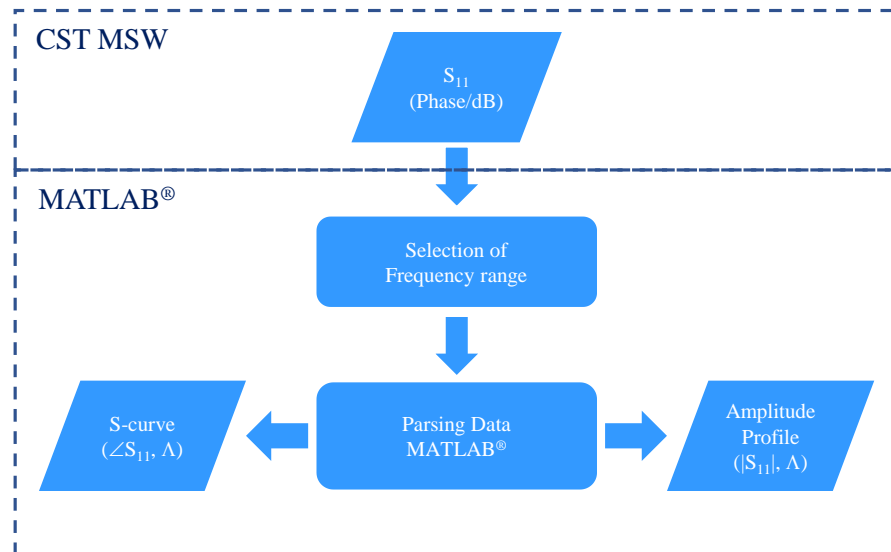


Figure 3.4: Flow chart for the  $S_{11}$  parameter post-processing.

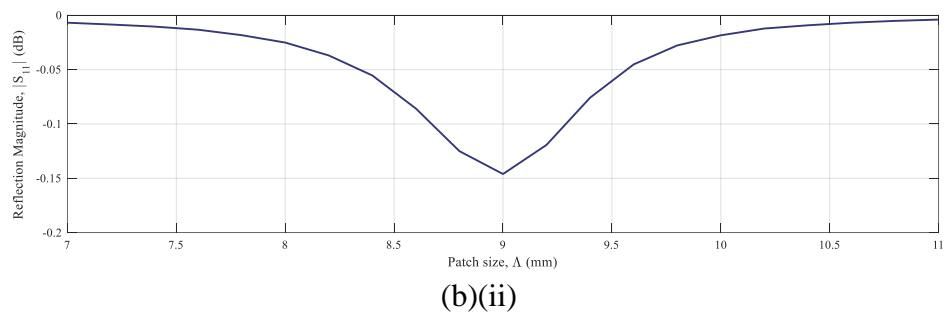
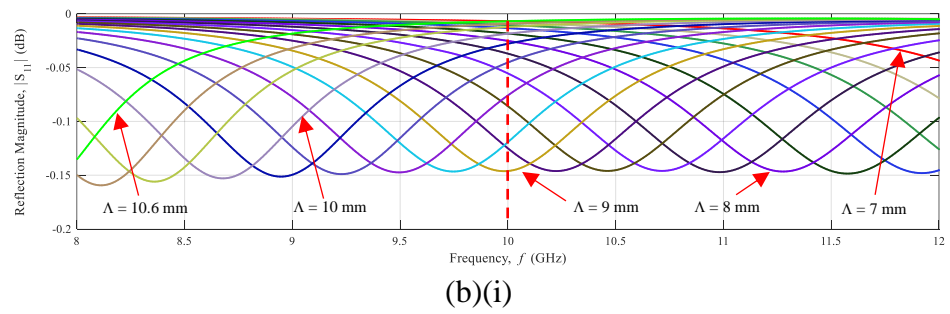
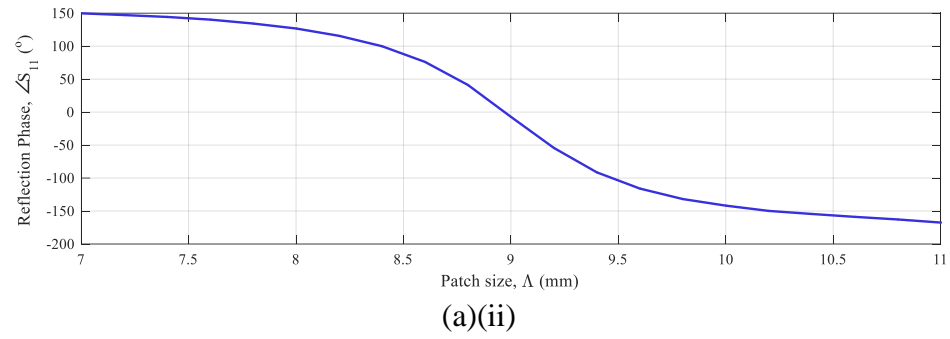
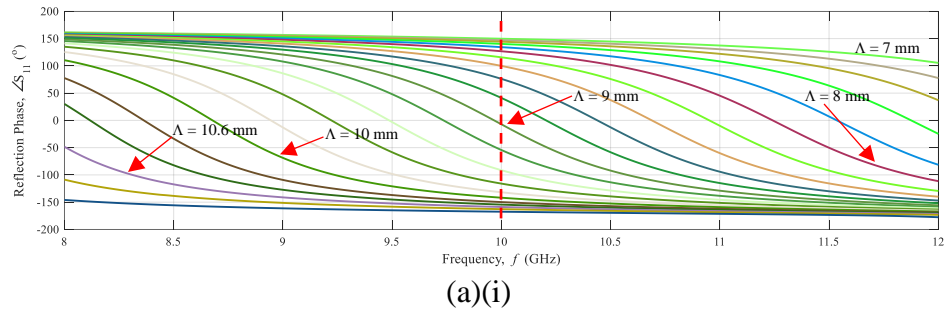


Figure 3.5:  $S_{11}$  parameter results and post-processed reflection responses vs phase-shifting parameter at the frequency of 10 GHz. (a) Reflection phase, and (b) reflection amplitude.

### 3.3 Reflectarray Configuration Design

In this research, to achieve a moderately high gain and for design simplicity, we have selected a square aperture with a moderate size based on our available fabrication facilities. Figure 3.6 shows the side view of a reflectarray configuration, which is described following the definition in Section 2.6. The reflectarray is designed with an offset feed to minimise blockage. The feed antenna is usually a horn located at a focal distance  $F$  from the centre point of the radiation aperture, at an angle of  $\theta_i$  to the normal. All the elements on the aperture must be be located at the farfield distance to the phase centre of the horn. The feed horn's focal distance  $F$  is also associated with the aperture dimension  $D$  of the reflectarray, which follows the design consideration discussed in Section 2.4.4.

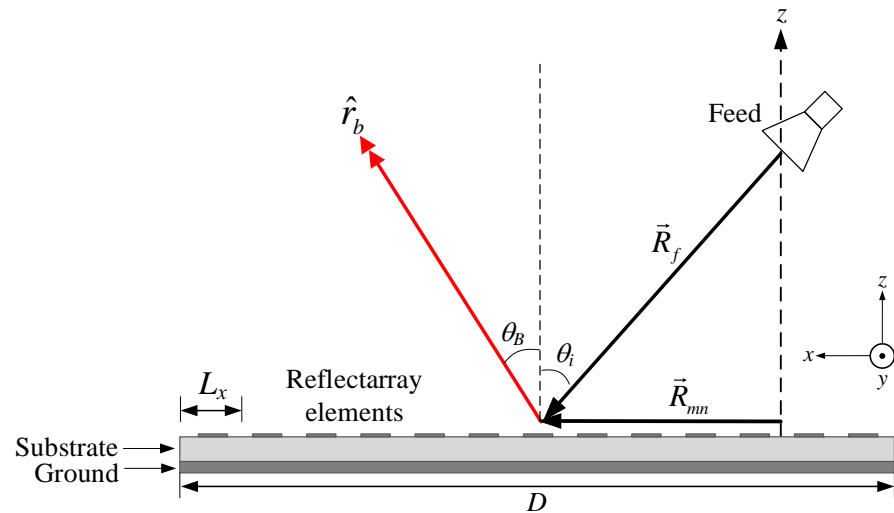


Figure 3.6: Side view of a reflectarray configuration.



The building of a reflectarray model involves two major steps. First is the phase map generation, followed by constructing a 3D reflectarray model, as illustrated in Figure 3.7.

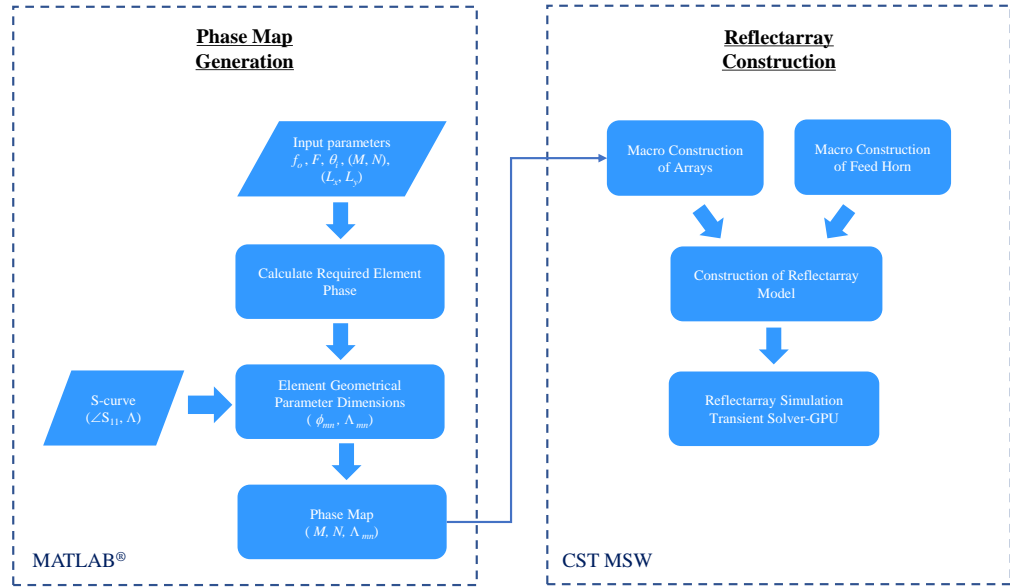


Figure 3.7: Flow chart of the phase map generation and construction of a 3D reflectarray model in CST Microwave Studio®.

The reflectarray aperture size is calculated according to the number of arrays ( $M \times N$ ) multiplied by the element size. Note that the element is a square shape with a dimension of  $L_x = L_y$ , giving a square antenna aperture. Figure 3.8 shows the grid layout for the array used for deriving the required phase shift ( $\phi_{mn}$ ) on the reflectarray aperture. Here, the design is mainly focused on configuring a broadside radiation normal to the aperture with a direction angle of  $\theta_B = 0^\circ$ , making  $\hat{r}_B \equiv \hat{z}$ . Therefore, the required phase compensation only depends on the spatial phase delay, and it can be determined using Equation (2.26). A MATLAB® program is developed to extract the phase-shifting parameter from the S-curve to synthesise the required phase shift ( $\phi_{mn}$ ) for all

the elements on the reflectarray aperture. A phase map ( $M, N, \Lambda_{mn}$ ) is generated according to the reflectarray's aperture size ( $D$ ), feed focal distance ( $F$ ), and incident angle ( $\theta_i$ ). The example of a calculated phase map for an offset angle feed configuration is shown in Figure 2.11 (b). Next, the CST Microwave Studio<sup>®</sup> is invoked to run the Macro scripts (CST MSW Macro) to construct the arrays and incorporate the feed horn accordingly. An example of the reflectarray model using the square patch element is shown in Figure 3.9.

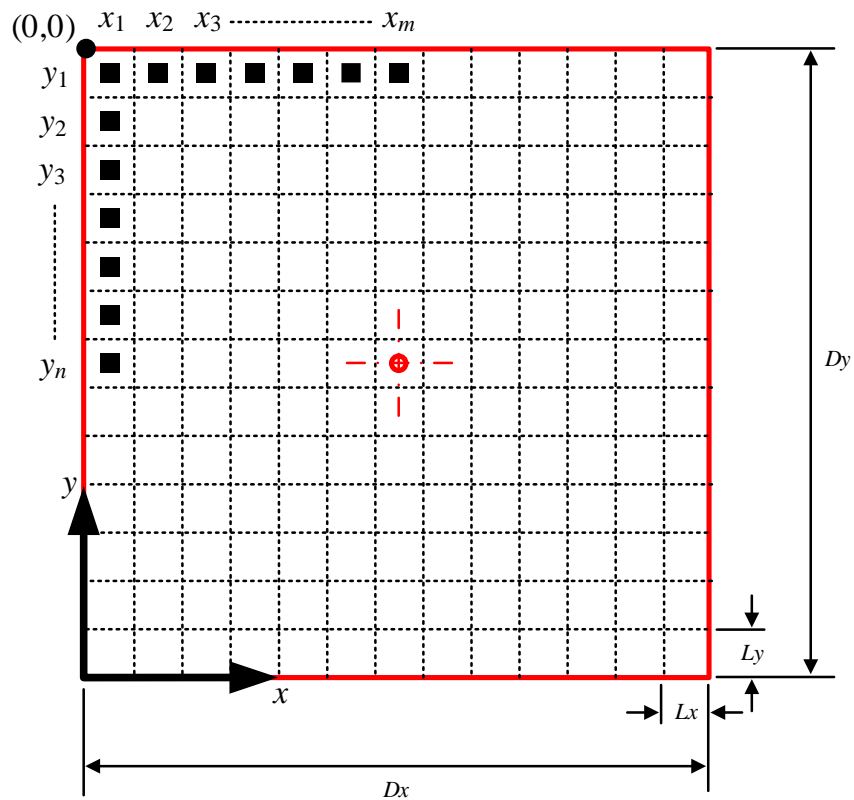


Figure 3.8:  $13 \times 13$  grid layout for the arrays.

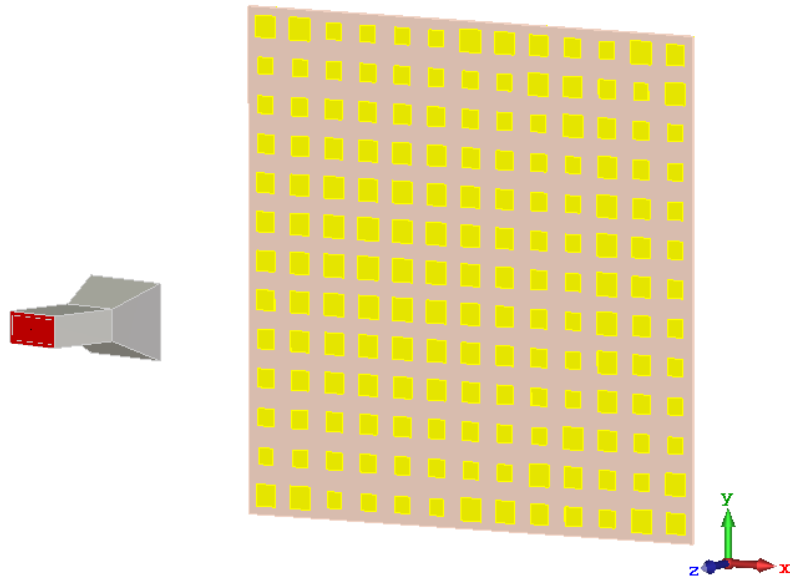


Figure 3.9: Full 3D reflectarray model.

A full-wave simulation using the Time-domain Solver across the frequency band of interest is performed, and the farfield radiation patterns are modelled through “Fields Monitor”. The antenna gain is then obtained using a Farfield Post-processing template to extract the farfield results from the Field Monitors in the broadside direction. The reflectarray configuration's parametric analysis, such as incident angle and  $F/D$ , will be performed to achieve optimum performance. A high-speed workstation Dell Precision T7610 (Dual Intel (R) Xeon ® CPU with 32 GB RAM) with the NVIDIA Tesla K80 (GPU computing supported) is used to perform all the simulations.

### 3.4 Measurement Method

The measurement setup is shown in Figure 3.10. The radiation patterns and antenna gains are measured in a free-space environment. A rotating table is used to position the reflectarray under test (RUT). The RUT is powered by a signal generator, Rohde & Schwarz SMB100A (100 kHz -12.75 GHz), connected to a feed horn for transmitting the microwave signals, with a power ( $P_t$ ) of 10 dBm at the desired frequency. At the receiving end, a linearly polarized (LP) C-band (ATM PNR137-440-2, 5.85 GHz – 8.2 GHz) or X-band (XB-HA90-18-SMA, 8.2 GHz – 12.9 GHz) pyramidal horn is used and connected to a spectrum analyser Advantest U3771 (9 kHz – 31.8 GHz) to receive the power ( $P_r$ ) from the RUT. The measurement devices are controlled through a laptop using the LAN remote connection to control the signal transmission and acquisition of reception data to display on the spectrum analyser.

The distance between the receiving horn and the RUT is at farfield with  $R > 2D^2/\lambda$ , where  $D$  is the diagonal dimension of the RUT. The RUT is directed facing at  $+z$  and rotated in the azimuth ( $\theta$ ) direction to measure the radiation patterns at all angles. The received power is directly recorded from the spectrum analyser at each elevation angle. The Friss transmission equation is then applied to compute the antenna gain (Balanis, 2005). A 3D view of the farfield radiation pattern generated from the CST Microwave Studio<sup>®</sup> is illustrated in Figure 3.11.

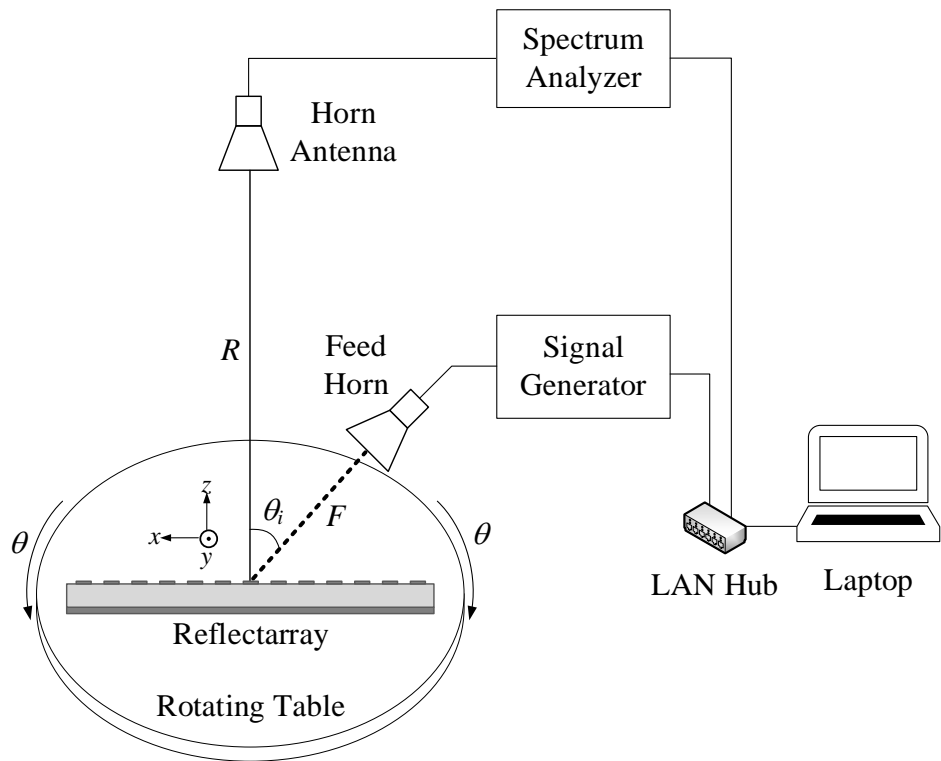


Figure 3.10: Measurement setup for a reflectarray.

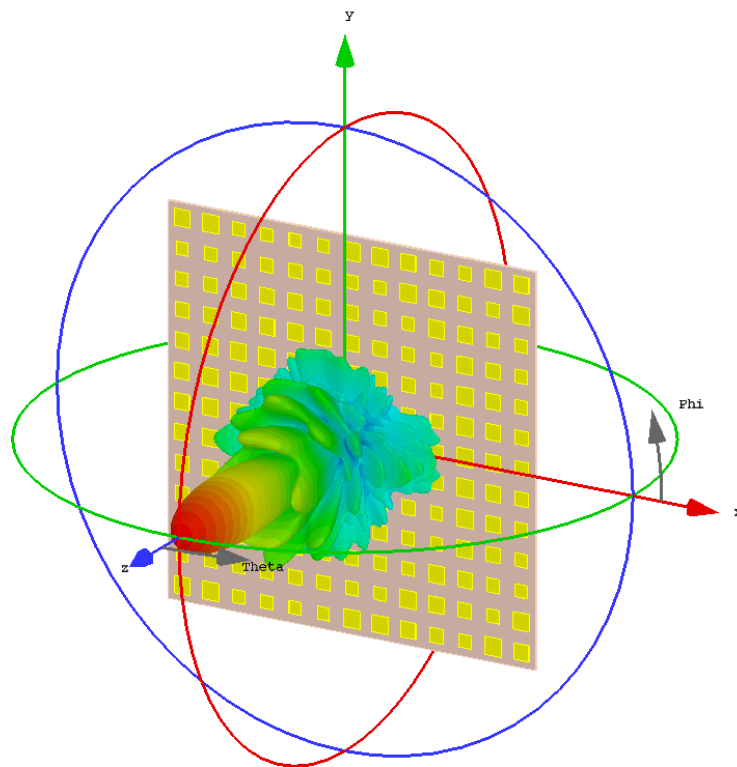


Figure 3.11: 3D view of the farfield radiation in the CST Microwave Studio®.

### **3.5 Conclusion**

Practically, designing a reflectarray requires proper selection of the right phase tuning method in the element design for achieving a linear and broad phase response. The analysis and optimisation of the reflectarray element can be carried out through iterative simulation to achieve optimum phase response. The full-fledged reflectarray is then synthesised using this optimum phase information and optimised for its farfield performance. Measurement of the farfield performance is then carried out to verify the simulation results.

## CHAPTER 4

### VIVALDI TAPERED SLOT REFLECTARRAY LOADED WITH DUMBBELL-SHAPED RING RESONATOR

#### 4.1 Introduction

In this chapter, a dumbbell-shaped square ring is combined with a Vivaldi tapered slot antenna (TSA) for designing a reflectarray for the first time. The TSA is a travelling-wave radiator that radiates in the end-fire direction at the wider end of the slot (Gibson, 1979). Extensive studies have been carried out to analyse and optimise the performances of the Vivaldi antenna array due to its wide-band and wide-scanning characteristics (Chio and Schaubert, 2000; Kasturi and Schaubert, 2006; Shin and Schaubert, 1999). Here, by incorporating the travelling-wave radiator of the Vivaldi tapered slot antenna, it is able to overcome the limitation of the conventional square ring structure and has enabled the proposed reflectarray element to achieve a full phase range with linear and low phase sensitivity simultaneously. By changing the ring size, this new design enables the generation of a phase range of more than  $360^\circ$ . A broad bandwidth with good aperture efficiency can be realised when the element translated into a full-fledged reflectarray.

## 4.2 Reflectarray Unit Element

Figure 4.1 shows the configuration of the unit element, which composes of a Vivaldi tapered slot antenna on one side and a dumbbell-shaped microstrip ring resonator on the other, fabricated on a single piece of RO4003C substrate ( $t = 0.8128$  mm,  $\varepsilon_r = 3.38$ , and  $\tan\delta = 0.0027$ ). The substrate is then placed vertically along the centreline of a rectangular ground plane, as shown in Figure 4.1 (a). With reference to Figure 4.1 (b), the Vivaldi tapered slot antenna consists of a circular slot cavity and an exponentially increasing tapered slot, which are interconnected by a short slotline ( $L_S$ ). The dimensions of the slotline are  $W_{SL}$  and  $L_S$ , and it is terminated with a circular slot cavity (with diameter  $D_{SL}$ ) positioned at a backwall offset distance  $L_g$  from the ground plane. Given the opening rate  $R$  and two coordinates  $P_1(y_1, z_1)$  and  $P_2(y_2, z_2)$  (Shin and Schaubert, 1999), as shown in Figure 4.1 (b), the curve profile of the tapered slot can be described by the following mathematical function:

$$y(z) = c_1 e^{Rz_1} + c_2 \quad (4.1)$$

$$\text{where } c_1 = \frac{y_2 - y_1}{e^{Rz_2} - e^{Rz_1}} \text{ and } c_2 = \frac{y_1 e^{Rz_2} - y_2 e^{Rz_1}}{e^{Rz_2} - e^{Rz_1}}.$$

The profile length  $L_T$  of the taper region is  $z_2 - z_1$ , and the aperture width  $H$  is  $2(y_2 - y_1) + W_{SL}$ . Larger antenna gain is attainable by increasing the profile length of this type of travelling-wave radiator, with the price of enlarging the footprint. The optimum parameters of the tapered slot are  $H = 8$  mm,  $W_{SL} = L_S = 0.5$  mm,  $D_{SL} = 3$  mm,  $L_g = 6$  mm,  $L_T = 10.5$  mm, and  $R = 0.3$  (Shin and

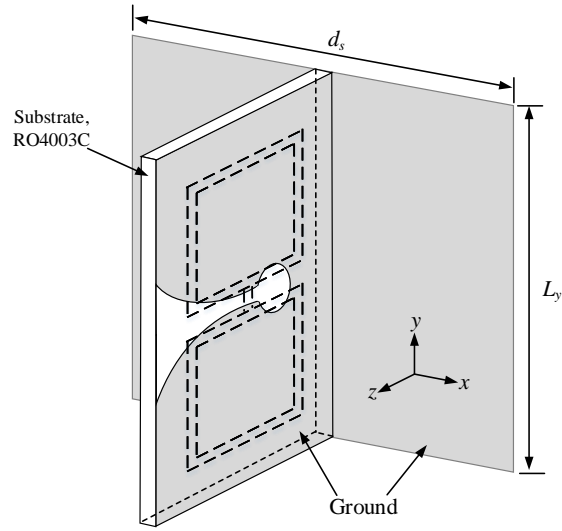


Schaubert, 1999; Wang et al., 2010). The total height  $h$  of the element is 20 mm ( $0.43\lambda_o$  at  $f_o = 6.5$  GHz). For a Vivaldi tapered slot antenna to work in the travelling condition, its effective dielectric thickness can be determined using the following equation (Schaubert et al., 1985):

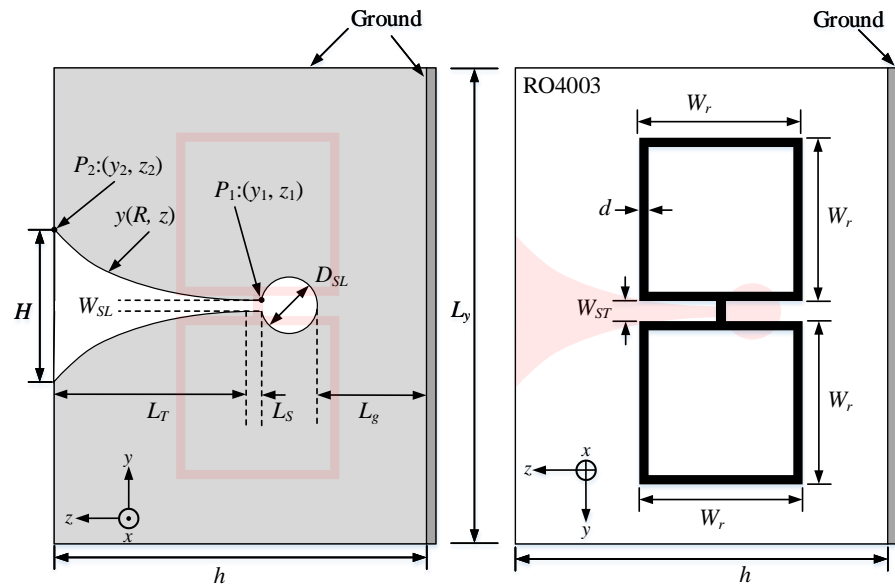
$$t_{eff} = (\sqrt{\epsilon_r} - 1)t \quad (4.2)$$

The thickness must be in the range of  $0.005\lambda_o - 0.03\lambda_o$ . In this design,  $t_{eff} = 0.015\lambda_o$ .

The dumbbell-shaped microstrip ring resonator is composed of two square rings ( $W_r$ ) which are interconnected by a section of short stripline ( $d = 0.5$  mm) with a length of  $W_{ST} = 1.0$  mm. The dumbbell is placed on the other side of the substrate with the short stripline positioned perpendicular to the Vivaldi slotline. The signal is coupled from the stub-loaded rings to the Vivaldi tapered slot antenna through the stripline-slotline coupling mechanism. In the design, the two microstrip rings function as the phase-shifting geometrical parameter where the desired phase range is obtained by varying the ring width  $W_r$  from 2.0 mm to 8.2 mm. Table 4.1 summarises the design parameters, and their parametric analysis can be found in Section 4.5.1.



(a)



(b)

Figure 4.1: (a) Exploded view of the proposed unit element, and (b) top and bottom views of the Vivaldi tapered slot antenna loaded with a dumbbell-shaped microstrip ring resonator.

Table 4.1: Design Parameters.

Parameter	Values	Parameter	Values
$t$	0.813 mm	$h$	20 mm
$H$	8.0 mm	$L_y$	25 mm
$L_S$	0.5 mm	$d_s$	25 mm
$W_{SL}$	0.5 mm	$R$	0.3
$D_{SL}$	3.0 mm	$W_r$	2.0 – 8.2 mm
$L_g$	6.0 mm		

The proposed unit element is simulated using Floquet cell in the CST Microwave Studio<sup>®</sup> simulation environment, as shown in Figure 4.2. The unit element is placed at one end of the Floquet cell while a linearly  $y$ -polarized plane wave is launched from the wave port (Port 1) at the other end with an incident angle of  $\theta_i = 20^\circ$ . The unit element is located at a distance of 80 mm from the wave port. In the simulation, the reference plane is de-embedded from the wave port to the top surface of the radiating aperture, which is shown in dotted lines in Figure 4.2. The unit cell size is designed to be  $L_y = d_s = 25$  mm ( $0.54\lambda_0$  at  $f_0 = 6.5$  GHz), which will be translated into the spacing of the elements later to avoid generating grating lobes.

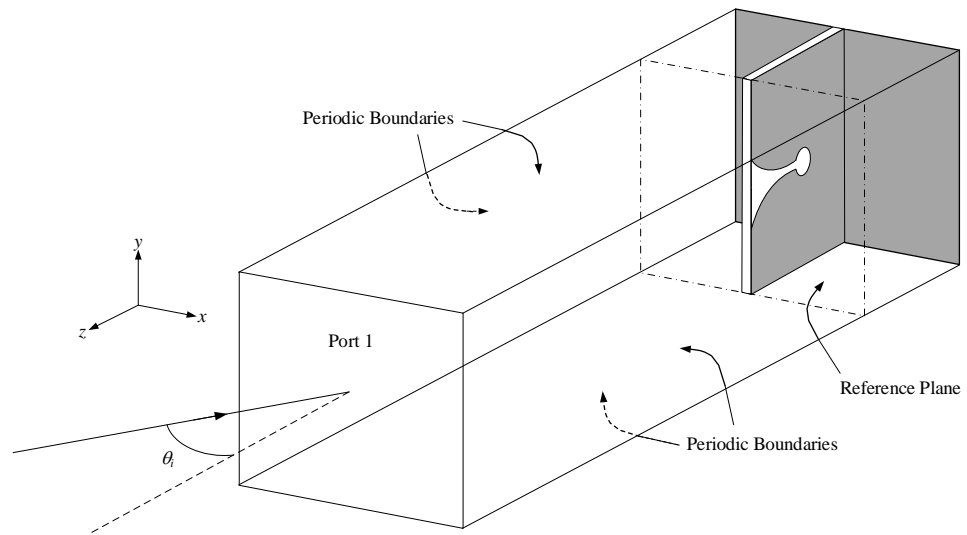


Figure 4.2: Simulation model of the Vivaldi tapered slot unit element in a Floquet cell.

By varying the ring width  $W_r$  from 2.0 mm to 8.2 mm, the reflection phase curves and amplitudes at the incident angle of  $\theta_i = 20^\circ$  with the wave frequency varied from 6.1 GHz to 6.7 GHz of the proposed unit element are plotted in Figure 4.3. A reflection phase range of  $371^\circ$  has been achieved, with

the reflection amplitude kept less than -0.5 dB at the design frequency  $f_o = 6.5$  GHz. Linear and slow-changing gradient in the phase curve is achieved for the entire  $W_r$  range, with an average phase sensitivity of  $64.6^\circ/\text{mm}$ , which can be difficult to be met by the conventional ring and patch reflectarray element. Usually, these conventional designs have phase sensitivities larger than  $90^\circ/\text{mm}$  (Bialkowski and Sayidmarie, 2008; Yoon et al., 2015). Combining multiple resonators in a single-layered structure is able to increase the phase range, but this comes with the price of increasing the phase sensitivity. Low phase sensitivity is good for reducing the fabrication errors of the elements. With reference to Figure 4.3, smooth curves with slow gradients are obtained at all frequencies, implying the proposed element has a wide bandwidth (Encinar, 2001). Also observed in the same figure is that the reflection amplitudes are generally less than 0.5 dB in all the curves. Figure 4.4 shows the effects of the incident angle ( $\theta_i$ ) on the phase response. For all cases, the reflection phase curves are quite linear, with the phase range being  $> 360^\circ$ . Because of the use of the travelling-wave radiator, the proposed unit element is able to achieve full phase range and low phase sensitivity simultaneously, which are difficult to be obtained by the conventional methods (Bialkowski and Sayidmarie, 2008; Costa and Monorchio, 2012; Yoon et al., 2015).

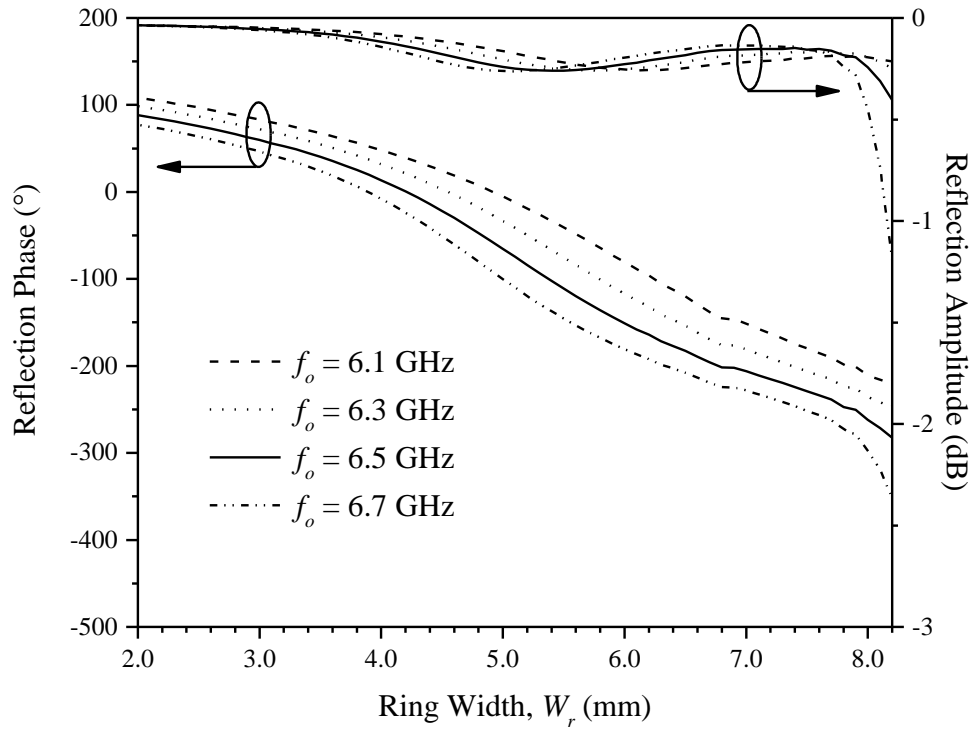


Figure 4.3: Reflection amplitude and phase responses as a function of ring width  $W_r$  for different wave frequencies at the incident angle of  $\theta_i = 20^\circ$ .

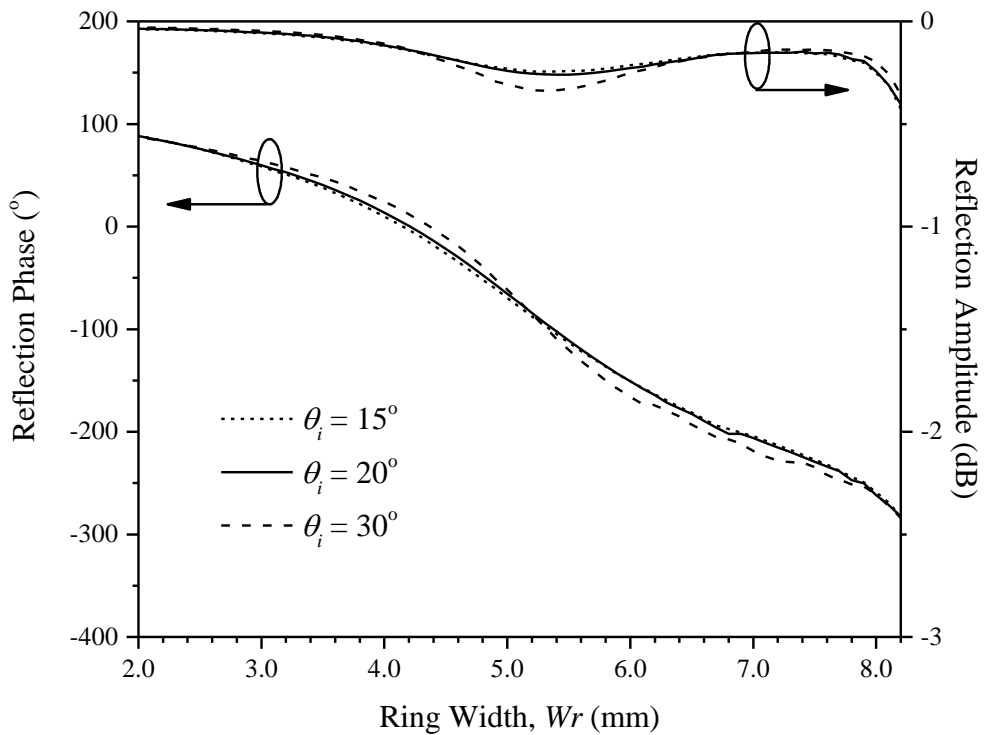
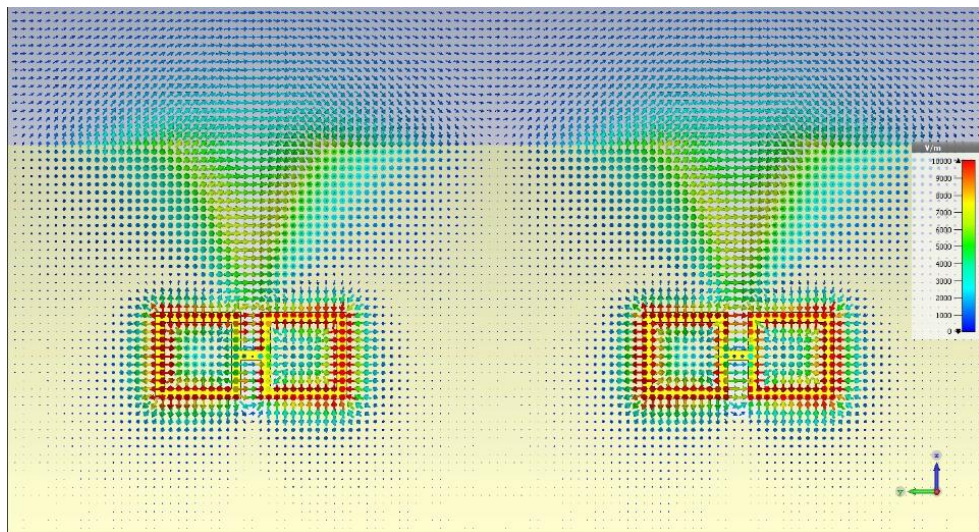
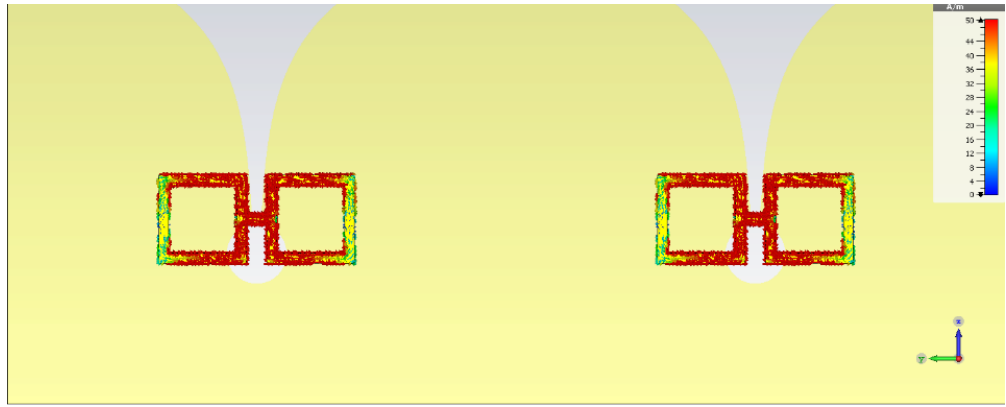


Figure 4.4: Reflection amplitude and phase responses for different incident angles ( $\theta_i$ ) at  $f_o = 6.5$  GHz.

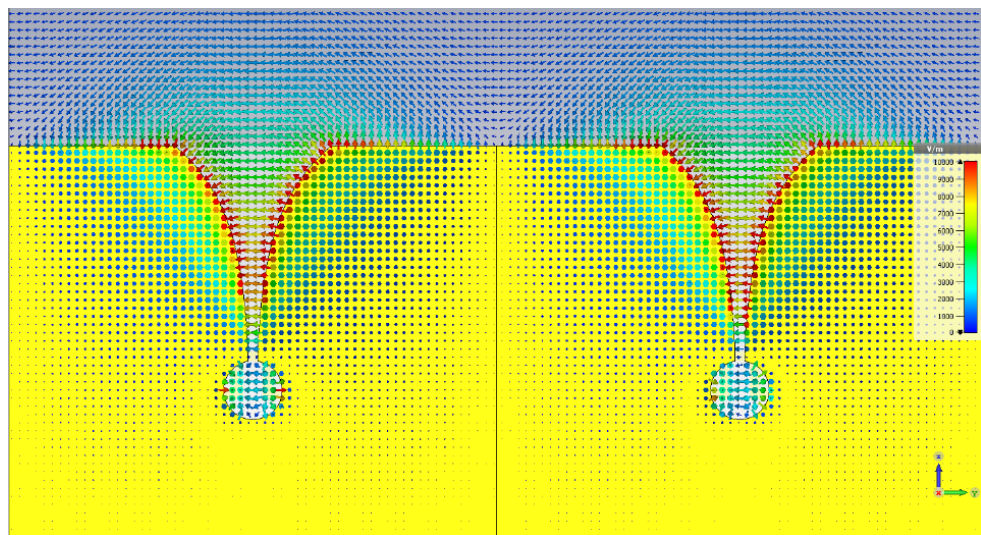
The electric field and current distributions for the case of  $W_r = 4.4$  mm are studied and depicted in Figure 4.5. In this case, the circumference of the stub-loaded ring is 17.6 mm, which corresponds to the resonant frequency of  $\sim 6.5$  GHz. Figures 4.5 (a) and (c) show the electric fields on the dumbbell-shaped microstrip ring resonator and the Vivaldi tapered slot antenna at 6.5 GHz. One standing wave is observed in each of the rings in Figure 4.5 (a), showing that the stub-loaded ring (Chang and Hsieh, 2004) resonates in its dominant mode ( $\lambda_g/2$ ) at this frequency, where  $\lambda_g$  is the guided wavelength. The resonant behaviour is confirmed by the strong surface current distribution, as shown in Figure 4.5 (b). At the same frequency, electric fields and current distribution are shown in Figures 4.5 (c) and (d) around the radiating aperture of the tapered slot. The wave coming from the port induces electric fluxes parallel to the slot, and the energy is later coupled from the slotline to the dumbbell-shaped rings through the stripline. Since both the rings resonate, only waves with selected frequencies can be coupled back to the slotline and re-radiated through the Vivaldi tapered slot antenna.



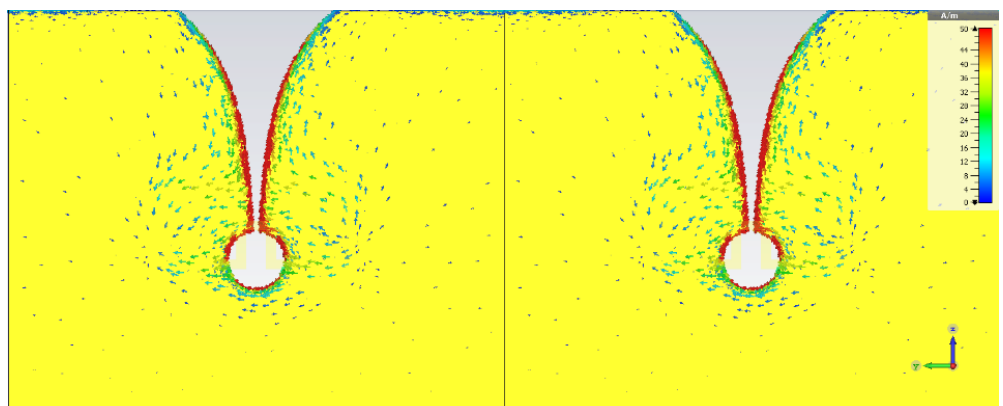
(a)



(b)



(c)

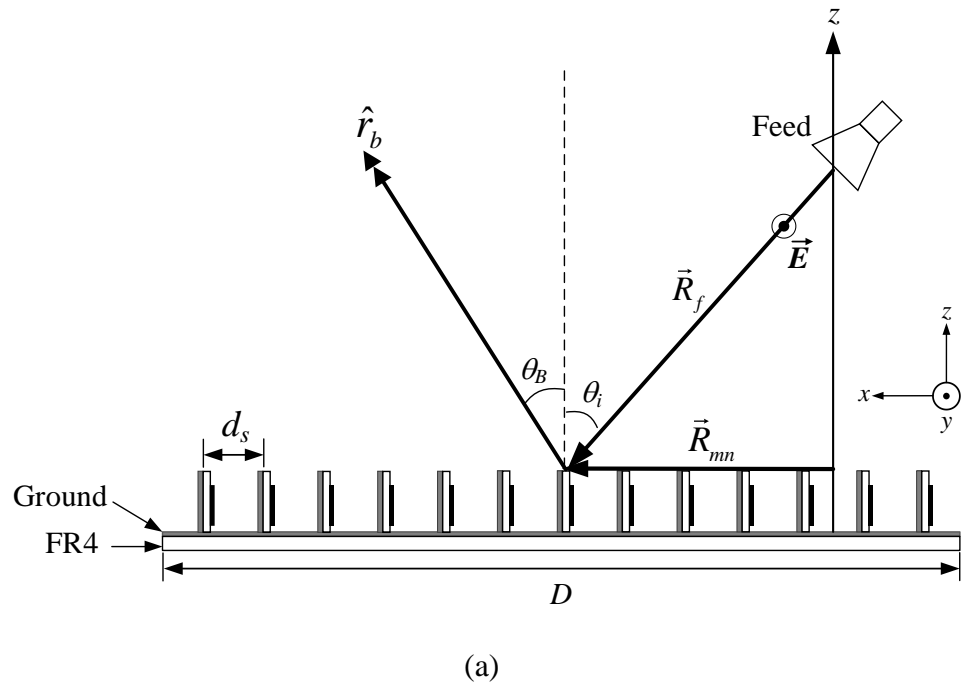


(d)

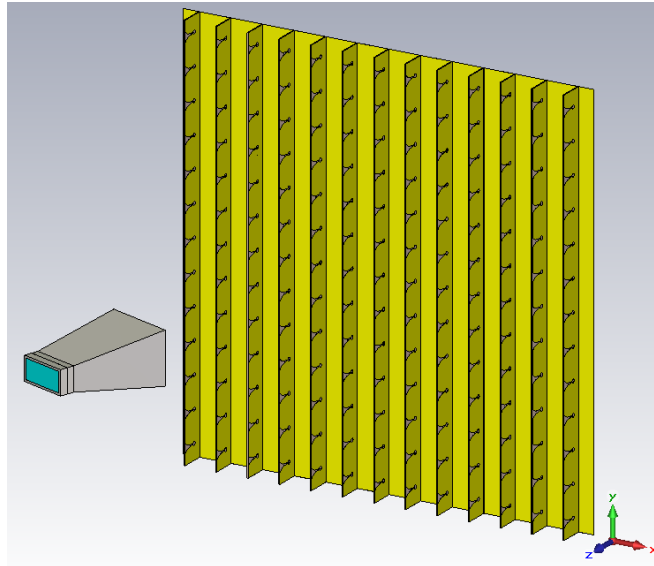
Figure 4.5: (a) Electric field and (b) surface current distributions on the dumbbell-shaped microstrip ring resonator; (c) Electric field and (b) surface current distributions on the Vivaldi tapered slot antenna at 6.5 GHz, for the ring width of  $W_r = 4.4$  mm.

### 4.3 Reflectarray Design Configuration

The proposed reflectarray element is then employed to design a  $13 \times 13$  reflectarray composed of 169-unit elements. The side view of the proposed reflectarray antenna is illustrated in Figure 4.6 (a), with the simulation model shown in Figure 4.6 (b). The reflectarray aperture is square in shape and has a total dimension of  $D = 13L_y = 325$  mm. The feeding horn is suspended at a farfield distance of  $F = 210$  mm and an incident angle of  $\theta_i = 20^\circ$  from the centre point of the aperture, yielding an  $F/D$  ratio of 0.65. The offset feeding method can minimise the feeder blockage. Underneath the ground, a FR-4 (thickness: 1.57 mm) is used as the structural support, and simulation shows that it does not affect the performance of the reflectarray.







(b)

Figure 4.6: (a) Side view of the proposed reflectarray with a feeding horn suspended at  $\theta$ . (b) Simulation model of the full-fledged reflectarray in CST Microwave Studio<sup>®</sup>.

A linearly polarized C-band pyramidal horn antenna, a commercial ATM PNR137-440-2 (5.85 GHz – 8.2 GHz), is used as the feeding source. It has a dimension of 51.31 mm ( $H$ )  $\times$  37.59 mm ( $E$ ), with a flare length  $F_L = 73.5$  mm, as shown in Figure 4.7. Figure 4.8 shows the simulated 3D farfield radiation pattern of the feed horn. The simulated antenna gain has a nominal value of 9.97 dBi in both the  $E$ - and  $H$ - planes at 6.5 GHz. The horn has a simulated 3-dB beamwidth of  $54.7^\circ$  and  $59.5^\circ$  in  $E$ - and  $H$ - planes, respectively, as shown in Figure 4.9. The inset in Figure 4.9 shows the cosine- $q$  model radiation pattern plot. The average  $E$ - and  $H$ - planes 2D radiation pattern matches the cosine- $q$  model pattern up to about  $\pm 30^\circ$  with the value of  $2q_f \approx 6$ . The phase centre of the horn is 2.7 mm below the opening aperture throughout this angular range.

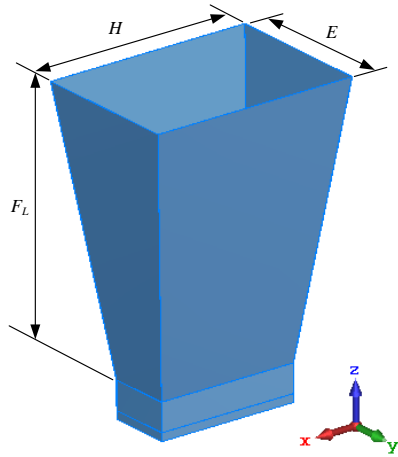


Figure 4.7: Simulation model of C-band pyramidal horn antenna.

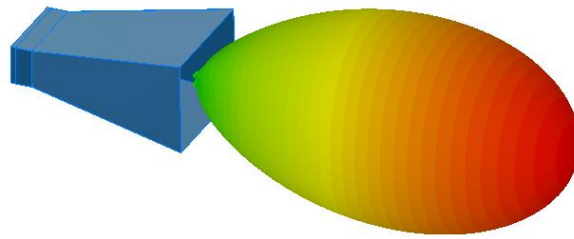


Figure 4.8: A 3D farfield plot of the C-band pyramidal horn antenna.

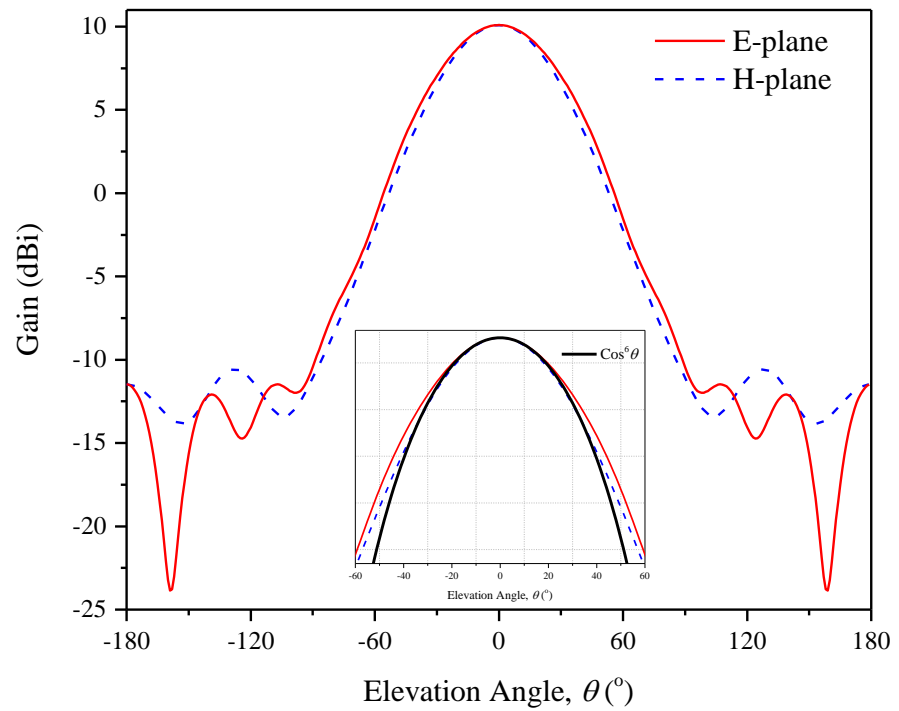


Figure 4.9: Radiation patterns of the C-band pyramidal horn antenna: 2D and cosine- $q$  model.

The proposed linear polarized reflectarray is designed to radiate in the boresight direction ( $\theta_B = 0^\circ$ , Figure 4.6 (a)). The desired phase shift for each element can be calculated using Equation (2.26). The corresponding geometrical dimensions for all phase-shifting elements on the reflectarray aperture can then be extracted from the reflection phase curve, which is shown in Figure 4.3. Figure 4.10 shows the phase distributions of all elements that are used to synthesise the reflectarray. The construction and simulation of the full 3D model (Figure 4.6 (b)) are then carried out using CST Microwave Studio<sup>®</sup>.

A prototype is fabricated and shown in Figure 4.11. The arrays are fabricated on a piece of RO4003 and cut into strips. The strip of arrays is then arranged upright on the ground in rolls. A couple of properly trimmed foam boards (with  $\epsilon_r \sim 1$ ) are used to hold the elements on the ground. Figures 4.11 (a) and (b) show the dumbbell-shaped microstrip ring resonator arrangement and the Vivaldi tapered slot antenna orientation. The conductive area of the tapered slot is shorted to the ground using 3M copper tapes. The top view of the prototype attached to the rotating table is shown in Figure 4.11 (c).

Next, the fabricated prototype is measured using the experimental setup described in Section 3.4. A linearly polarized C-band pyramidal horn (ATM PNR137-440-2 ,5.85 GHz – 8.2 GHz) located at farfield is used as a receiving horn. It is connected to a spectrum analyser (Advantest U3771) for recording purposes. The farfield distance is  $R = 12$  m. The reflectarray is directed at  $+z$  and rotated in the azimuth direction to enable the measurement of radiation patterns at all angles (Figure 3.10).

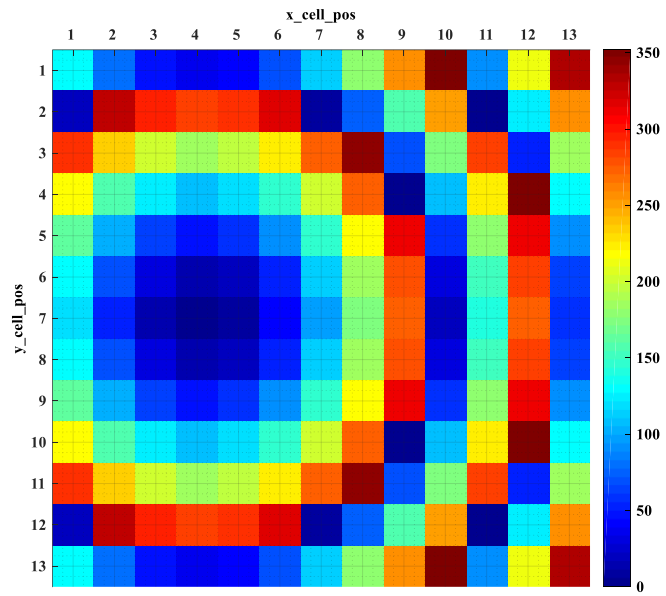
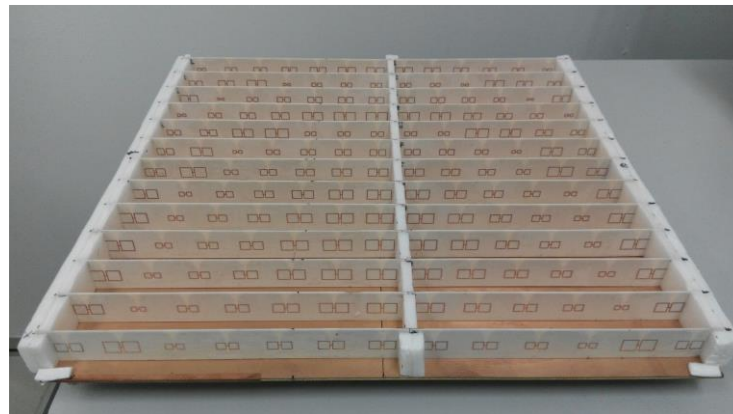
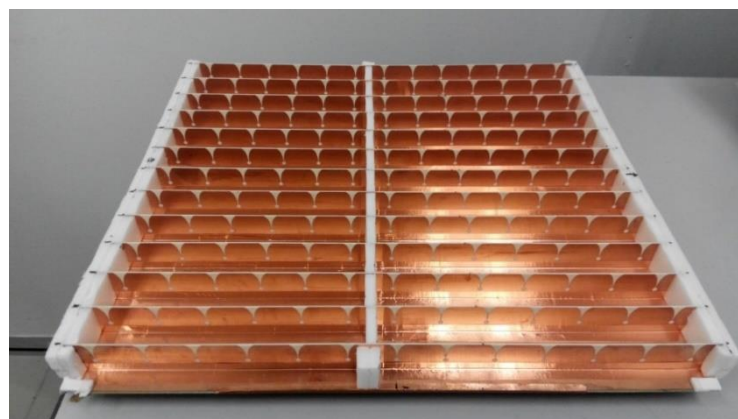


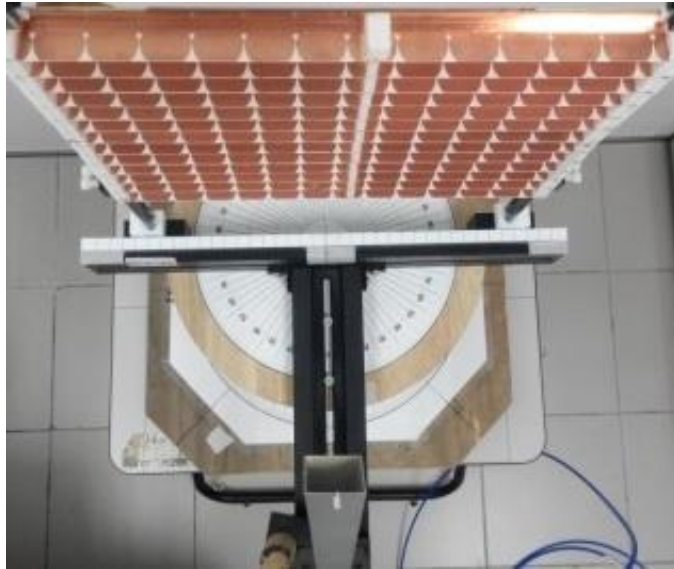
Figure 4.10: Phase distributions on the proposed reflectarray.



(a)



(b)

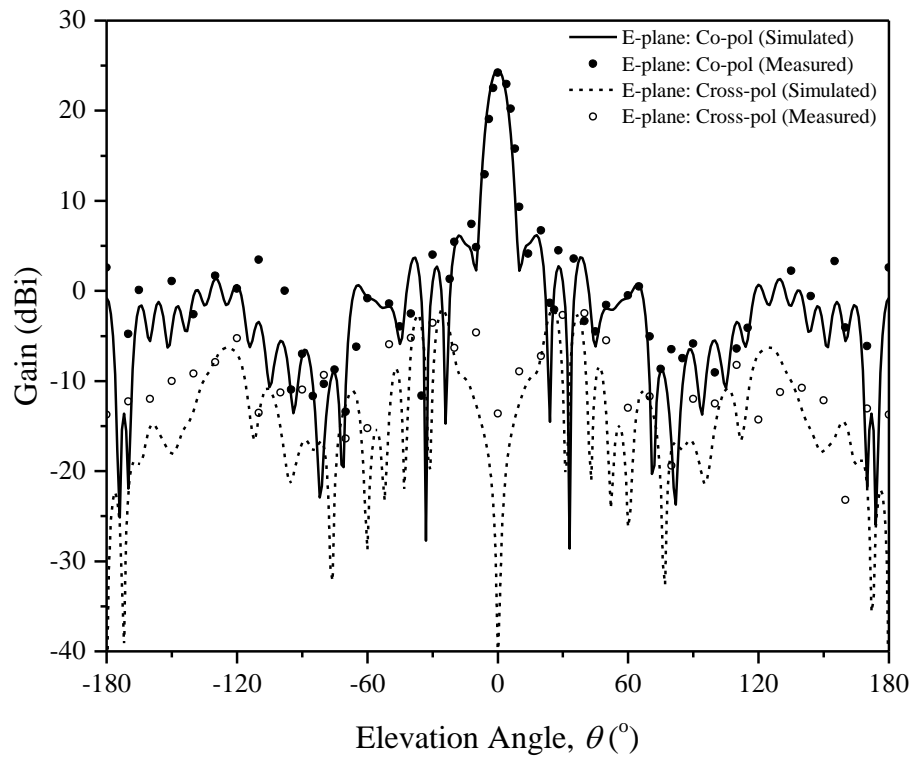


(c)

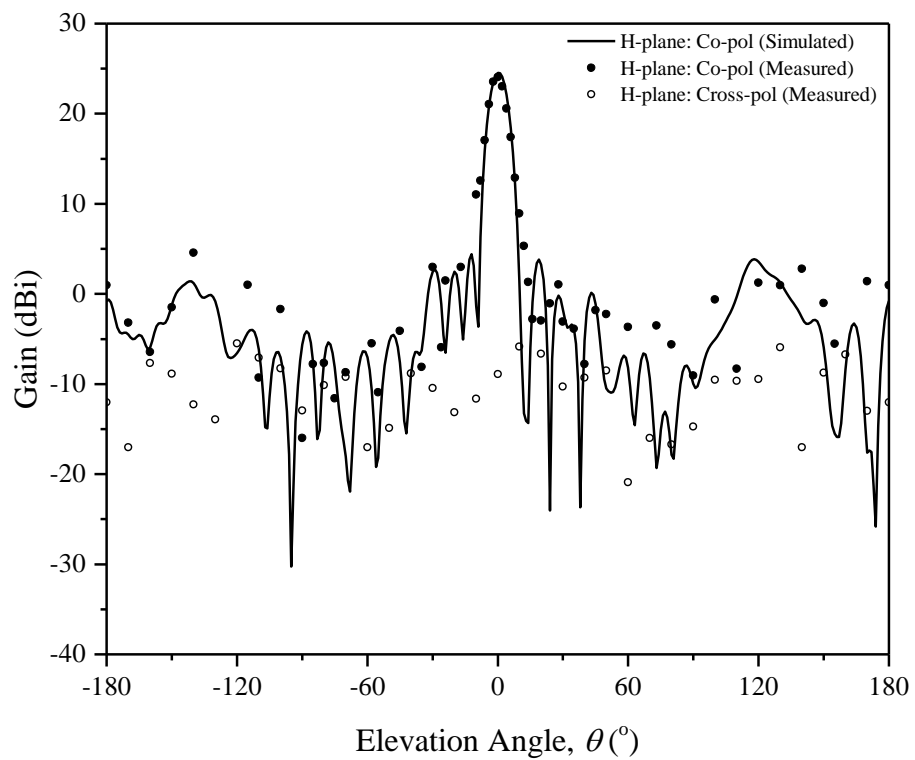
Figure 4.11: Prototype of the proposed reflectarray viewed from different directions. (a) dumbbell-shaped microstrip ring resonator, (b) Vivaldi tapered slot antenna, and (c) top view of the prototype attached to the rotating table.

#### 4.4 Results and Discussion

Figure 4.12 shows the measured and simulated radiation patterns in the  $E$  ( $yz$ -plane) and  $H$  ( $xz$ -plane) planes at 6.6 GHz. Good agreement has been observed between simulation and measurement results, with the sidelobe level (SLL) lower than that in the boresight by at least 18 dB. Also, the cross-polarized radiation field is found to be at least 20 dB lower than the co-polarized one in the boresight. The simulated cross-polarized field curve is not shown in the  $H$ -plane as all data points are much less than -30 dB.



(a)



(b)

Figure 4.12: Measured and simulated (a) *E*- and (b) *H*- plane radiation patterns of the proposed reflectarray at 6.6 GHz.

Figure 4.13 shows the measured and simulated antenna gains in the boresight, where good agreement is observed. The measured and simulated maximum antenna gains read 24.1 dBi and 24.5 dBi, respectively, at 6.6 GHz. The optimum measured aperture efficiency is calculated to be 40.4%, which is slightly lower than its simulation counterpart of 44.3%. The simulated radiation efficiency is found to be 99.4%. As can be seen from Figure 4.13, the proposed reflectarray has a measured -1-dB gain bandwidth of 10.6% (simulation: 11.2%), covering 6.05 GHz - 6.75 GHz (simulation: 6.1 GHz - 6.84 GHz).

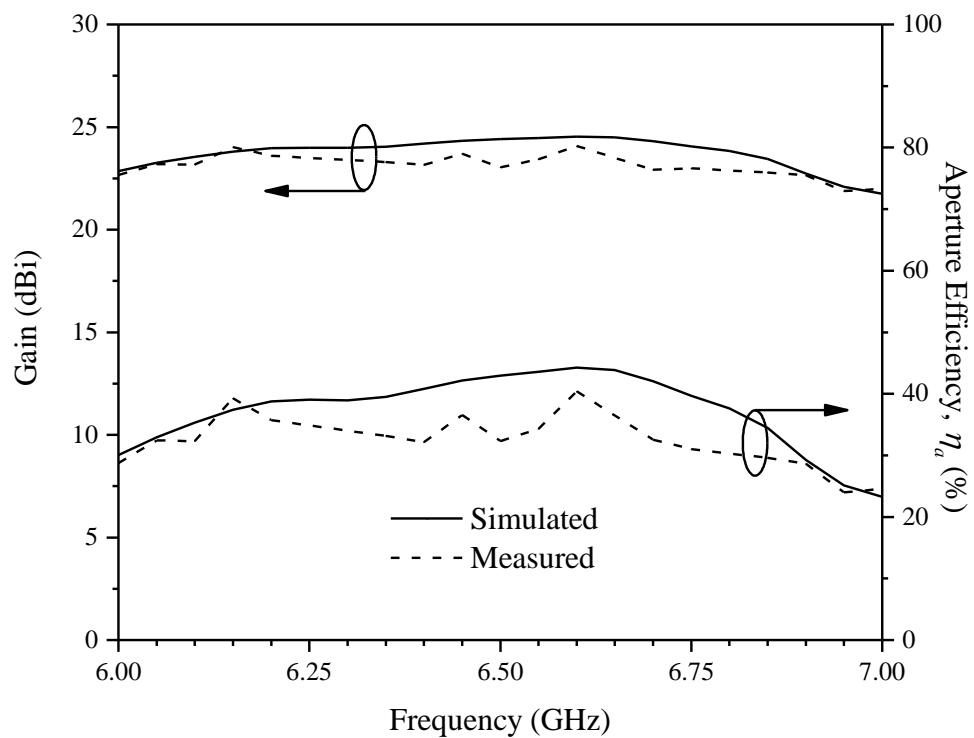


Figure 4.13: Measured and simulated radiation gains and aperture efficiencies of the proposed reflectarray as a function of frequency.

## 4.5 Parametric Analysis

Parametric analysis is performed to study the characteristics of the proposed unit element and reflectarray to achieve optimum performance. Details of their analysis will be discussed in the following Section 4.5.1 and Section 4.5.2, respectively.

### 4.5.1 Unit Element Reflection Phase

Simulations have been conducted to study the effects of crucial design parameters on the reflection characteristics of the unit element reflection characteristics at design frequency  $f_o = 6.5$  GHz. In this analysis, the dumbbell-shaped microstrip ring resonator geometrical parameters are fixed at  $d = 0.5$  mm and  $W_{ST} = 1$  mm with the element size  $L_y = 25$  mm. The Vivaldi tapered slotline section is fixed at  $W_{SL} = L_s = d$  for proper coupling. Therefore, the parametric analysis is focused on  $h$ ,  $L_g$ ,  $D_{SL}$ ,  $H$ , and  $R$ .

Figure 4.14 shows the effect of total height  $h$  with the remaining geometrical parameters:  $L_g = 6$  mm,  $D_{SL} = 3$  mm,  $H = 8$  mm, and  $R = 0.3$ . In the proposed unit element design,  $h = L_t + L_s + D_{SL} + L_g$ . Hence, changing the total height is equivalent to changing the tapered profile length  $L_t$ . It can be seen that the height of the Vivaldi antenna deviates from 20 mm, and the reflection amplitude is not much affected. However, the phase curve gradient starts to deteriorate.



Next, the backwall offset distance  $L_g$  is changed while keeping  $h = 20$  mm,  $D_{SL} = 3$  mm,  $H = 8$  mm, and  $R = 0.3$ . In this case, the tapered profile length  $L_t$  decreases by increasing the offset distance  $L_g$ . Increasing the offset distance  $L_g$  causes the phase gradient to rise, as shown in Figure 4.15. It is observed that when  $Wr$  is at the larger end, the reflection amplitude is at the higher side.

With the optimum values of  $h = 20$  mm and  $L_g = 6$  mm and kept  $H = 8$  mm and  $R = 0.3$ , the circular slot cavity diameter  $D_{SL}$  is varied accordingly, as shown in Figure 4.16. By increasing or reducing  $D_{SL}$  from 3 mm, the phase gradient starts to degrade with a slight increase in reflection amplitude. This is consistent with the effect obtained from the  $h$  and  $L_g$ , whereby changing the  $D_{SL}$  changes the tapered profile length  $L_t$  and affects the phase gradient accordingly. Therefore, it can be seen that the optimum total height  $h$  and offset distance  $L_g$  are 20 mm and 6 mm, respectively, which is converted to tapered profile length  $L_t = 10.5$  mm.

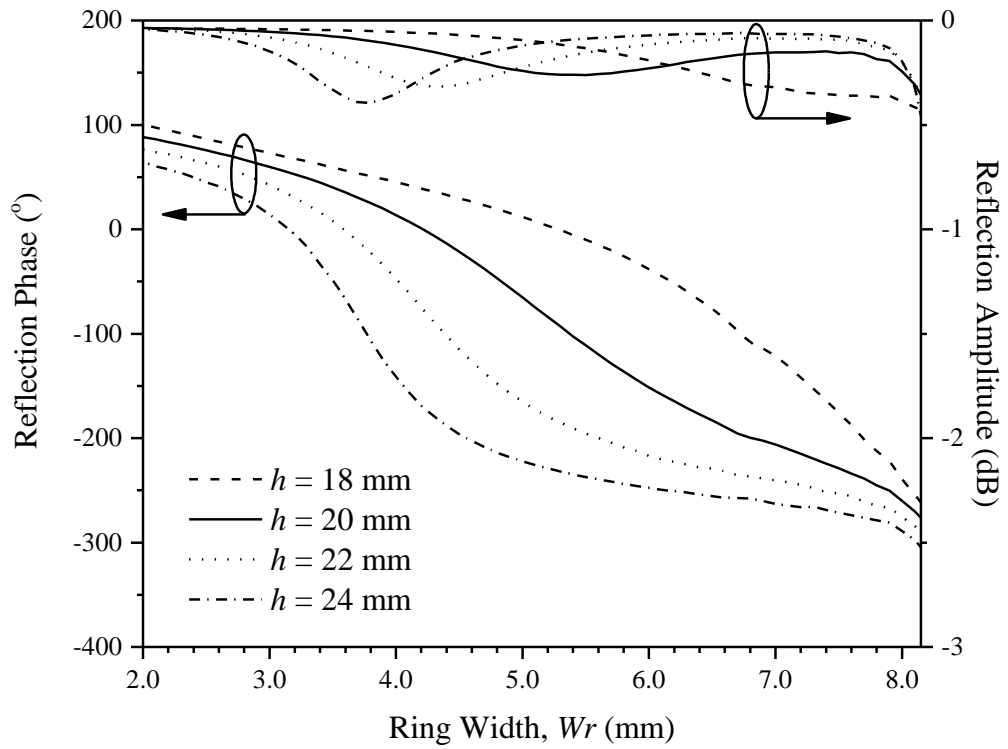


Figure 4.14: Effect of total height  $h$  on the reflection amplitude and phase responses at the incident angles  $\theta_i = 20^\circ$  and  $f_o = 6.5$  GHz.

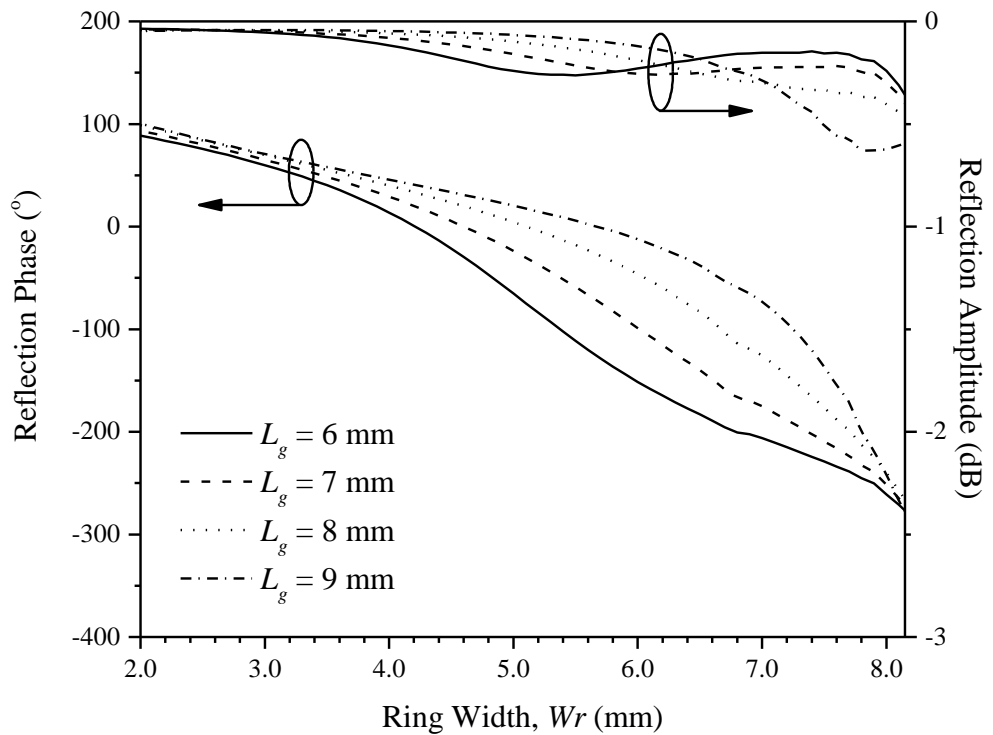


Figure 4.15: Effect of backwall offset distance  $L_g$  on the reflection amplitude and phase responses at the incident angles  $\theta_i = 20^\circ$  and  $f_o = 6.5$  GHz.

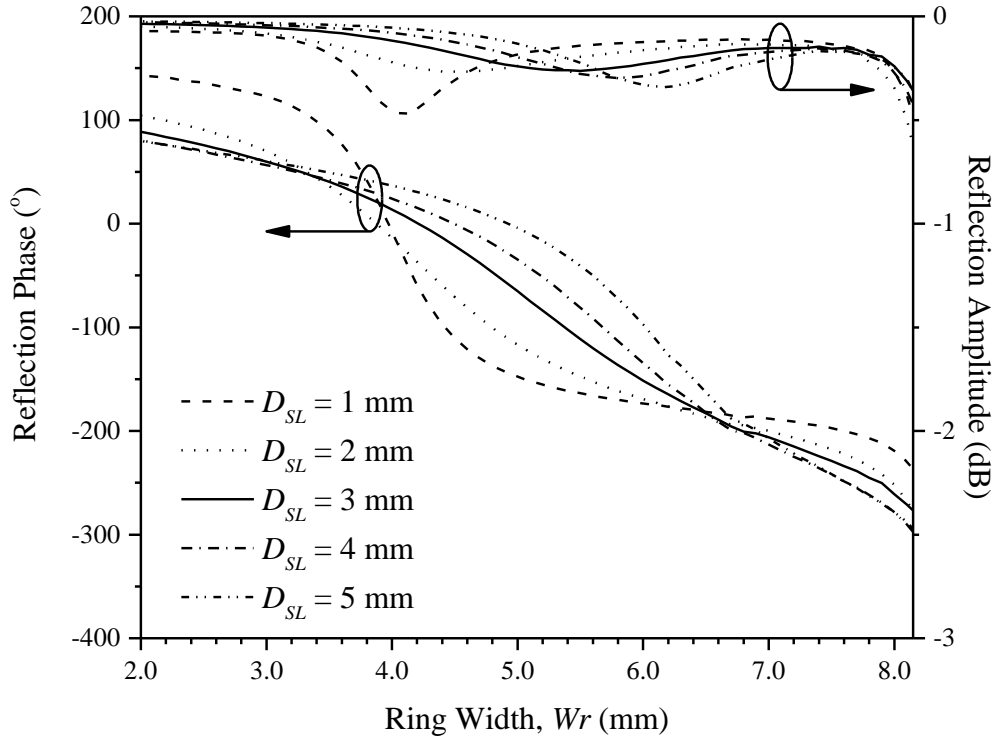


Figure 4.16: Effect of circular slot cavity diameter  $D_{SL}$  on the reflection amplitude and phase responses at the incident angles  $\theta_i = 20^{\circ}$  and  $f_o = 6.5$  GHz.

With the optimum selection of  $h = 20$  mm,  $L_g = 6$  mm, and  $D_{SL} = 3$  mm, the tapering rate  $R$  is varied, as shown in Figure 4.17. Reducing the tapering rate would improve the phase linearity as well as the reflection amplitude. However, the phase range is decreased. Further reducing the tapering rate causes the phase gradient and reflection amplitude to deteriorate at the larger end of  $W_r$ . Hence,  $R = 0.3$  is selected. Subsequently, the aperture opening  $H$  is varied as shown in Figure 4.18. It can be seen that the opening has the least effect among all the geometrical parameters. Hence,  $H = 8$  mm is selected because it provides the lowest reflection amplitude with a reasonably good phase gradient.

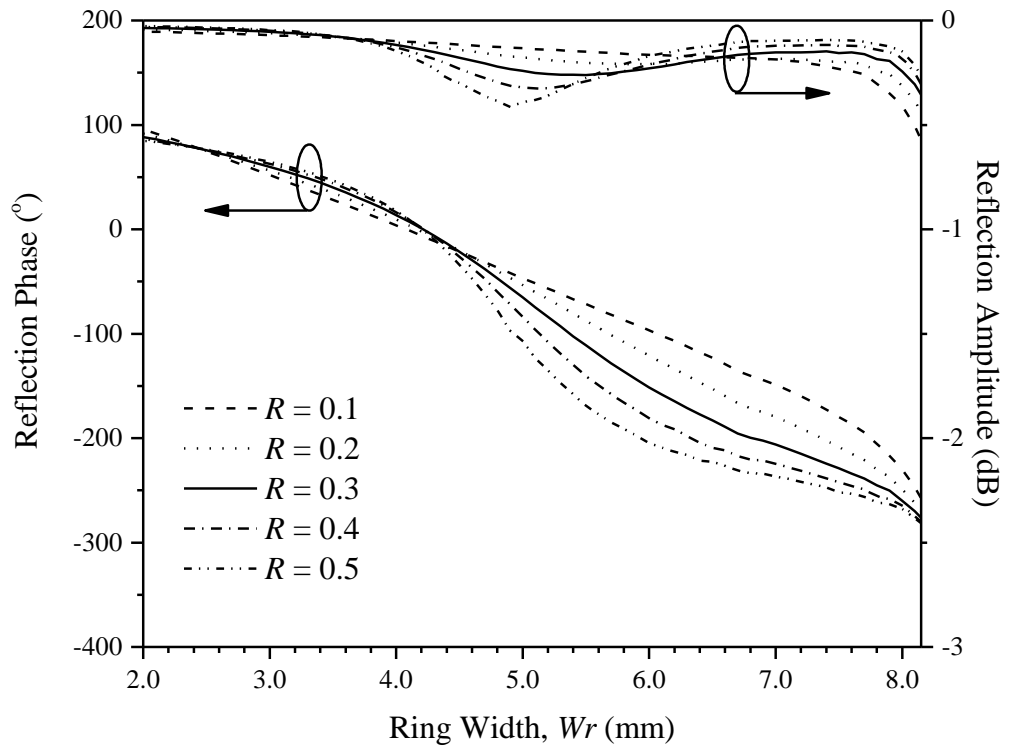


Figure 4.17: Effect of tapering rate  $R$  on the reflection amplitude and phase responses at the incident angles  $\theta_i = 20^\circ$  and  $f_o = 6.5$  GHz.

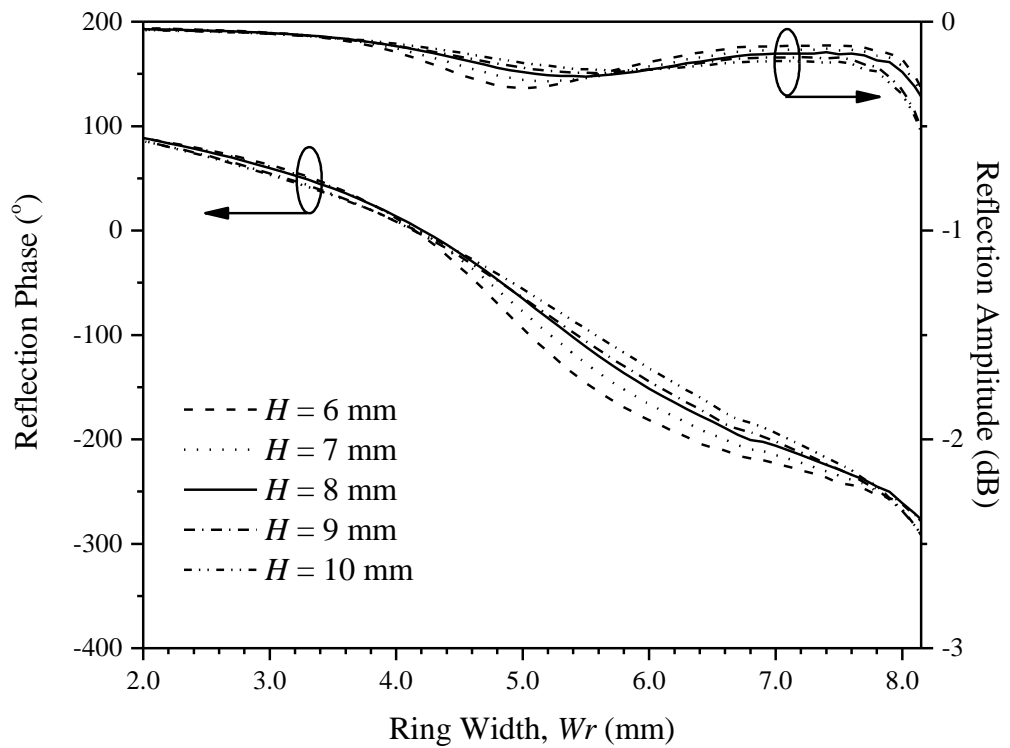


Figure 4.18: Effect of opening  $H$  on the reflection amplitude and phase responses at the incident angles  $\theta_i = 20^\circ$  and  $f_o = 6.5$  GHz.

Since the proposed unit element design placed the phase-shifting element upright and arranged in rows, the separation gap is made equal to the element spacing  $L$  ( $d_s = L$ ). The effect of reducing the separation gap is analysed as shown in Figure 4.19. The decreasing separation  $d_s$  from  $0.54\lambda_o$  does not provide advantages for the reflection phase curve and its amplitude.

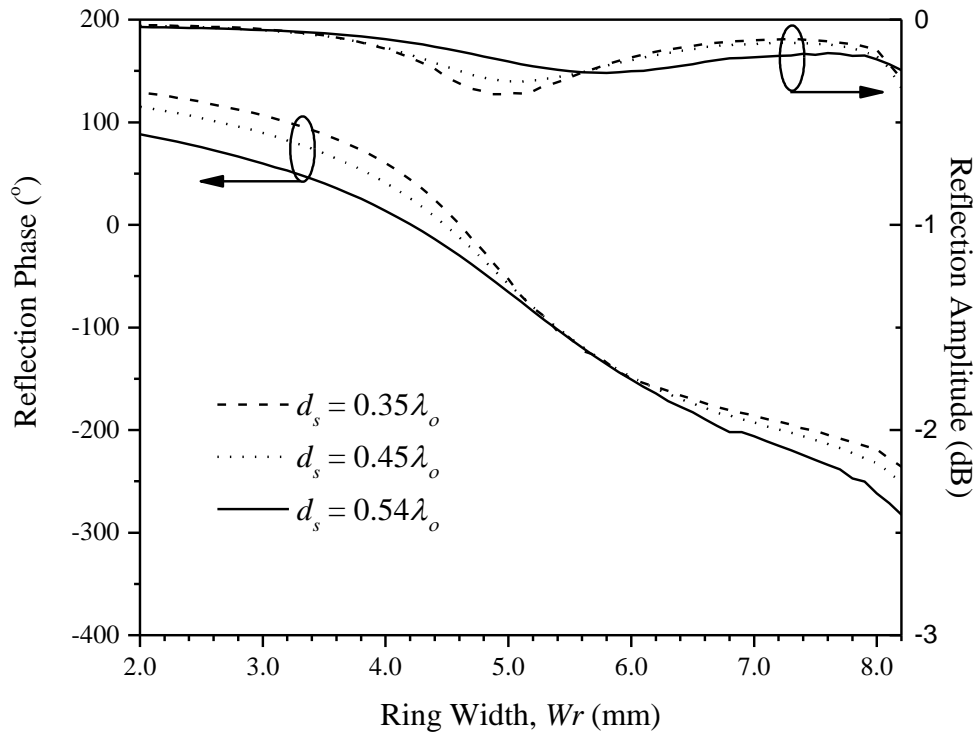


Figure 4.19: Effect of separation gap  $d_s$  on the reflection amplitude and phase responses at the incident angles  $\theta_i = 20^\circ$  and  $f_o = 6.5$  GHz.

From Figure 4.2, the proposed unit element is incident by a linearly y-polarized plane wave. The element has the tapered slot radiator on one side while the dumbbell-shaped square ring on the other. Therefore, the dependency of the wave incident angle on the reflection phase response is further analysed. Figure 4.20 shows the wave incident at  $\theta_{i,L}$  and  $\theta_{i,R}$  on the tapered slot radiator

and the dumbbell-shaped square ring, respectively. Meanwhile, Figure 4.21 shows the effects of the incident angles  $\theta_{i,R}$  in the  $xz$ -plane on the reflection amplitude and phase responses. Compared to Figure 4.4, where the wave incident angles are  $\theta_{i,L}$  in the  $xz$ -plane, the reflection amplitude and phase responses are almost similar and insensitive to the incident angles in the  $xz$ -plane.

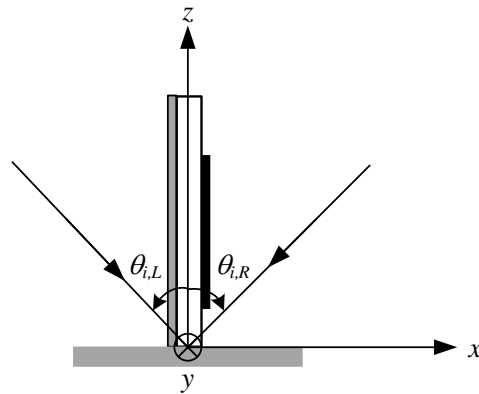


Figure 4.20: Wave incident angles  $\theta_{i,L}$  and  $\theta_{i,R}$  in  $xz$ -plane.

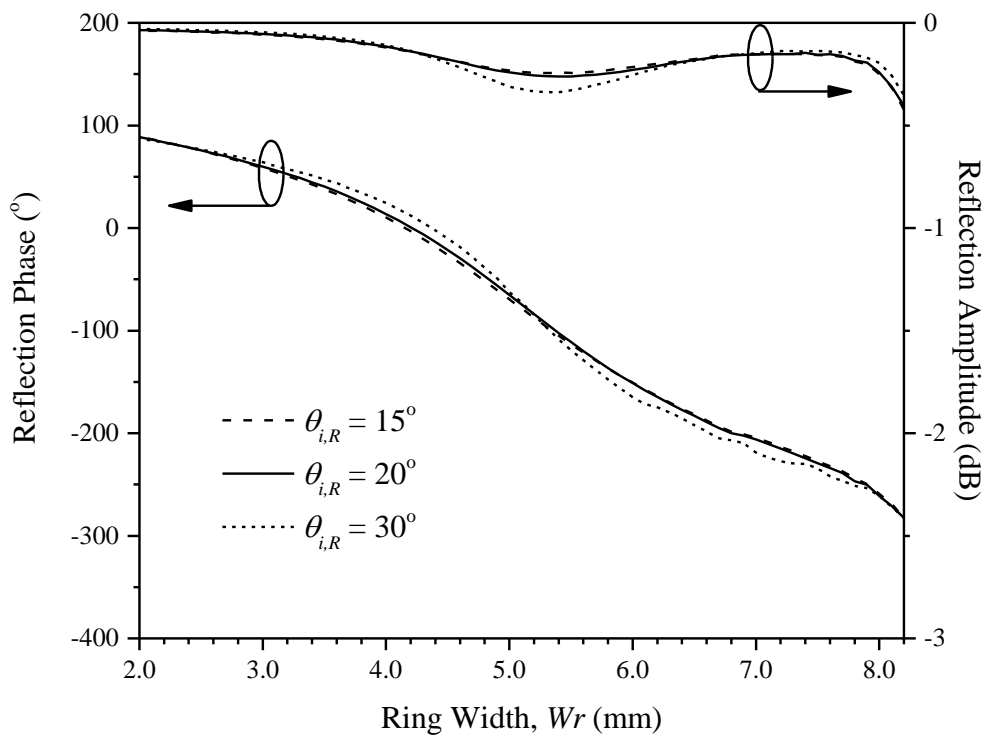


Figure 4.21: Effect of opposite wave incident angles  $\theta_{i,R}$  on the reflection amplitude and phase responses at  $f_o = 6.5$  GHz.

#### 4.5.2 Reflectarray Performance

The full-fledged reflectarray bandwidth performance is analysed to obtain an optimum operation bandwidth. Figure 4.22 shows the effect of the incident angle ( $\theta_i$ ) on the radiation gains. Smaller offset angles provide higher peak gain. It is observed that the feeding angle of  $\theta_i = 20^\circ$  gives the largest operational bandwidth (11.4%) as compared to its counterparts, 7.6% ( $\theta_i = 15^\circ$ ) and 5.3% ( $\theta_i = 30^\circ$ ). With reference to the radiation beam in the boresight direction in Figure 4.23, it is noticed that reasonably low side and back lobes are observed for  $\theta_i = 20^\circ$  for both the  $E$ - and  $H$ - planes radiation fields.

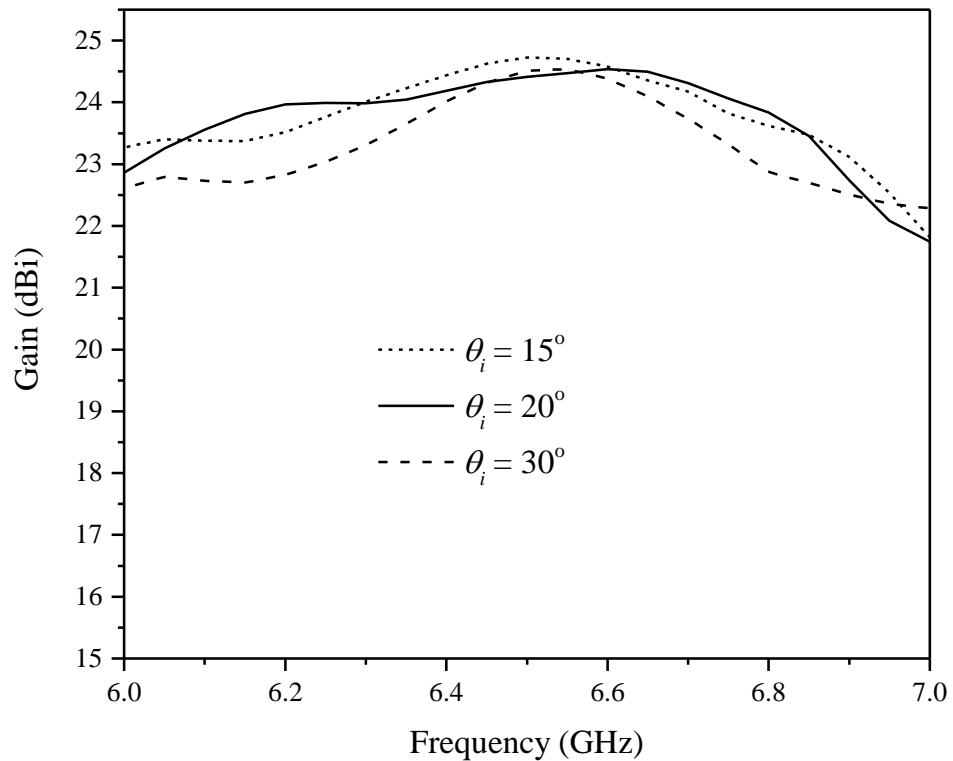
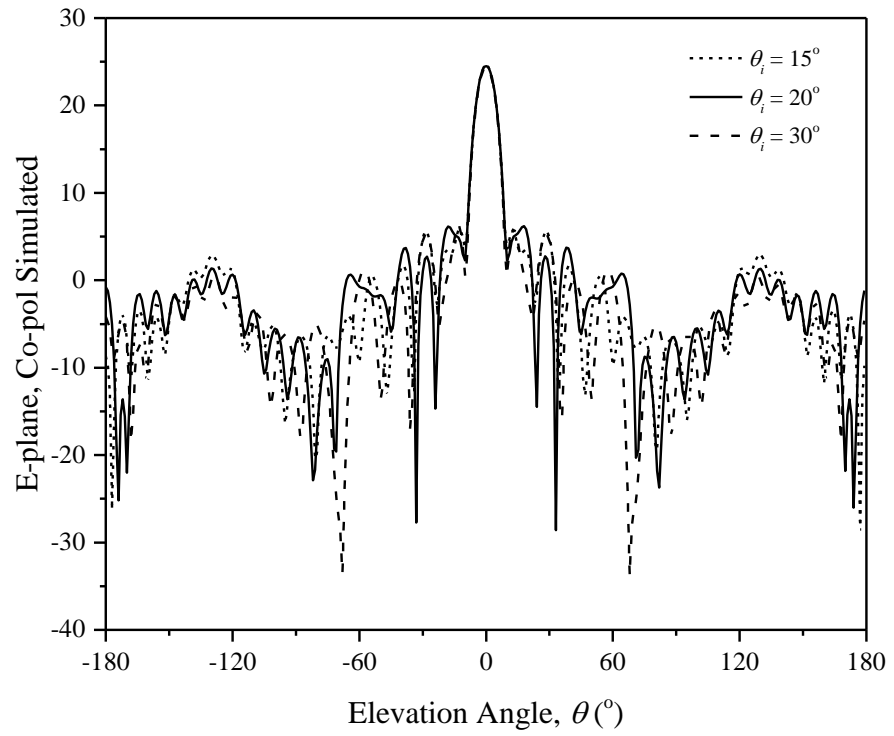
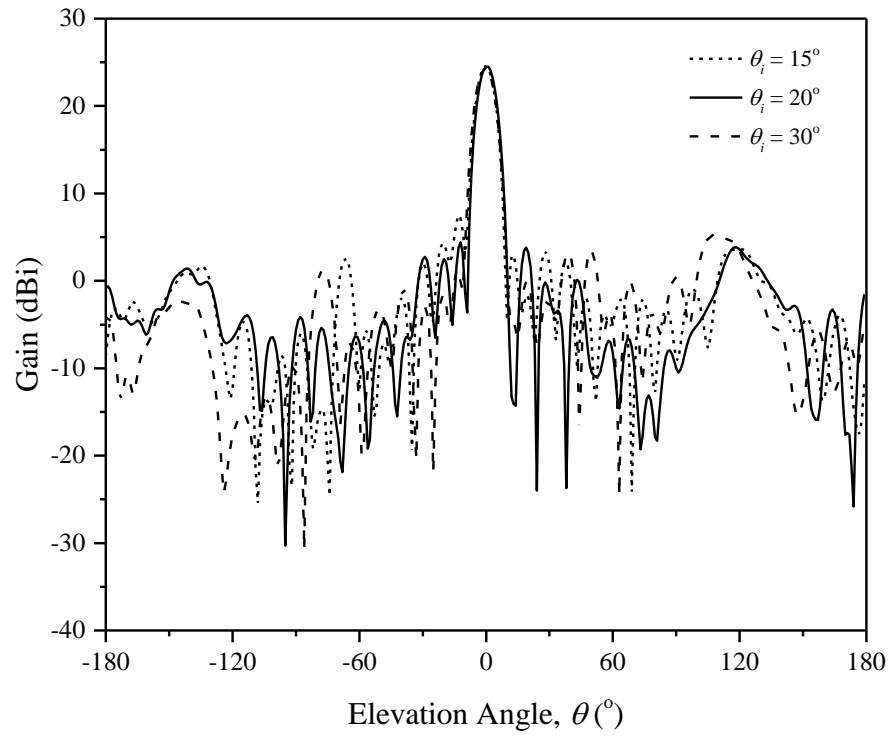


Figure 4.22: Simulated radiation gains of the proposed reflectarray for different feeding angles ( $\theta_i$ ).



(a)



(b)

Figure 4.23: Radiation patterns of the proposed reflectarray at 6.6 GHz for different feeding angles ( $\theta_i$ ). (a)  $E$ - and (b)  $H$ - planes.



The effect of the  $F/D$  is shown in Figure 4.24. Increasing the  $F/D$  cause the radiation gain to drop and affect the reflectarray overall performance. It is observed that the  $F/D = 0.65$  provides the largest operational bandwidth (11.4%) as compared to its counterparts, 10% ( $F/D = 0.85$  and  $1.0$ ). The reduction in antenna performance can be directly seen from the spillover issue that gives rise to the side and back lobes, as shown in both the  $E$ - and  $H$ - planes field radiation patterns in Figure 4.25. The low  $F/D$  agrees with the aperture efficiency analysis discussed in CHAPTER 2 Section 2.4.4. Due to the low cosine- $q$  factor of the feed, the optimum aperture efficiency is at lower  $F/D$ , as indicated in Figure 2.7.

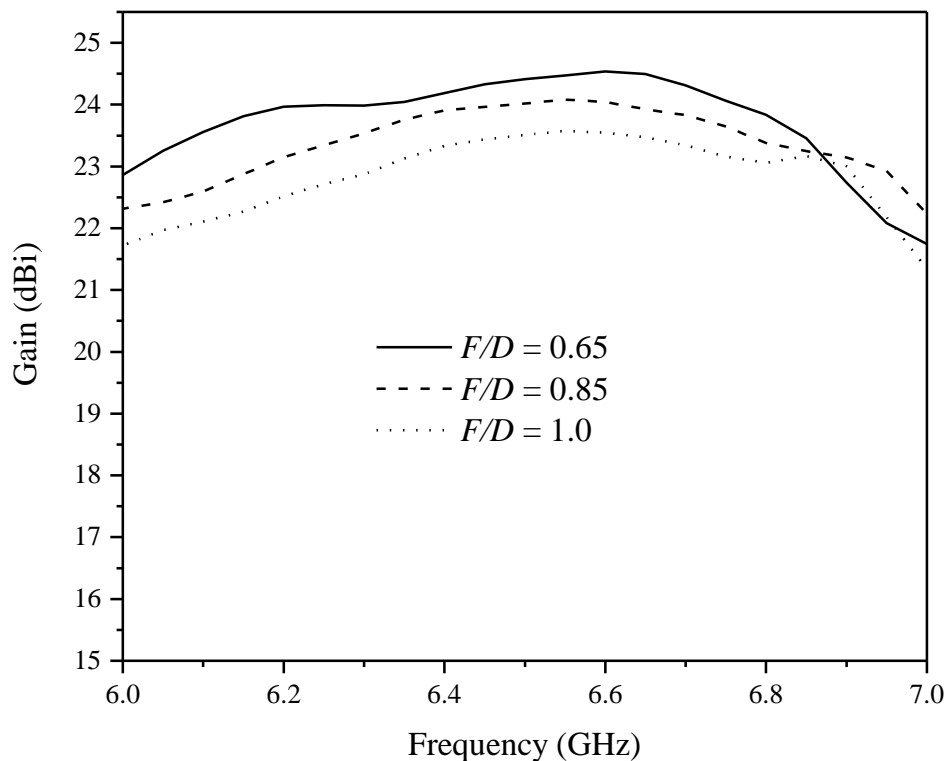
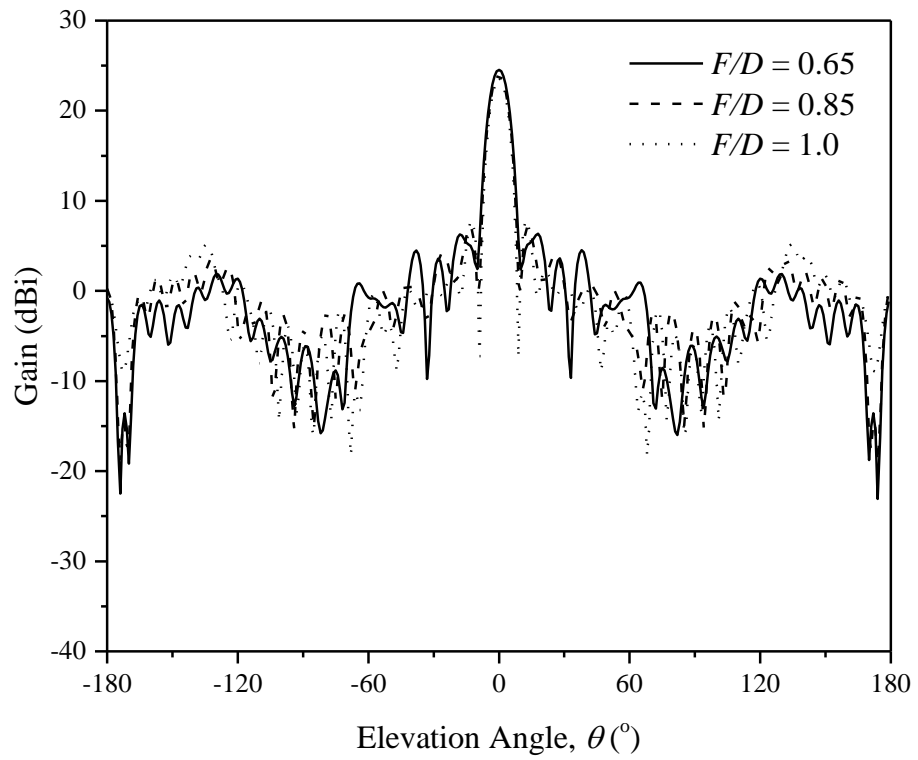
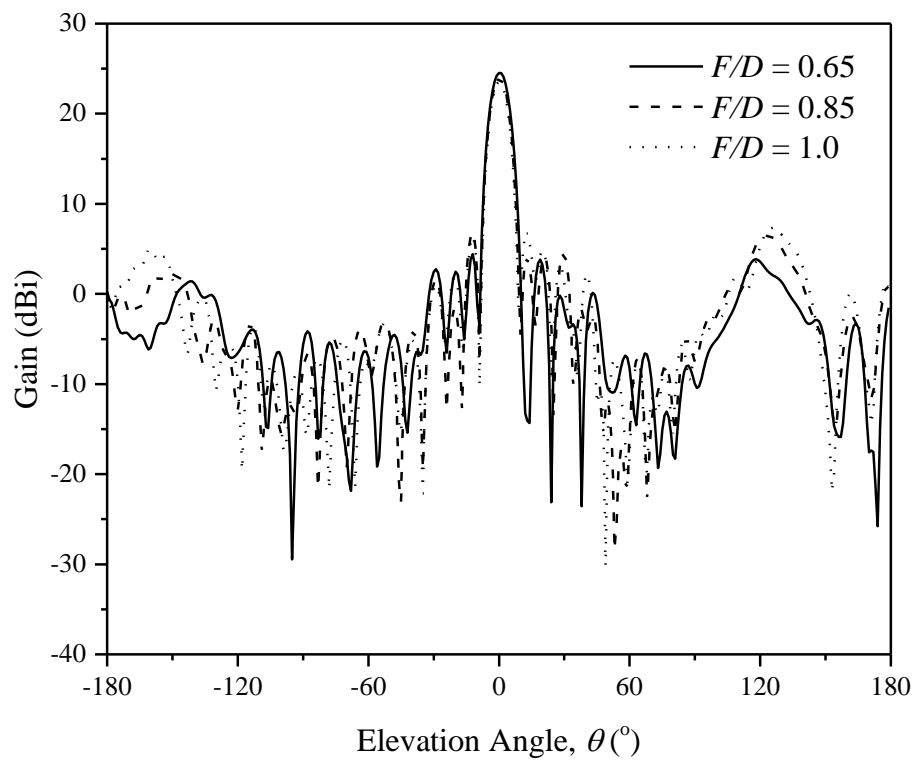


Figure 4.24: Simulated radiation gains of the proposed reflectarray for different feeding angles ( $\theta$ ).



(a)



(b)

Figure 4.25: Radiation patterns of the proposed reflectarray at 6.6 GHz for different feeding angles ( $\theta_i$ ). (a)  $E$ - and (b)  $H$ - planes.

## 4.6 Comparative Study

Table 4.2 compares the proposed reflectarray with other reported works covering C-band. In Tahseen's work (Tahseen and Kishk, 2017), a square ring-patch configuration of variable size is implemented using textile-based material. However, a limited phase range of  $340^\circ$  is obtained with a -1-dB gain bandwidth of 9.3%, and low aperture efficiency was reported. The work carried out by Lee (Lee et al., 2017) used a shorted E-shaped patch configuration to overcome the phase limitation in the conventional single-layer variable size patch configuration and achieve a phase range of  $\sim 360^\circ$ . Nevertheless, the performance is still below the proposed reflectarray. The configuration reported by Yang (Yang et al., 2018) employed a mechanically tunable height element structure using patch-slotted-patch. By adjusting the height separation between the patch and slotted-patch vertically, a phase range of  $324^\circ$  is obtained. The advantage of this design is that it allows beam-scanning capability of up to  $60^\circ$ . However, low -1-dB bandwidth was reported. Overall, the proposed reflectarray configuration has achieved the widest -1-dB bandwidth and low sidelobe levels.

Table 4.2: Comparison of the Proposed Reflectarray with Other Works.

Ref.	This Work	(Tahseen and Kishk, 2017)	(Lee et al., 2017)	(Yang et al., 2018)
Element Size [ $\lambda_o$ ]	0.54	0.55	0.658	0.386
Phase Range [ $^\circ$ ]	371	340	360	324
Aperture Size [mm]	325	426.7	275	528

-1-dB Gain BW [%]	10.6	9.3	8.1	6
-3-dB Gain BW [%]	19	22	19.8	-
AE [%]	40.4	20	36	48.6
Peak Gain [dBi]	24.1	22.3	23.7	25.7
Max. Cross-polarization [dB]	<-20	-21	-18	-26.9
Max. Sidelobe level [dB]	<-18	-16	-	-15.6
Frequency [GHz]	6.5	5.8	7.9	4.825

#### 4.7 Conclusion

A novel reflectarray element has been designed by combining the dumbbell-shaped microstrip ring resonator with the Vivaldi tapered slot antenna. Here, the ring size is varied to generate a phase range of  $371^\circ$ , with a phase sensitivity of  $64.6^\circ/\text{mm}$ . An antenna gain of 24.1 dBi has been obtained, achieving a wide -1-dB gain bandwidth of 10.6%. It has also achieved 40.4% aperture efficiency. Because of the use of the travelling-wave radiator, the proposed reflectarray element is able to achieve full phase range and low phase sensitivity at the same time. In addition, the antenna gain can be easily enhanced by elongating the profile length of the tapered slot antenna without the need to increase the number of elements. The abovementioned advantages are not possible with the conventional single-layer reflectarray elements.

## CHAPTER 5

### SINGLE-LAYER BROADBAND REFLECTARRAY USING CIRCULAR MICROSTRIP PATCH LOADED WITH TWO UNEQUAL SLOTS

#### 5.1 Introduction

As seen in the previous chapter, the reflectarray element was designed using a conventional variable-size square ring, which was closely coupled with a travelling-wave radiator as a phase-shifting element for achieving a full phase range of  $360^\circ$  and low phase sensitivity simultaneously. However, the proposed reflectarray was only able to achieve a moderate profile. This chapter proposes a unique design utilising a single-layer circular patch loaded with a pair of unequal slots for designing a broadband reflectarray. The aim is to enhance the phase tuning ability and provide a low-profile reflectarray. Here, the linearity and sensitivity of the phase curve can be easily optimised by using a simple design equation that pegs the two unequal slots to the patch radius. The optimised reflectarray element is able to achieve a broad phase range and low phase sensitivity simultaneously. Broad bandwidth and aperture efficiency are achievable when the element is translated into a full-fledged reflectarray. The proposed reflectarray design is simpler than some of the reported works in the literature (Hasani et al., 2010; Liu et al., 2017; Sayidmarie and Bialkowski, 2011).

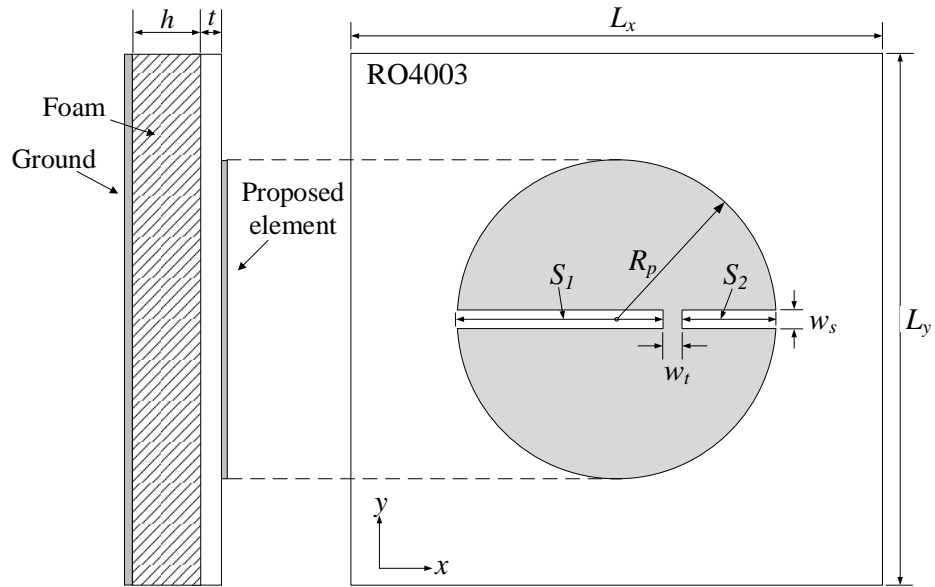
## 5.2 Reflectarray Unit Element

Figure 5.1 (a) shows the configuration of the unit element, which is made on a single piece of RO4003C substrate ( $t = 0.8128$  mm,  $\epsilon_{r1} = 3.38$ , and  $\tan\delta = 0.0027$ ) and suspended from the ground plane by an air layer ( $h = 5.7$  mm). The cell size of the unit element, which will be translated into the spacing of the elements in the reflectarray later, is set to be  $L_x = L_y = 16$  mm ( $0.48\lambda_o$  at  $f_o = 9.0$  GHz) to avoid the generation of grating lobes. With reference to Figure 5.1 (b), the unit element is placed at one end of the Floquet cell while a linearly  $y$ -polarized plane wave is launched from the wave port (Port 1), propagating in the  $xz$ -plane with an incident angle of  $\theta_i = 20^\circ$ . The unit element is located at a distance of 80 mm from the wave port. In the simulation, the reference plane is de-embedded from the wave port to the top surface of the radiating aperture. As can be seen from Figure 5.1 (a), the element configuration consists of a circular patch with radius  $R_p$ , which is horizontally loaded with two rectangular slots of unequal length. A narrow shunt strip separates the two slots with a width of  $w_t$  and a height of  $w_s$ . Here, the patch radius ( $R_p$ ) is employed as the phase-shifting geometrical parameter, with  $R_p$  varying from 2 mm to 6 mm. The slots are varied simultaneously following the relationship:

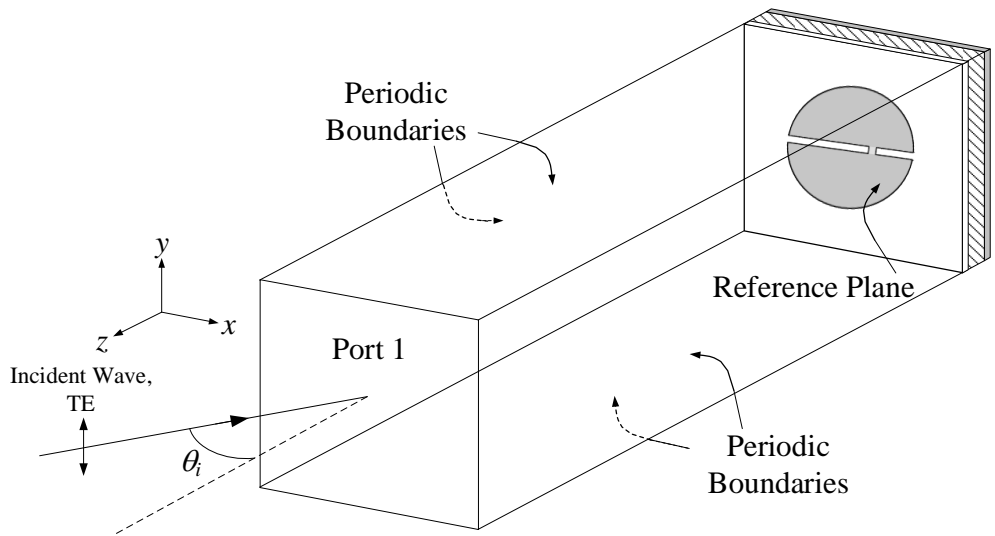
$$\left. \begin{aligned} S_1 &= R_p (1 - \xi) \\ S_2 &= R_p (1 + \xi) - w_t \end{aligned} \right\} \quad (5.1)$$

where  $-0.6 < \xi < 0.7$  is a real number and is defined as the slot-length ratio, which can be used to optimise the reflection phase response. Negative  $\xi$  makes

$S_1 > S_2$ . Here, the optimum ratio is chosen to be  $\xi = -0.2$  to provide a broad and linear phase curve. In this design, the optimum shunt strip is found to be  $w_s = w_t = 0.5$  mm. **Error! Reference source not found.** Table 5.1 summarises the design parameters, and their parametric analysis can be found in Section 5.5.1.



(a)



(b)

Figure 5.1: (a) The proposed unit element. (b) Simulation model of the unit element in a Floquet cell.

Table 5.1: Design Parameters.

Parameter	Values	Parameter	Values
$t$	0.813 mm	$h$	5.7 mm
$w_t$	0.5 mm	$L_x$	16 mm
$w_s$	0.5 mm	$L_y$	16 mm
$\xi$	-0.2	$R_p$	2.0 – 6.0 mm

Figure 5.2 shows the effects of  $\xi$  on the reflection phase for different frequencies at a wave incident angle of  $20^\circ$  at 9 GHz. It is observed that the phase range and curve gradient can be easily controlled by adjusting  $\xi$ . A smoother gradient has been found to be more beneficial for optimising the bandwidth performances of the reflectarray (Xia et al., 2017). With reference to the reflection amplitudes at an incident angle of  $\theta_i = 20^\circ$  with different frequencies in Figure 5.3 (a), the losses are found to be lesser than 1dB with smooth phase gradients in general. A reflection phase range of  $458^\circ$ , with a phase sensitivity of  $134^\circ/\text{mm}$ , is achievable at the design frequency of  $f_o = 9.0$  GHz. The phase sensitivity would be further reduced by half if the patch diameter were made as to the phase-shifting parameter. Figure 5.3 (b) shows the effects of the incident angle ( $\theta$ ) on wave reflection. For all cases, the phase curves are found to be linear and insensitive to the wave incident angle, which is most desirable.



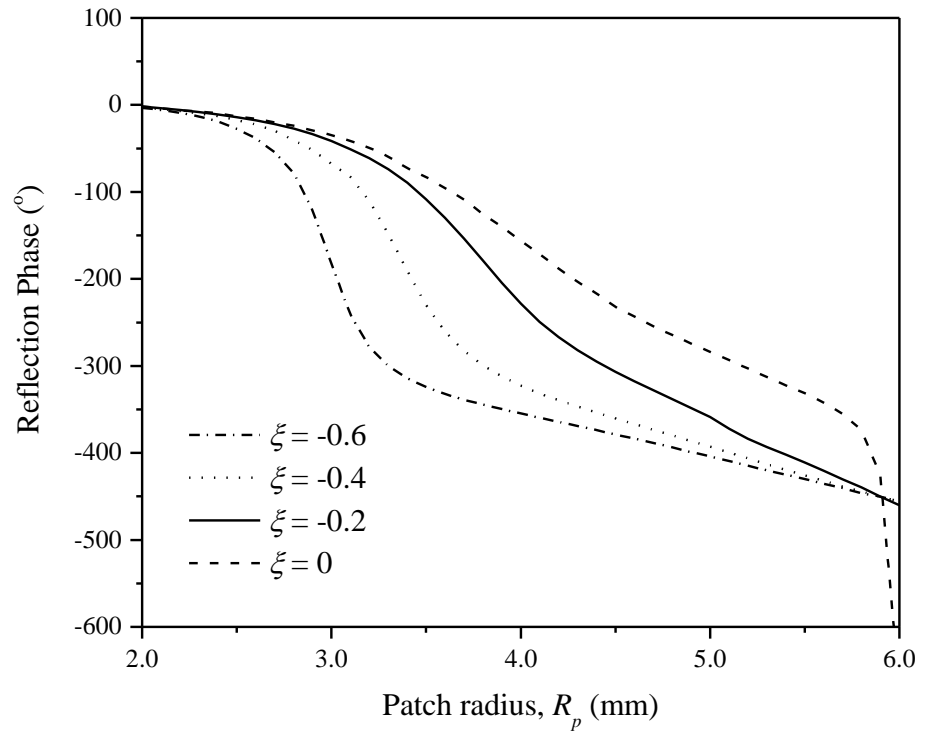
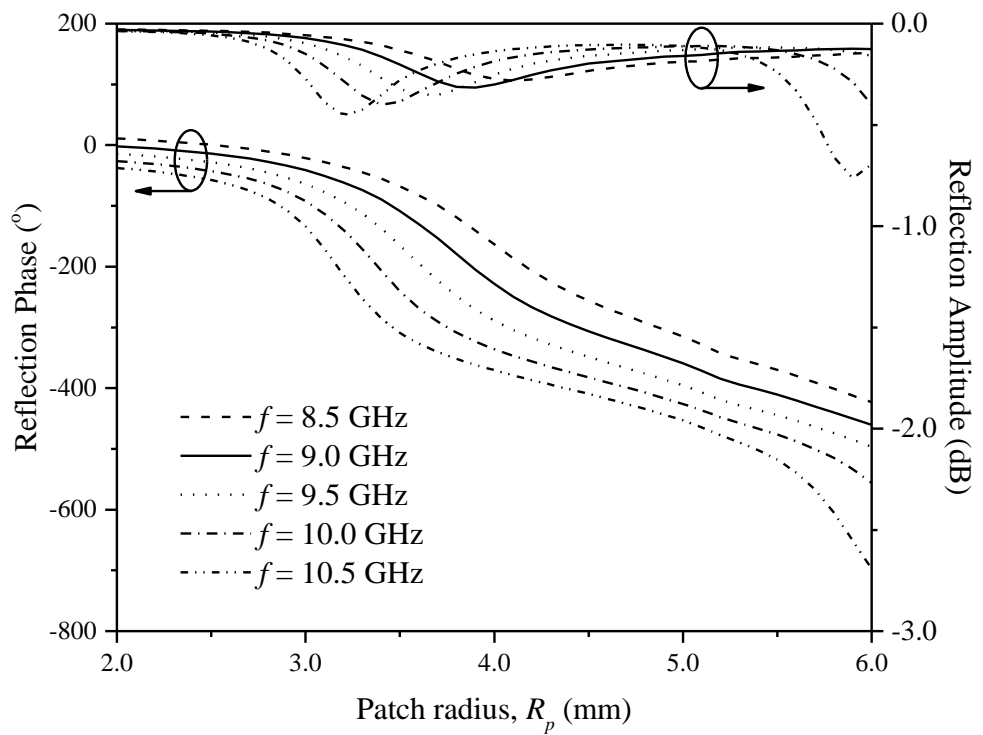
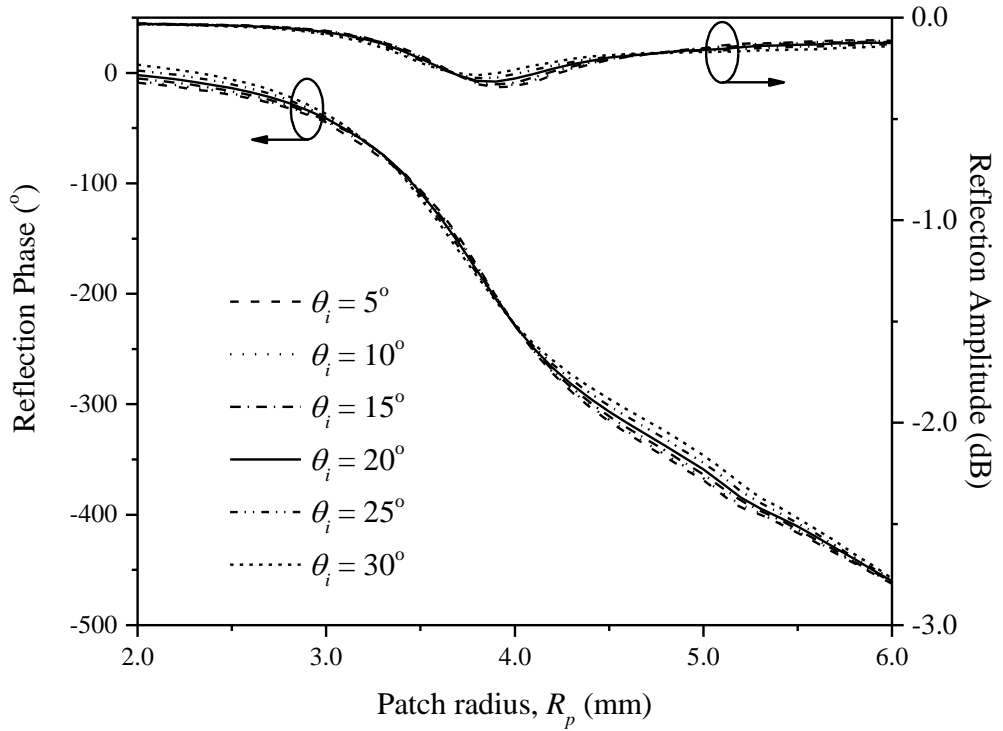


Figure 5.2: Reflection phase response of the proposed unit element at  $f_o = 9.0$  GHz for different slot length ratios  $\xi$  at  $\theta_i = 20^\circ$ .



(a)



(b)

Figure 5.3: Reflection amplitude and phase responses of the proposed unit element as a function of patch radius  $R_p$ . (a) Different wave frequencies at  $\theta_i = 20^\circ$ . (b) Different incident angles  $\theta_i$  at  $f_o = 9.0$  GHz.

The reflectarray element is designed using a conventional circular microstrip resonator (Figure 5.4 (a)) with  $w_t = 8.0$  mm,  $S_1 = 0.0$  mm,  $S_2 = 0.0$  mm resonating in its fundamental  $TM_{11}^z$  mode (Eriksson et al., 2001), where the resonant frequency of a circular microstrip patch (Wolff and Knoppik, 1974) can be estimated using the following equation:

$$f_{mn} = \frac{cK_{mn}}{L_e \sqrt{\epsilon_e}} \quad (5.2)$$

where  $c$  is the speed of light,  $K_{mn}$  is the  $m^{\text{th}}$  root of the derivative of the Bessel function of order  $n$ . It has a substrate ( $\epsilon_{r1}$ ,  $t$ ) and air spacer ( $\epsilon_{r2}$ ,  $h$ ). This two-

layer structure can be viewed as an equivalent single-layer structure having an effective dielectric constant (Nasimuddin et al., 2005) and is expressed as:

$$\varepsilon_e = \frac{\varepsilon_{r1}\varepsilon_{r2}(h+t)}{\varepsilon_{r1}h + \varepsilon_{r2}t} \quad (5.3)$$

For this composite structure, the effective radius  $L_e$  can be estimated (Sakotic et al., 2017) as:

$$L_e \approx \left[ 2\pi R_p + (4R_p - 2w_t) \right] \left\{ 1 + \frac{2d_e}{\pi R_p \varepsilon_e} \left[ \ln \left( \frac{\pi R_p}{2d_e} \right) + 1.7726 \right] \right\}^{1/2} \quad (5.4)$$

where  $(4R_p - 2w_t)$  is the total slot length of the reflectarray element and  $d_e = t + h$ . For a particular case, where  $w_t = 0.5$  mm or  $R_p = 4$  mm, the resonant frequency is calculated to be 8.1 GHz. When a single rectangular slot is etched on the left edge, as shown in Figure 5.4 (b), the current path becomes slightly longer, introducing additional inductance to the element. When another slot is included on the right edge, as shown in Figures 5.4 (c) and (d), the current intensities on the patch become higher, especially along the slot edges, giving an even higher inductance. It shows that the two slots can be effectively used as geometrical parameters for changing the reflection phase.

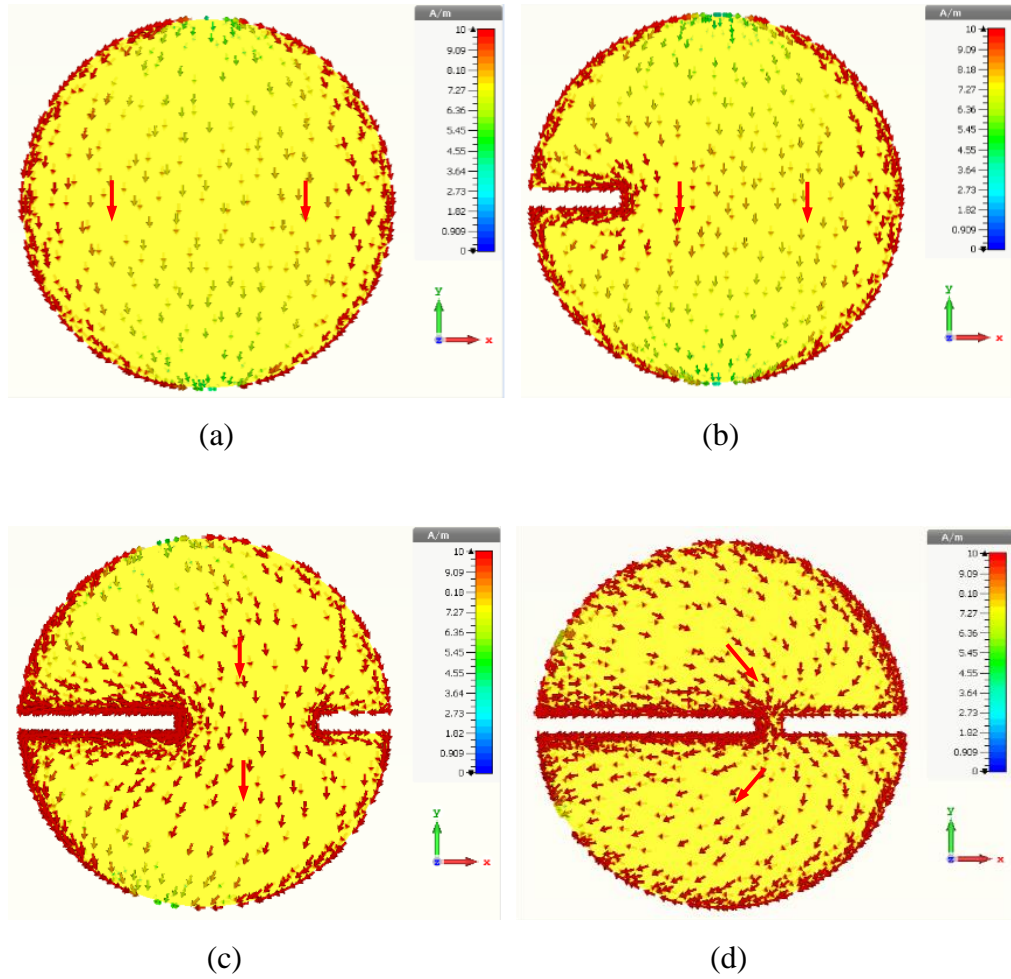
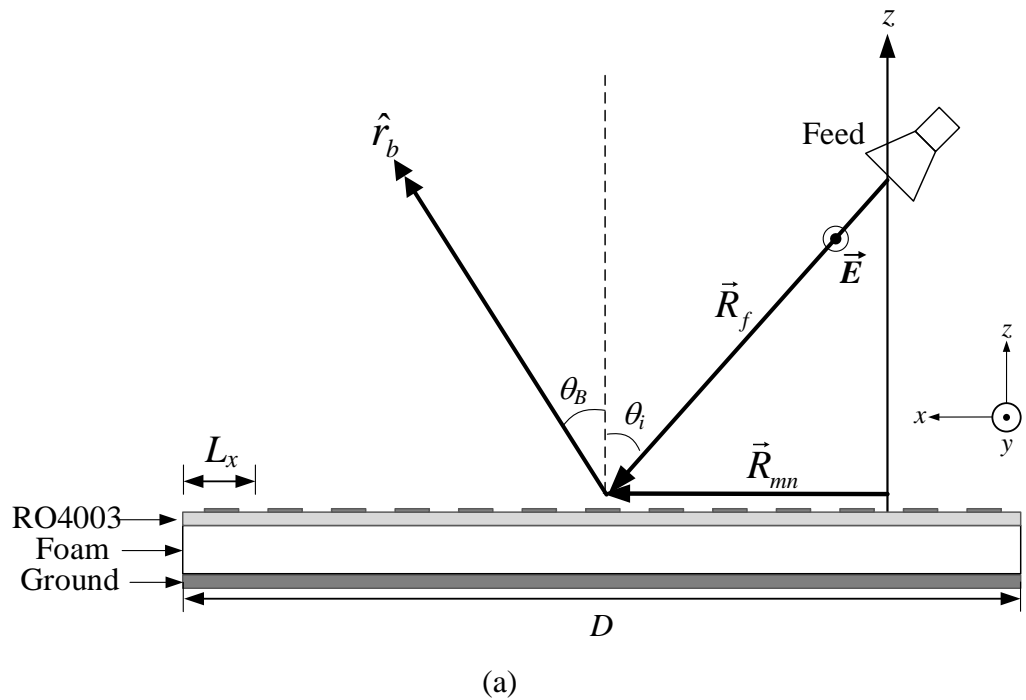
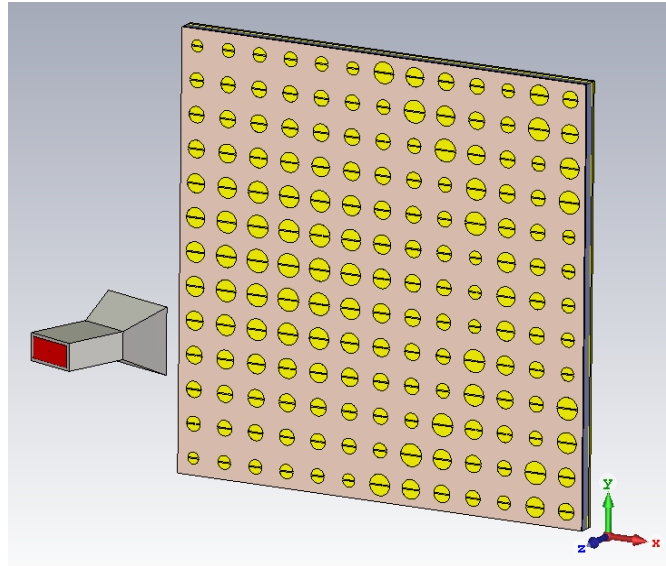


Figure 5.4: Current distributions for the cases of (a)  $w_t = 8.0$  mm,  $S_1 = 0.0$  mm,  $S_2 = 0.0$  mm; (b)  $w_t = 6.0$  mm,  $S_1 = 2.0$  mm,  $S_2 = 0.0$  mm; (c)  $w_t = 3.0$  mm,  $S_1 = 3.4$  mm,  $S_2 = 1.6$  mm; (d)  $w_t = 0.5$  mm,  $S_1 = 4.8$  mm,  $S_2 = 2.7$  mm.

### 5.3 Reflectarray Design Configuration

The design of a  $13 \times 13$  reflectarray, which composes 169-unit elements, is shown in Figure 5.5. Figure 5.5 (a) shows the side view of the proposed reflectarray antenna with the simulation model shown in Figure 5.5 (b). The reflectarray aperture is square in shape and has a total dimension  $D = 13L_x = 208$  mm. The substrate is stacked on a piece of polystyrene foam with a dielectric constant of  $\epsilon_r \sim 1$  and a thickness of  $h = 5.7$  mm, with a copper plate placed underneath as ground. The feeding horn is suspended at a farfield distance  $F = 150$  mm at an incident angle of  $\theta_i = 20^\circ$  from the centre point, yielding an  $F/D$  ratio of 0.72. An offset feed method is used to reduce the feed blockage and avoid the grating lobes generation.





(b)

Figure 5.5: (a) Side view of the proposed reflectarray with a feeding horn suspended at  $\theta$ . (b) Simulation model of the reflectarray in CST Microwave Studio<sup>®</sup>.

A linearly polarized X-band pyramidal horn antenna (8.2 GHz – 12.5 GHz) is used as a feeding horn. The horn flare has a dimension of 36.5 mm ( $H$ )  $\times$  28.5 mm ( $E$ ), with a flare length  $F_L = 20$  mm, and is attached to a waveguide adaptor (Vector Telecom VT100WCASKPC) as shown in Figure 5.6. Figure 5.7 shows the simulated 3D farfield radiation pattern of the feed horn. The simulated antenna gain has a nominal value of 10.1 dBi and a 3-dB beamwidth of  $56.5^\circ$  in both the  $E$ - and  $H$ - planes at 9.0 GHz, as shown in Figure 5.8. The inset in Figure 5.8 shows the cosine- $q$  model radiation pattern plot. The 2D radiation pattern matches the cosine- $q$  model pattern up to about  $\pm 30^\circ$  with the value of  $2q_f = 5.4$ . The phase centre of the horn is 2.35 mm below the opening aperture throughout this angular range.

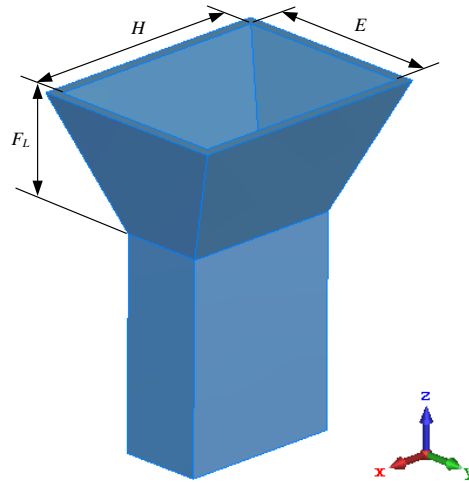


Figure 5.6: Simulation model of X-band pyramidal horn antenna.

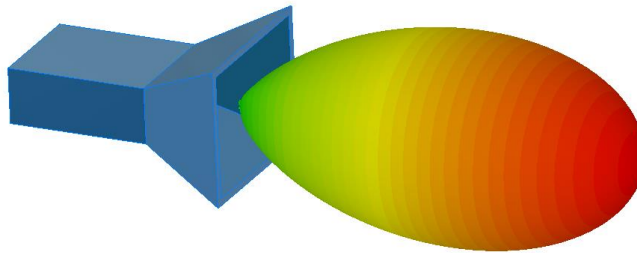


Figure 5.7: A 3D farfield plot of the pyramidal horn antenna.

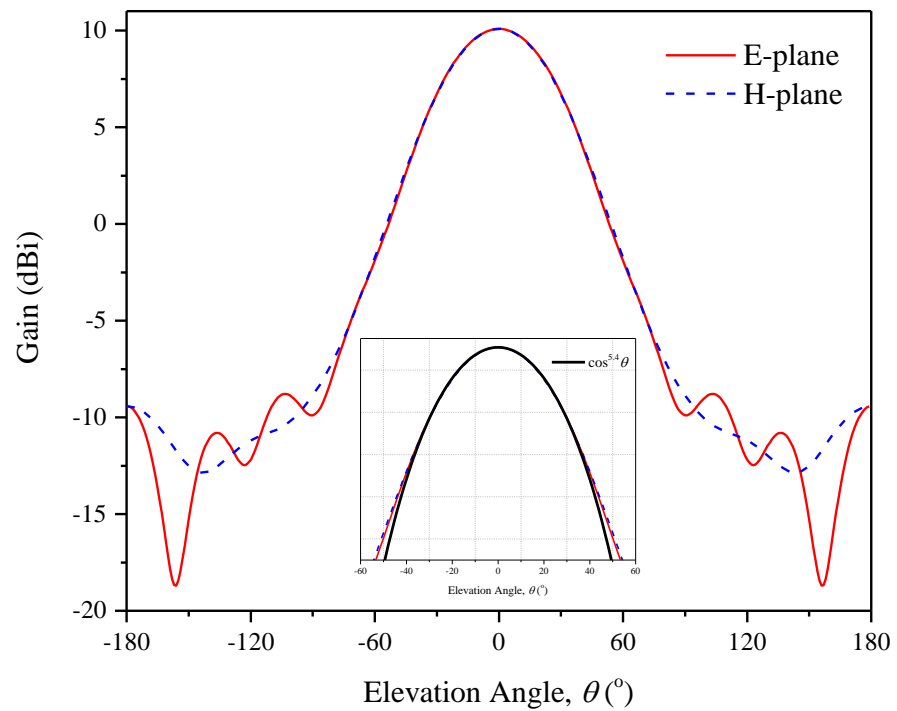


Figure 5.8: Radiation patterns of the X-band pyramidal horn antenna: 2D and cosine- $q$  model.

The full-fledged linearly polarized reflectarray is designed to radiate in the broadside direction ( $\theta_B = 0^\circ$ , Figure 5.5 (a)). The desired phase shift for each element can be calculated using Equation (2.26). In the same way, the corresponding geometrical dimensions for all elements on the reflectarray aperture can then be extracted from the reflection phase curve ( $\xi = -0.2$ ), which is shown in Figure 5.2. Figure 5.9 (a) shows the phase distributions of all the elements used to synthesise the proposed reflectarray. The construction and simulation of the full 3D model (Figure 5.5 (b)) are then carried out using CST Microwave Studio<sup>®</sup>.

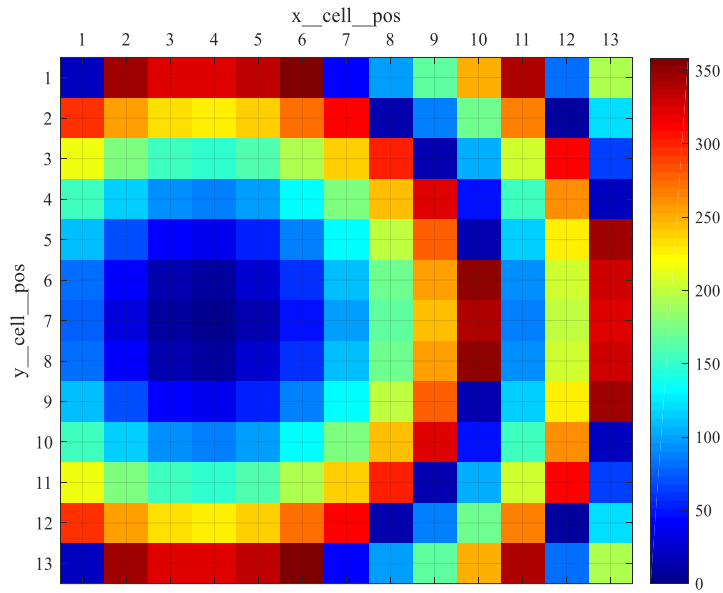
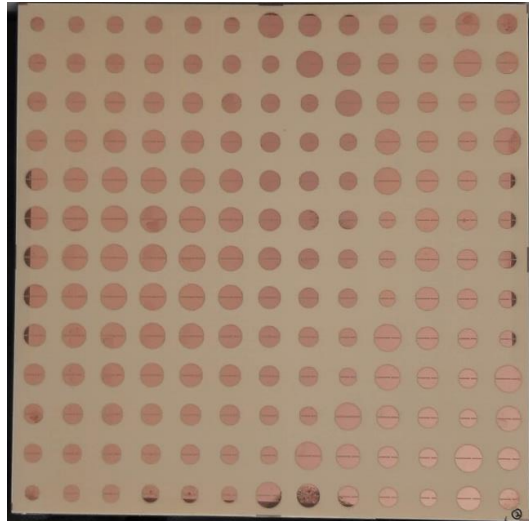


Figure 5.9: (a) Phase distributions on the proposed reflectarray.

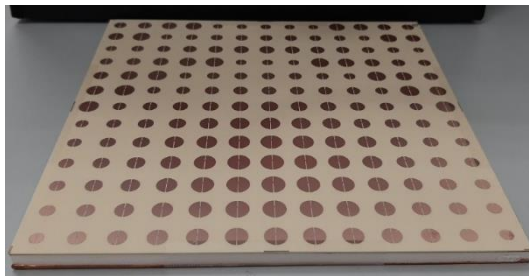
A prototype is fabricated, as shown in Figure 5.10. The arrays are fabricated on a piece of RO4003 and stacked on a polystyrene foam with a copper plate placed underneath as ground. The foam has a thickness of  $h = 5.7$



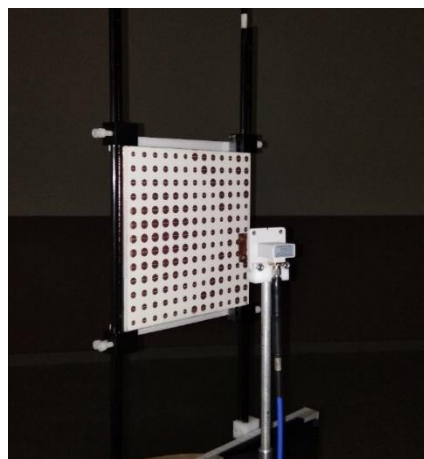
mm with a dielectric constant of  $\epsilon_r \sim 1$ . The side view of the prototype attached to the rotating table is shown in Figure 5.10.



(a)



(b)



(c)

Figure 5.10: Prototype of the proposed reflectarray viewed from different directions. (a) Front view, (b) Side view, and (c) side view of the prototype attached to the rotating table.

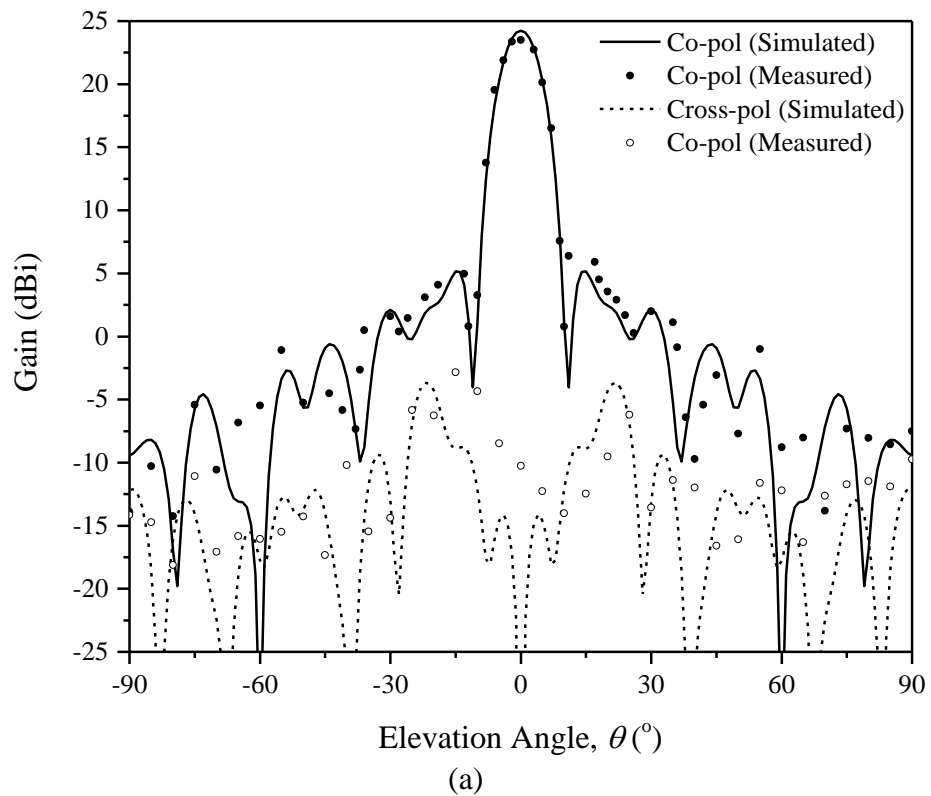
Then, the fabricated prototype is measured using the measurement setup described in Section 3.4. A linearly polarized X-band pyramidal horn (XB-HA90-18-SMA, 8.2 GHz – 12.9 GHz) located at farfield is used as a receiving horn. It is connected to a spectrum analyser (Advantest U3771) for recording purposes. The farfield distance is  $R = 6.5$  m. The reflectarray is directed facing  $+z$  and rotated in the azimuth direction to enable the measurement of radiation patterns at all angles.

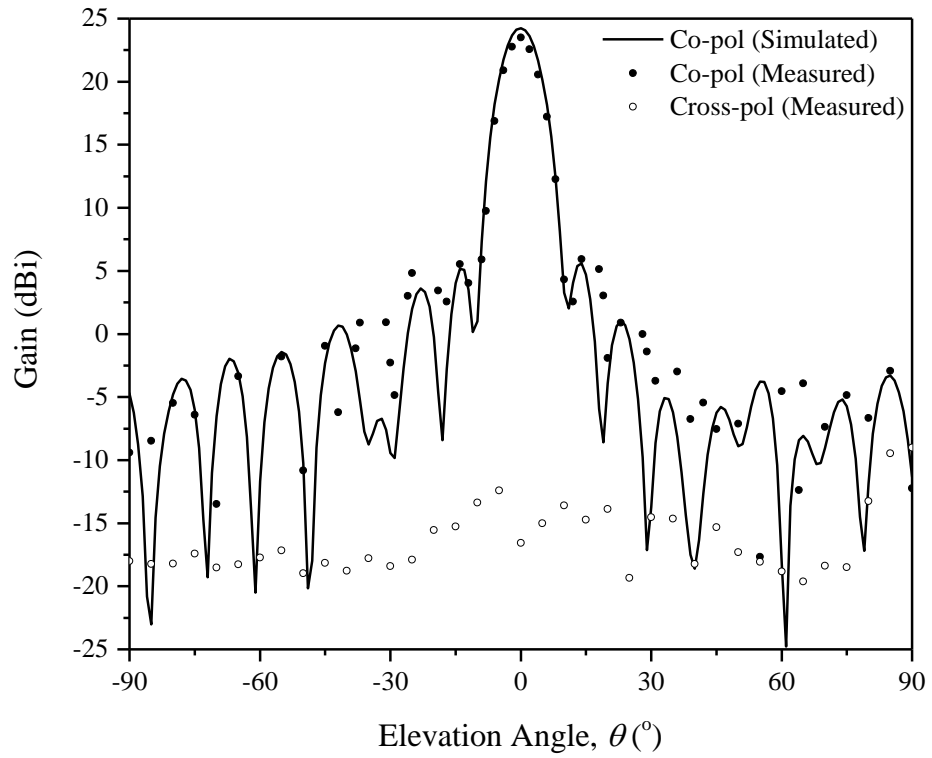
#### 5.4 Results and Discussion

Figure 5.11 shows the measured and simulated radiation patterns in the  $E$  ( $yz$ -plane) and  $H$  ( $xz$ -plane) planes at 9.3 GHz. Good agreement is observed between the simulation and measurement, with the sidelobe level lower than that in the boresight direction ( $\theta = 0^\circ$ ) by at least 20 dB. Also, the cross-polarized radiation field is found to be more than 25 dB lower than the co-polarized one in the boresight. The  $H$ -plane simulated cross-polarized fields are not shown in Figure 5.11(b), as all the data points are well below -80 dB.

Figure 5.12 shows the measured and simulated antenna gains in the boresight direction, where reasonable agreement has been observed. The measured and simulated maximum antenna gains read 23.4 dBi and 24.2 dBi, respectively, at 9.3 GHz. The optimum aperture efficiency is measured to be 42% (simulation: 50.3%). The simulated radiation efficiency is found to be 98%. As shown in Figure 5.12, the proposed reflectarray has a measured -1-dB gain

bandwidth of 11.8% covering 8.85 GHz – 9.95 GHz (simulation: 14.5% covering 8.85 GHz – 10.2 GHz). The discrepancy in the measured and simulated aperture efficiencies can be due to random phase errors caused by fabrication tolerances (Sayidmarie and Bialkowski, 2011) and misalignments, which are unavoidable during the measurement processes. The proposed reflectarray is simple in structure as it is composed of a simple circular patch resonator. However, the limitation of this structure is that it may be very challenging to expand the bandwidth further using a single circular patch resonator.





(b)

Figure 5.11: Measured and simulated (a) *E*- and (b) *H*- plane radiation patterns of the proposed reflectarray at 9.3 GHz.

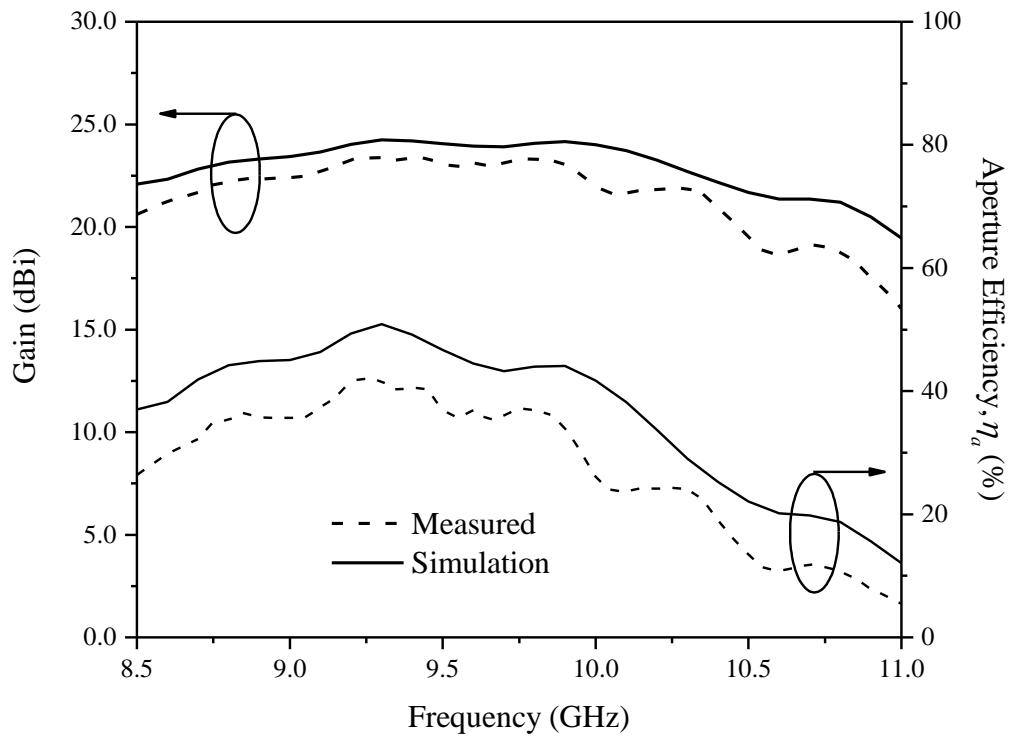


Figure 5.12: Measured and simulated antenna gains of the proposed reflectarray as a function of frequency.

## 5.5 Parametric Analysis

Parametric analysis is performed to study the characteristics of the proposed unit element and reflectarray to achieve optimum performance. Details of their analysis will be discussed in the following Section 5.5.1 and Section 5.5.2, respectively.

### 5.5.1 Unit Element Reflection Phase

Simulations have been conducted to study the effects of crucial design parameters on the reflection characteristics of the unit element at design frequency  $f_o = 9.0$  GHz. Figure 5.13 shows reflection phase responses when varying the slot-length ratio ( $\xi$ ). It can be seen that the linearity of the phase gradient can be easily tuned by varying  $\xi$ , although the phase range is not affected much. Here, the reflection loss is generally less than 1 dB in the passband. The slot-length ratio can be varied from -0.6 to 0.7 based on the  $S_1$  and  $S_2$  relationships. It moves the shunt strip from the leftmost ( $S_1 > S_2$ ) to the rightmost ( $S_1 < S_2$ ) of the circular patch. As can be seen in Figure 5.13, the phase sensitivity becomes lower, and linearity becomes better with increasing  $\xi$ . In this design, the optimum slot-length ratio is chosen as  $\xi = -0.2$ , which is equivalent to  $S_1 = 7.195$  mm and  $S_2 = 4.295$  mm at  $R_p = 4.0$  mm. A smooth phase curve with a phase sensitivity of  $134^\circ/\text{mm}$  and a reflection loss of less than 0.5 dB can be obtained simultaneously.

Figure 5.14 shows the effects of the slot width ( $w_s$ ) and strip width ( $w_t$ ) on the reflection characteristics. It can be seen that the phase gradient is more sensitive to the slot width changes than the strip width. With reference to Figure 5.14 (a), it is observed that a wider slot gives a better phase gradient but with the expense of decreasing in phase range slightly. For all cases, the phase ranges can still be kept well above  $400^\circ$ . From Figure 5.14 (b), changing the strip width shows the opposite trend, and increasing the strip width improves the phase gradient without altering the phase range. For both cases, a steeper phase gradient comes with higher reflection loss. In order to achieve low phase sensitivity and low reflection loss simultaneously, both the slot and strip widths are fixed at  $w_s = w_t = 0.5$  mm in this design.

Figure 5.15 shows the effects of the air spacer on the reflection phase. The maximum phase range obtained is  $472^\circ$  at  $h = 3.157$  mm, although the gradient is steep near the resonance. Further increasing spacer thickness causes the phase range to reduce. Also, the phase linearity worsens, and the reflection loss increases when  $h = 6.35$  mm and beyond. In this design, the optimum thickness is fixed at 5.7 mm as it provides a linear phase curve with the lowest phase sensitivity and a broad phase range of  $458^\circ$  simultaneously.

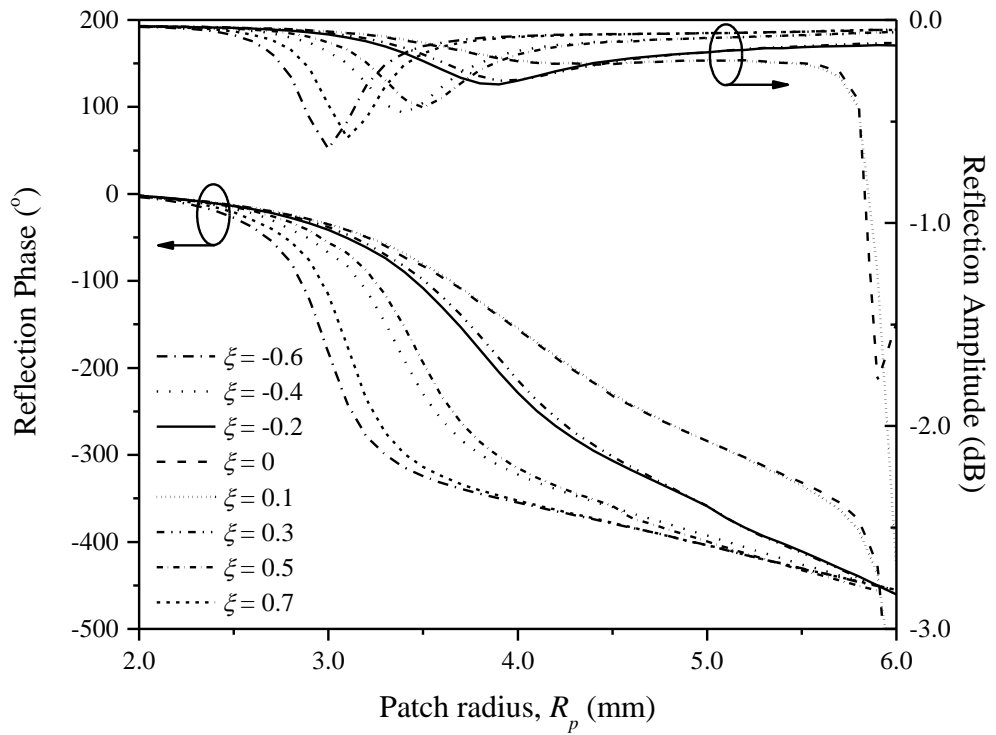
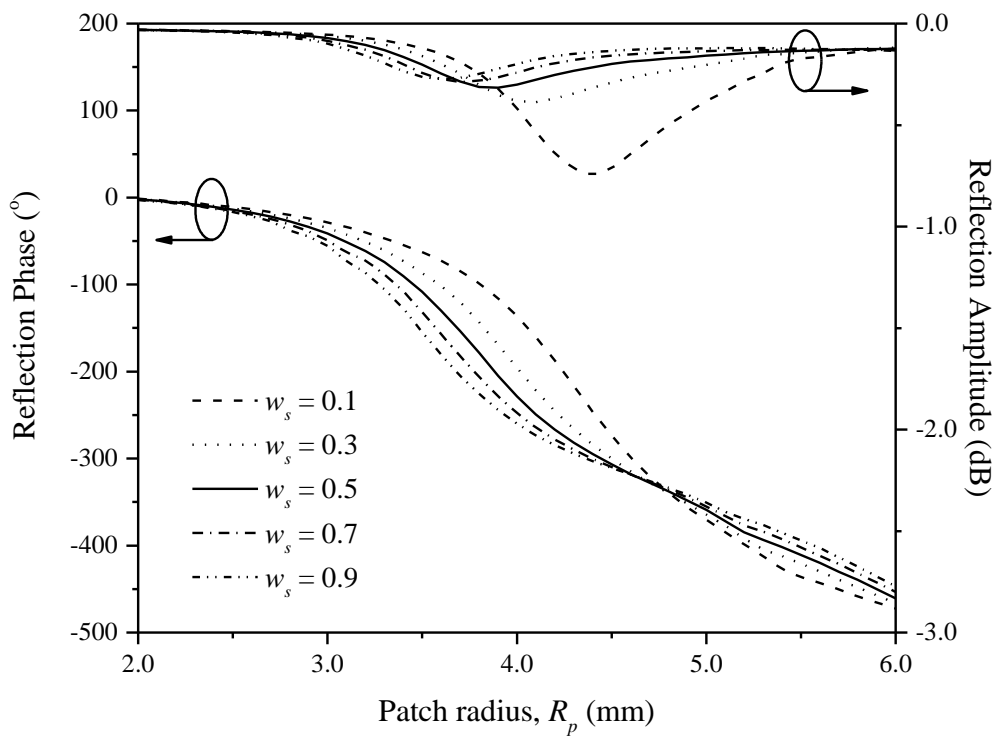
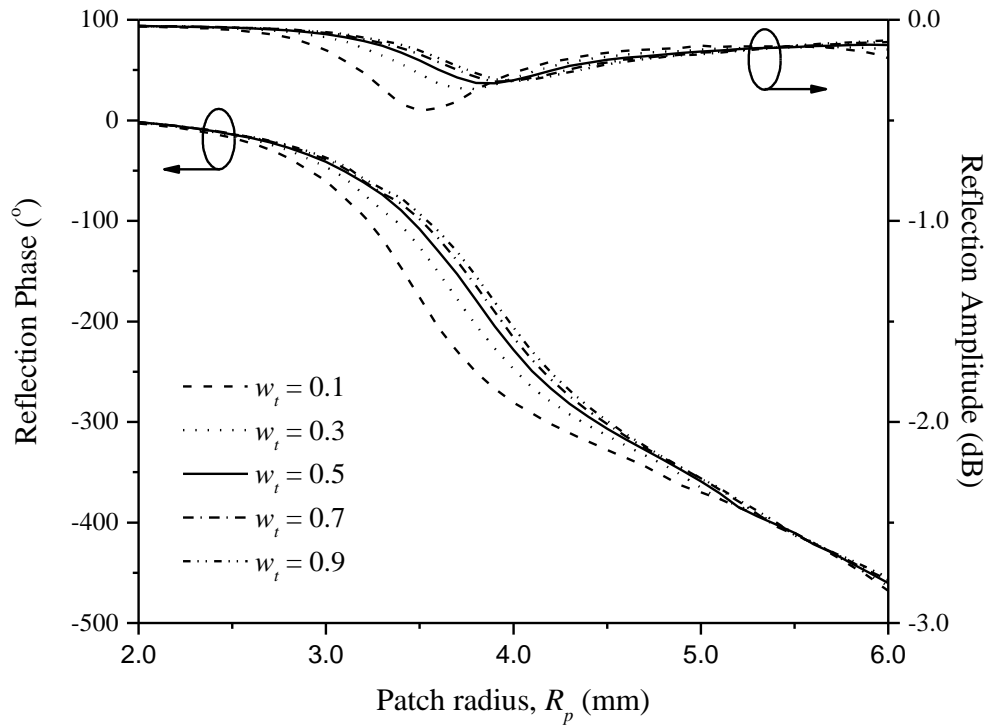


Figure 5.13: Effect of  $\xi$  on the reflection amplitude and phase responses at  $f_o = 9.0$  GHz and  $\theta_i = 20^\circ$  ( $h = 5.7$  mm,  $w_s = 0.5$  mm,  $w_t = 0.5$  mm).



(a)



(b)

Figure 5.14: Effect of  $w_s$  and  $w_t$  on the reflection amplitude and phase responses at  $f_o = 9.0$  GHz and  $\theta_i = 20^\circ$ . (a)  $h = 5.7$  mm,  $\xi = -0.2$ ,  $w_t = 0.5$  mm. (b)  $h = 5.7$  mm,  $\xi = -0.2$ ,  $w_s = 0.5$  mm.

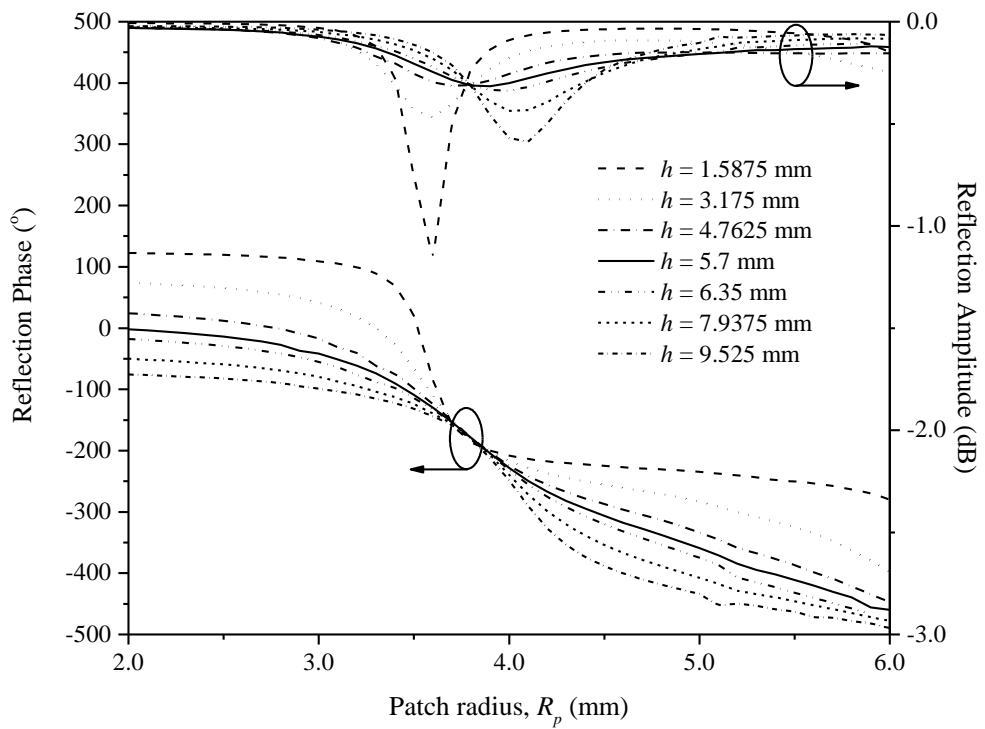


Figure 5.15: Effect of  $h$  on the reflection amplitude and phase responses at  $f_o = 9.0$  GHz and  $\theta_i = 20^\circ$  ( $\xi = -0.2$ ,  $w_s = 0.5$  mm).



From Figure 5.1, the proposed unit element is a circular patch loaded with unequal slots where a linearly  $y$ -polarized plane wave is incident on the element. The dependency of the wave incident angle on the reflection phase response is further analysed. Figure 5.16 shows the wave incident in  $\theta_i$  ( $xz$ -plane) and  $\varphi_i$  ( $yz$ -plane) orientations. As the structure is symmetrical in the  $yz$ -plane, only  $\varphi_{i,u}$  is considered in this analysis.

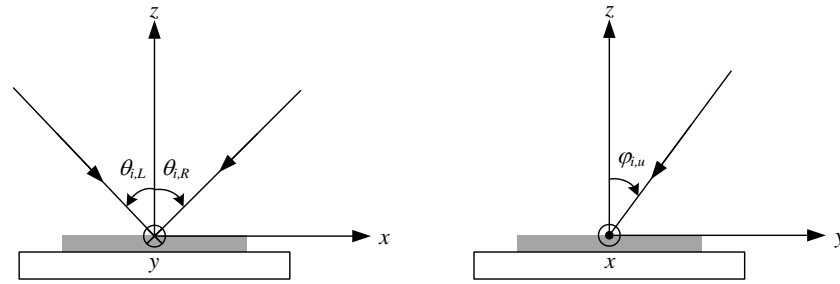
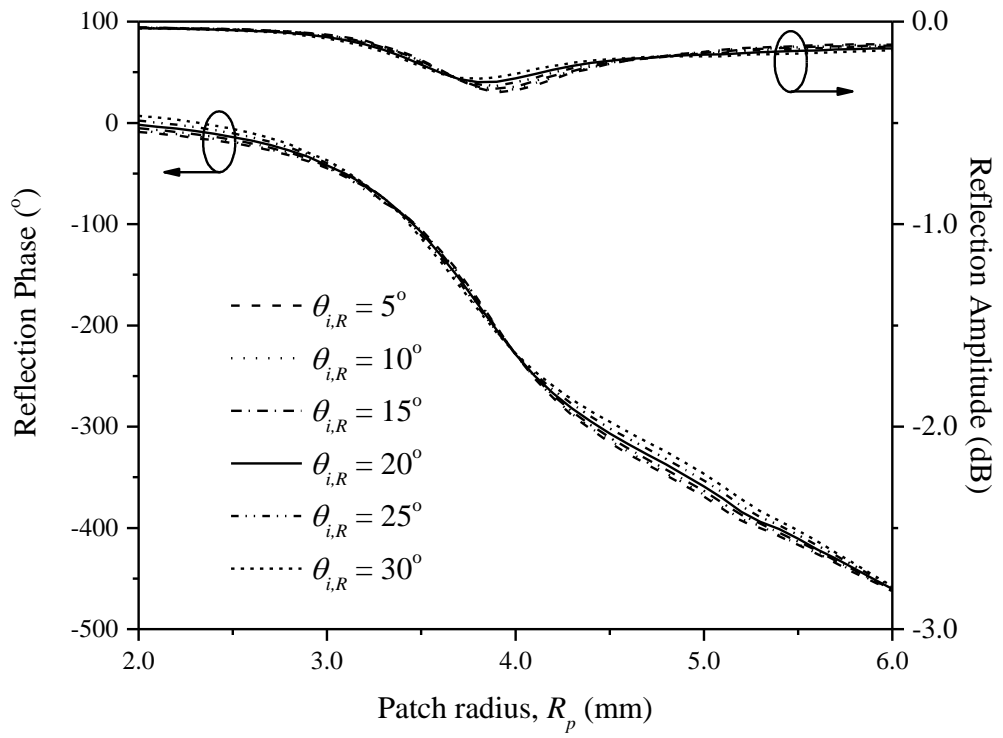
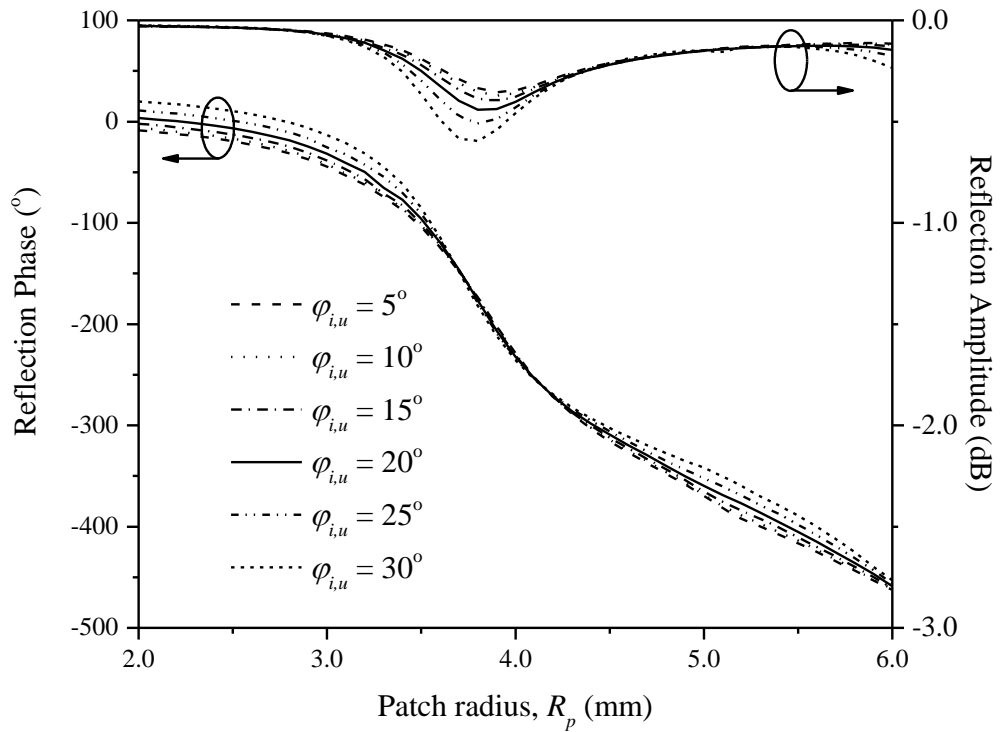


Figure 5.16: Wave incident at  $\theta_i$  ( $xz$ -plane) and  $\varphi_i$  ( $yz$ -plane) orientations.

The effects of the wave incident angles on the reflection amplitude and phase responses for  $\theta_{i,R}$  ( $xz$ -plane) is shown in Figure 5.17 (a), while for the case of  $\theta_{i,L}$  ( $xz$ -plane) can be obtained from Figure 5.3 (b). It can be seen from Figure 5.17 (a) that the reflection amplitude and phase responses are almost similar to the case of  $\theta_{i,R}$ . The proposed element design is insensitive to the incident angles in the  $xy$ -plane, as can be seen from Figure 5.17 (c), where the phase curves of  $\theta_{i,L}$  and  $\theta_{i,R}$  are overlapped. With reference to Figure 5.17 (b), the effect of incident angle  $\varphi_{i,u}$  in the  $yz$ -plane has a minimum effect on the phase response. Overall, the incident angle of  $\theta_i$  in the  $xz$ -plane has a better reflection amplitude and phase responses as compared to  $\varphi_i$  in the  $yz$ -plane as shown in Figure 5.17 (c). Hence, the field incident angle  $\theta_{i,L} = 20^\circ$  is selected as it gives the optimum location to avoid feed blockage while maintaining a good reflectarray performance.



(a)



(b)

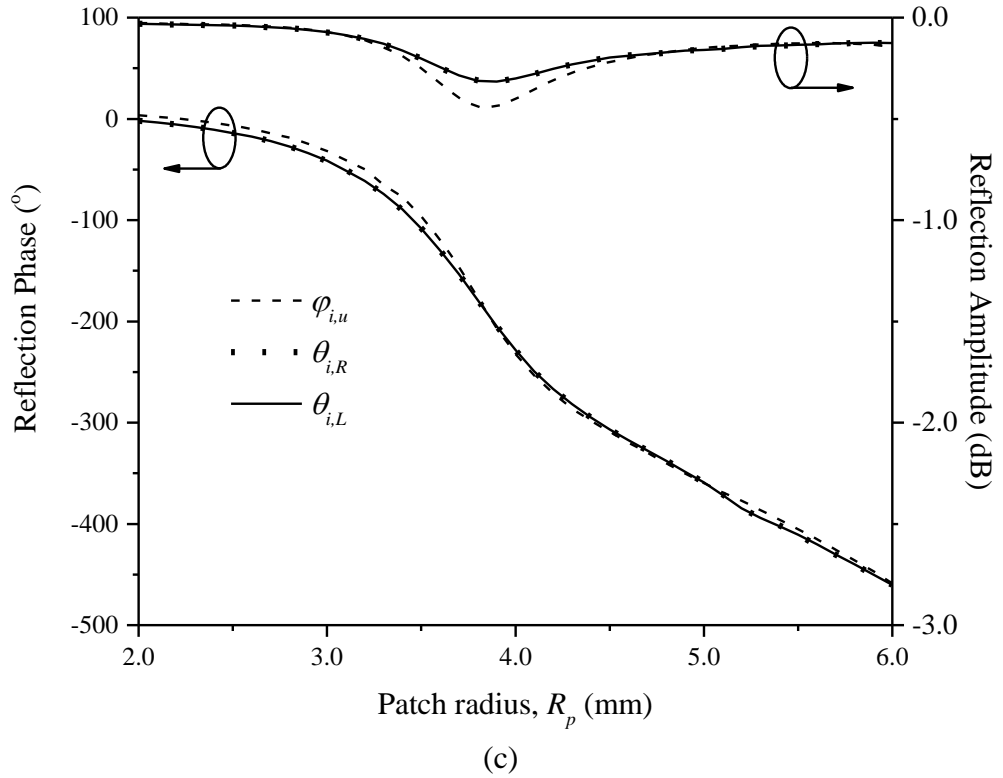
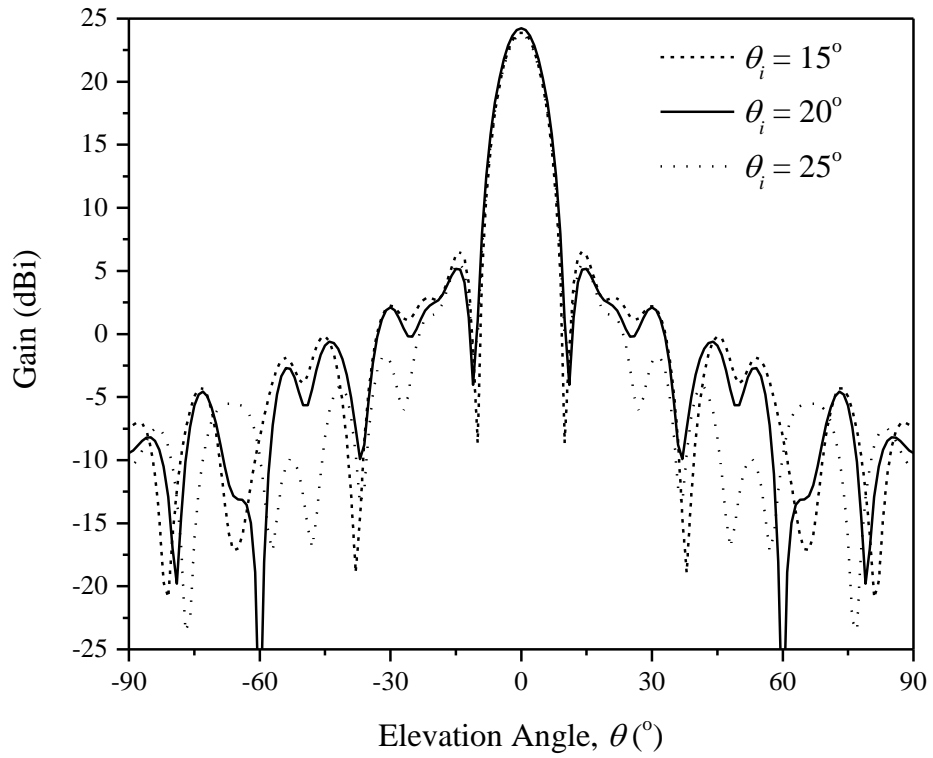


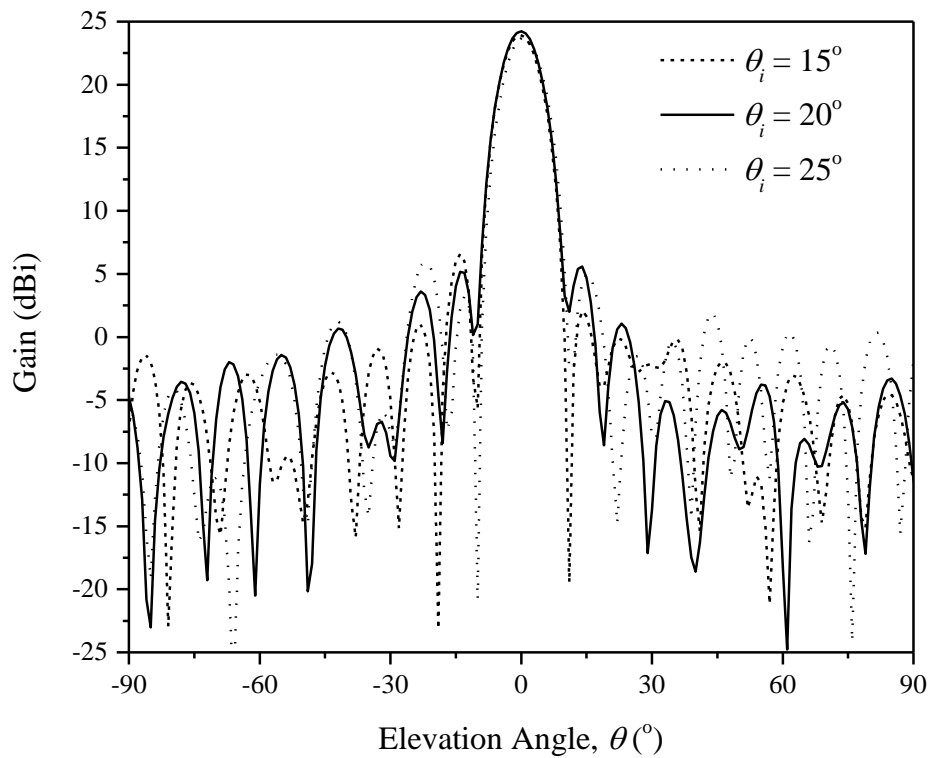
Figure 5.17: Effect of incident angles on the reflection amplitude and phase responses of the proposed unit element at  $f_o = 9.0$  GHz. (a)  $\theta_{i,R}$  in  $xz$ -plane orientation, (b)  $\varphi_{i,u}$  in  $yz$ -plane orientation and (c) comparison for  $\theta_i = 20^\circ$  in  $xz$ -plane and  $\varphi_i = 20^\circ$  in  $yz$ -plane.

### 5.5.2 Reflectarray Performance

Next, the performances of the reflectarray are studied for different wave incident angles ( $\theta_i$ , in  $xz$ -plane). Figure 5.18 shows that the beam in the boresight direction remains almost the same for  $\theta_i \leq 25^\circ$ . For all cases, the levels of the side lobes are at least 20 dB lower than the main beam. As can be seen in Figure 5.19, the antenna gain bandwidth can be tuned by adjusting the incident angle. An optimum -1-dB bandwidth of 14.2% is achievable at  $\theta_i = 20^\circ$ . When  $\theta_i$  is reduced to  $15^\circ$ , the gain bandwidth decreases to  $\sim 11.8\%$ . This is due to the blockage of the feed horn.



(a)



(b)

Figure 5.18: Simulated (a) *E*- and (b) *H*- plane radiation patterns of the reflectarray at 9.3 GHz for different incident angles.

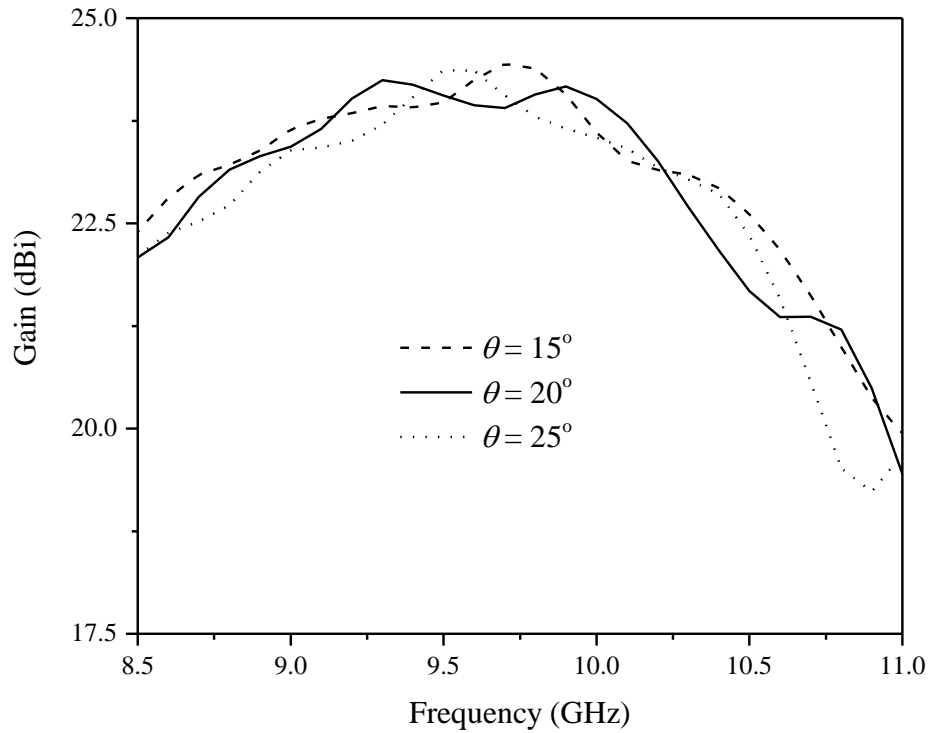
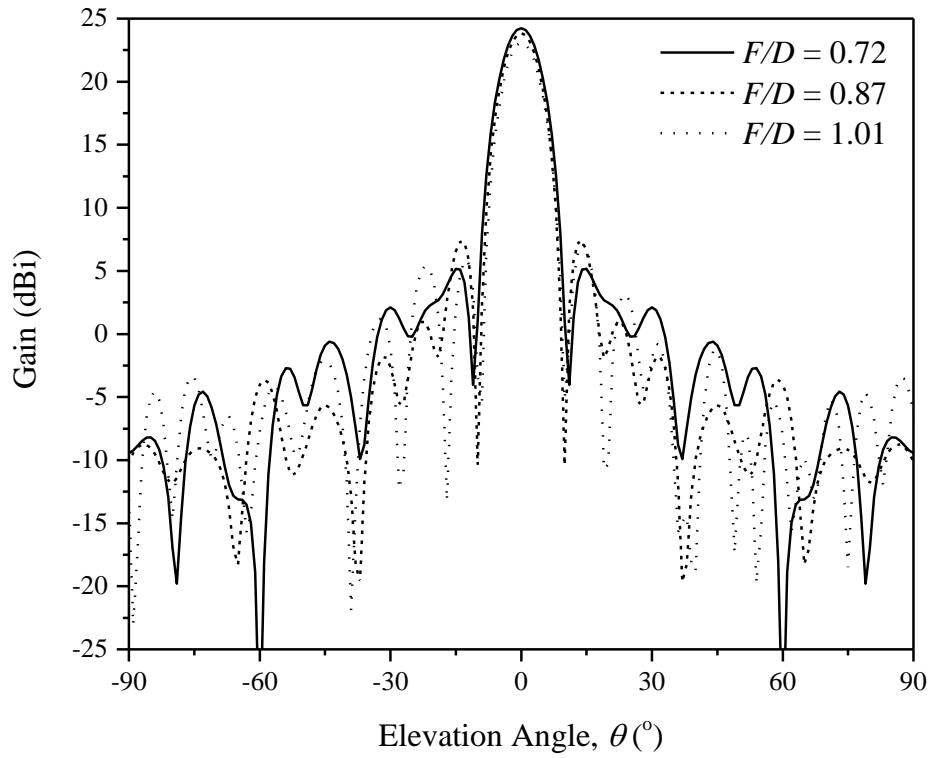
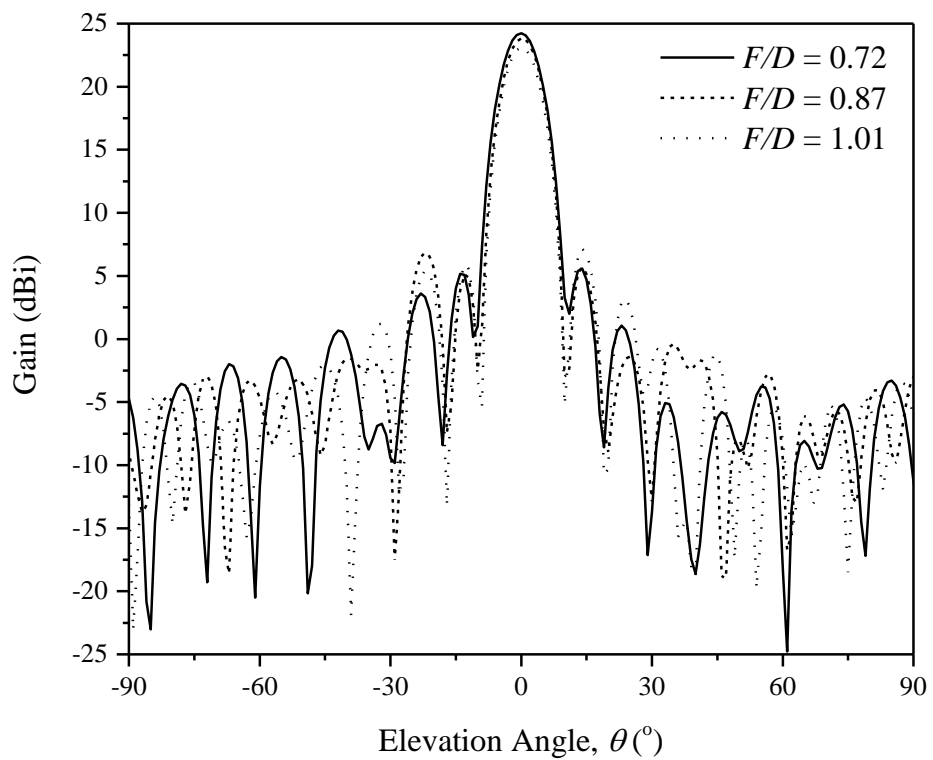


Figure 5.19: Simulated antenna gains of the reflectarray as a function of frequency for different incident angles.

Figure 5.20 shows the effects of  $F/D$  on the radiation characteristics of the proposed reflectarray. When the  $F/D$  value is decreased, the gain improves in the boresight direction. Nearer feed distance also causes the antenna gain and its bandwidth to increase, as shown in Figure 5.21, where the gain and bandwidth are found to have increased by  $\sim 2\%$ , respectively. In this case, the  $F/D$  ratio is set to be 0.72 with a focal distance of 150 mm. This is the minimum distance that the feed horn can be located while maintaining the farfield criterion.



(a)



(b)

Figure 5.20: Simulated (a)  $E$ - and (b)  $H$ - plane radiation patterns of the reflectarray at 9.3 GHz for different  $F/D$  ratios.

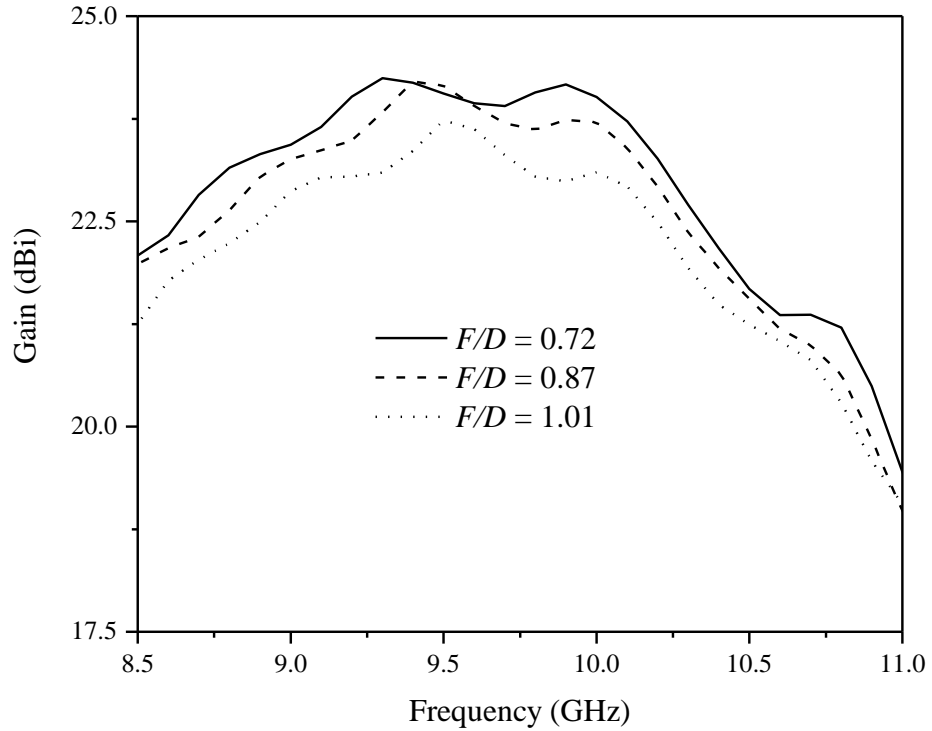


Figure 5.21: Simulated antenna gains of the reflectarray as a function of frequency for different  $F/D$  ratios.

## 5.6 Comparative Study

Table 5.2 compares the proposed reflectarray with other single-layer reflectarrays. As compared with previous works using circular patches (Hasani et al., 2010) and (Liu et al., 2017), the proposed reflectarray has achieved better -1-dB gain bandwidth and much lower sidelobes. Following is the comparison with those using multi-ring structures (Han et al., 2017), (Mohammadi et al., 2018) and (Bodur et al., 2018). Although the reflectarray demonstrated by Han (Han et al., 2017) is able to reach a much broader bandwidth, it requires the use of a complex structure, which consists of three rings and delay lines, to attain multi-resonant characteristics. Moreover, a mirror symmetry arrangement is needed to decrease the cross-polarization level. The configuration proposed by

Mohammadi (Mohammadi et al., 2018) has employed an additional layer of high-dielectric and lossy substrate for increasing the phase range. The usable geometrical range of the reflectarray in Bodur's work (Bodur et al., 2018) is less than 2 mm and the corresponding phase sensitivity is high. On top of that, its sidelobes are also very high. In contrast, the proposed reflectarray has a simpler structure and it can achieve lower sidelobes.

Table 5.2: Comparison of the Proposed Reflectarray with Other Works.

Ref. No.	This Work	(Hasani et al., 2010)	(Liu et al., 2017)	(Han et al., 2017)	(Mohammadi et al., 2018)	(Bodur et al., 2018)
Element Size [ $\lambda_o$ ]	0.54	0.33	0.52	0.47	0.33	0.53
Phase Range [°]	458	>500	~500	600	423	430
Aperture Size [mm]	208	270	218	266	300	144
Profile [ $\lambda_o$ ]	0.2	0.03	0.15	0.09	0.08	0.2
-1-dB Gain BW [%]	11.8	~ 7	24 (1.5-dB Gain BW)	31.5	16.3	23
-3-dB Gain BW [%]	20.1	18	~ 17	-	-	29
AE [%]	42	25	22	50	44.27	40
Peak Gain [dBi]	23.4	24	25.2	25.8	26.4	21.6
Max. Cross-polarization [dB]	-25	-	< -25	< -26	- 31.6	-24.9
Max. Sidelobe level [dB]	-20	-	-18	-20	-20.4	-
Frequency [GHz]	9.0	11.7	15	10	10	10



## 5.7 Conclusion

A single-layer circular patch reflectarray element loaded with a pair of unequal slots has been employed to enhance the phase tuning ability and provide a low-profile reflectarray design at the same time. The phase range can be optimised by a simple equation that pegs the two unequal slots to the patch radius, producing a broad phase of  $458^\circ$  with a low reflection loss of less than 0.5 dB. The linearity and sensitivity of the phase curve can be easily achieved by adjusting the ratio of the two unequal slots changeable according to the simple design equation. The proposed reflectarray can achieve a broad -1-dB gain bandwidth of 11.8 % with an antenna gain of 23.4 dBi and an aperture efficiency of 42 % at the centre frequency of 9.3 GHz. The proposed reflectarray is simple in structure, and it can achieve a smooth phase curve, low cross-polarized radiation field, and low sidelobes.

## CHAPTER 6

### BROADBAND REFLECTARRAY WITH CLOSELY COUPLED INTER-LAYER CIRCULAR RING-PATCHES

#### 6.1 Introduction

In reflectarray element design, the reflection phase not only depends on individual element structure, but the mutual coupling between the adjacent elements is also important, and it can affect the phase response (Karnati et al., 2012). The synthesis of reflectarray can be done by varying the geometrical sizes of phase-shifting elements at a particular design frequency. When the element itself is translated into a full-fledged reflectarray, it may cause abrupt geometrical variation in the neighbouring elements. Such variation does not benefit the bandwidth performance, particularly for the conventional moderate-sized reflectarray (Li et al., 2011).

This chapter explores the use of the conventional circular patch reflectarray element to improve the phase tuning ability and enhance the bandwidth performance. Two closely coupled circular ring-patches are tactfully stacked on the two sides of a single-layer substrate for designing a broadband reflectarray. The inter-layer coupling mechanism is explored for minimizing the mutual coupling of the neighbouring elements. It can overcome the shortcoming of the abrupt geometric variation among the neighbouring elements. By mitigating the coupling between the elements, the proposed reflectarray can

achieve wideband behaviour. This is due to the broadening of the operational bandwidth of the element. A unique design equation that is linked to the geometrical dimensions of the ring-patches is employed for generating the reflection phase curve, which will be used for designing a full-fledged reflectarray to achieve broadband performance.

## 6.2 Reflectarray Unit Element Design and Analysis

With reference to Figure 6.1, the unit element is placed at one end of the Floquet cell while a linearly  $y$ -polarized plane wave is launched from the wave port (Port 1) on the other end. It propagates in the  $xz$ -plane with an incident angle of  $\theta_i = 15^\circ$ . The unit element is located 80 mm away from the wave port. In this simulation, the reference plane is de-embedded from the wave port to the top surface of the radiating aperture. Figure 6.2 illustrates the proposed unit element that is designed using a single piece of RO4003C substrate ( $t = 0.8128$  mm,  $\epsilon_{r1} = 3.38$ , and  $\tan \delta = 0.0027$ ), with a ground plane separated by an air layer ( $h = 4.0$  mm) to achieve a smoother and linear phase response. The element size is set to be  $L_x = L_y = 16$  mm ( $0.49\lambda_o$  at  $f_o = 9.2$  GHz). The size is kept at  $< 0.5\lambda_o$  to prevent the presence of the grating lobes generation in the farfield radiation. The proposed unit element configuration consists of a single layer RO4003C substrate sandwiched between two concentric circular ring-patches, with its geometric parameters given in Figure 6.2 (a). This design allows more degree of freedom for the phase tuning.

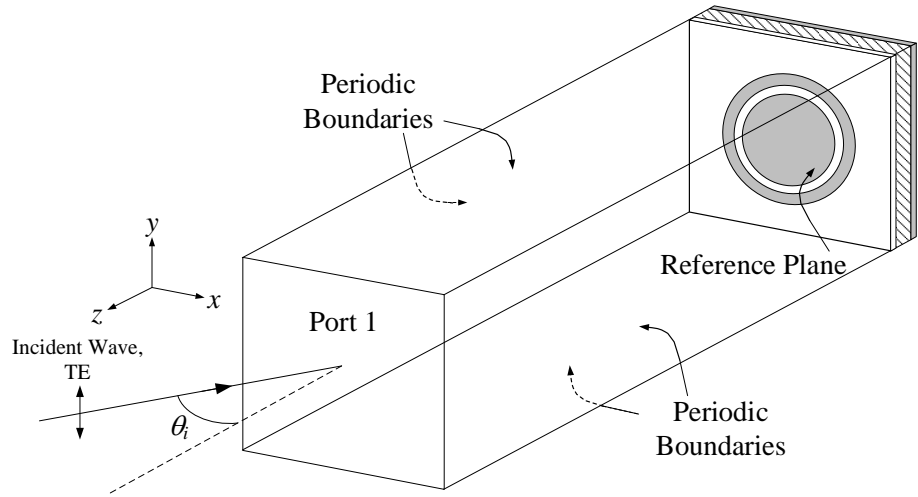
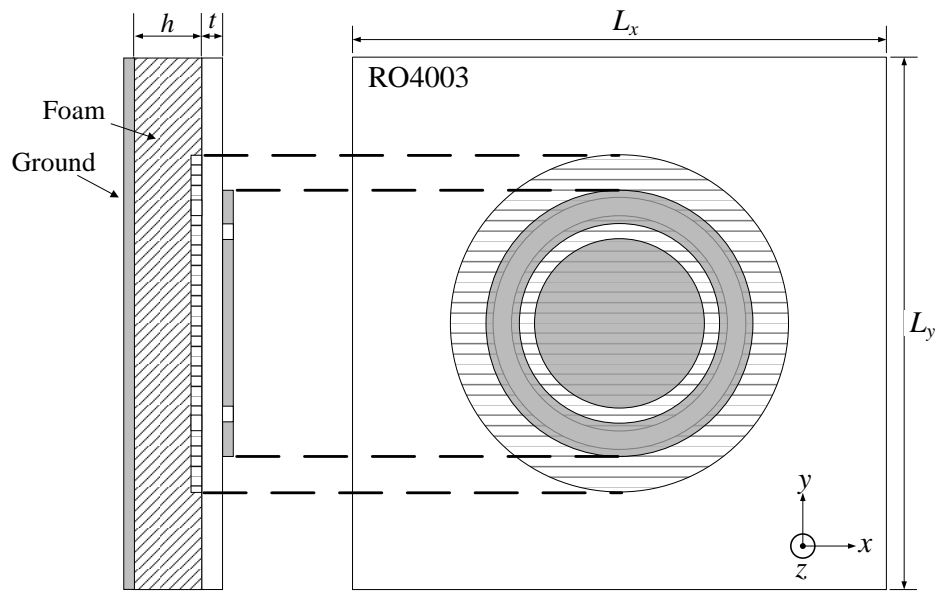
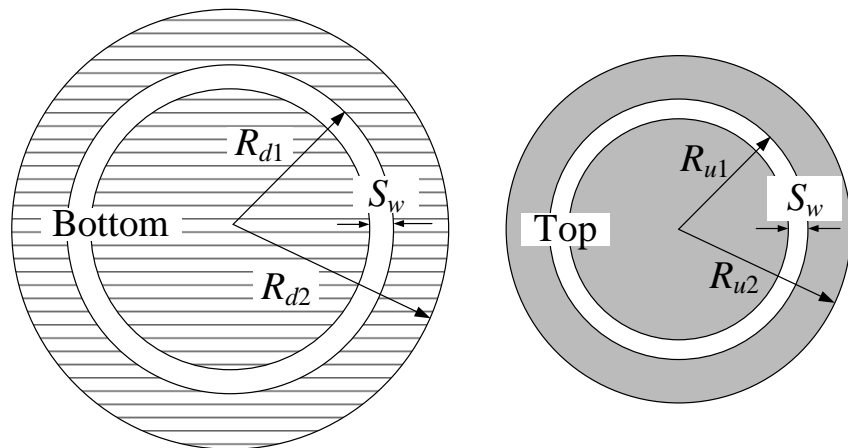


Figure 6.1: Simulation model of the unit element in a Floquet cell.



(a)



(b)

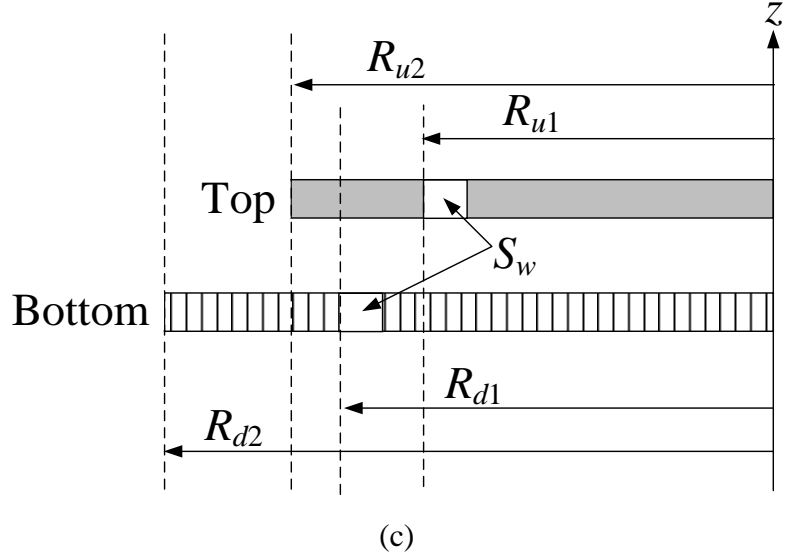


Figure 6.2: (a) The proposed unit element, (b) layouts, and (c) cross-sectional view of the top and bottom circular ring-patches.

The reflection phase curve of the unit element is generated in a unique way by using two linear equations defined in Equation (6.1).

$$\left. \begin{aligned} R_{u1} &= c_{u1}\rho_{ur}, & R_{u2} &= c_{u2}\rho_{ur} \\ R_{d1} &= c_{d1}(\rho_{ur} + \Delta), & R_{d2} &= c_{d2}(\rho_{ur} + \Delta) \end{aligned} \right\} \quad (6.1)$$

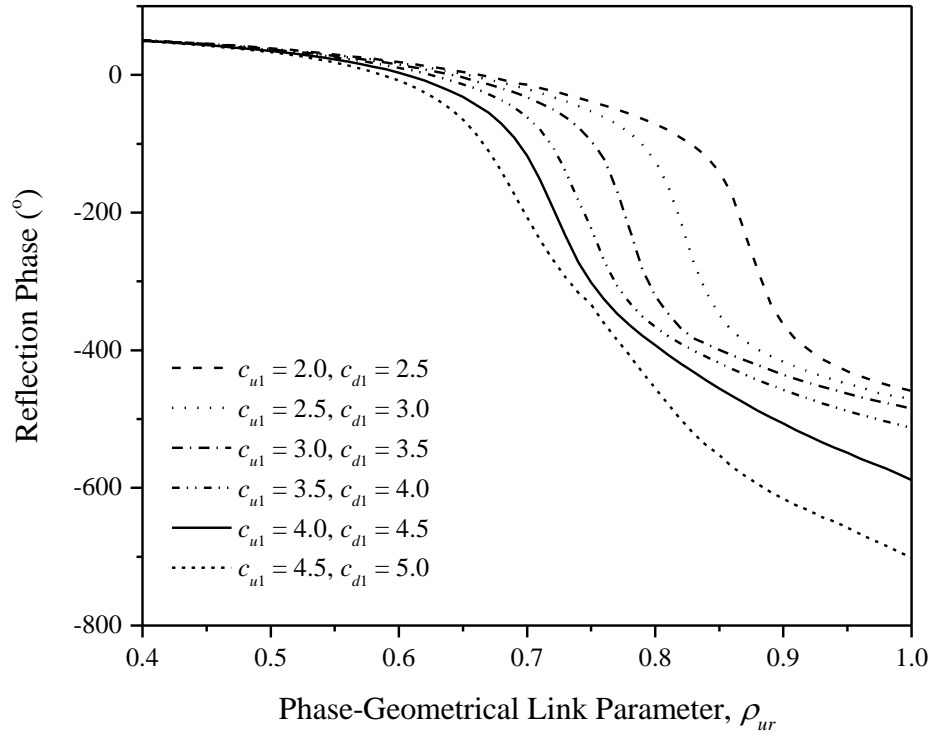
where  $\rho_{ur}$  is a phase-geometrical link parameter that is related to the actual radii of the top ( $R_{u1}, R_{u2}$ ) and bottom ( $R_{d1}, R_{d2}$ ) ring-patches. Changing  $\rho_{ur}$  causes the radii to vary simultaneously but with different weights, as the linear equations are scaled by different coefficients ( $c_{u1}, c_{u2}, c_{d1}, c_{d2}$ ). Here, the coefficients for  $R_{u2}$  and  $R_{d2}$  are fixed at  $c_{u2} = 5$  and  $c_{d2} = 6$ , respectively, so that the bottom ring-patch is always slightly larger than the top ring-patch by a fixed proportion ( $R_{u1}, R_{u2} < R_{d1}, R_{d2}$ ). Also, it is to keep the maximum diameter of the bottom ring ( $2R_{d2}$ ) below 12 mm to avoid strong mutual coupling with the adjacent elements.

The slot width is fixed at  $S_w = 0.5$  mm.  $\Delta$  is a small real number that is intentionally applied to ensure the location of the slot at the bottom layer is optimum to produce linear phase responses. Table 6.1 summarises the design parameters. Their parametric analysis can be found in the following discussion and Section 6.5.1 accordingly.

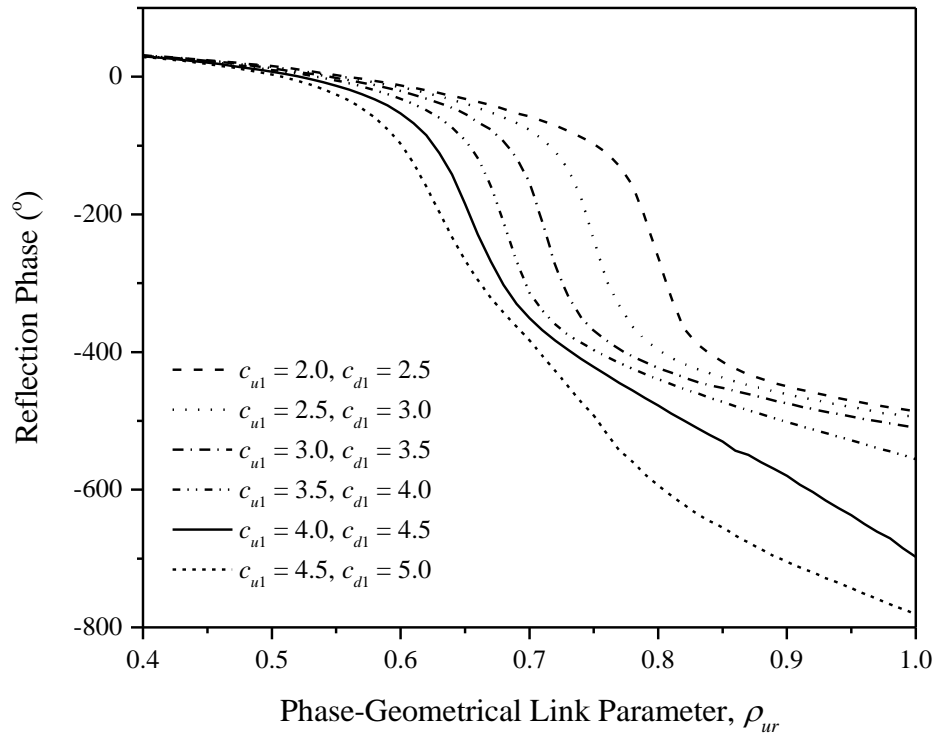
Table 6.1: Design Parameters.

Parameter	Values	Parameter	Values
$t$	0.813 mm	$c_{u1}$	4
$h$	4.0 mm	$c_{u2}$	4.5
$S_w$	0.5 mm	$c_{d1}$	5
$L_x$	16 mm	$c_{d2}$	6
$L_y$	16 mm	$\Delta$	0.06
		$\rho_{ur}$	0.6-0.9

It is always very desirable to make the reflection phase curve smooth across a large frequency range with low reflection loss. Hence, parametric analysis is carried out to obtain the optimum relationship that links the actual geometrical radii to achieve optimum phase responses and maintain low mutual coupling simultaneously. Figure 6.3 shows the reflection phase responses by varying  $\rho_{ur}$  in the range of 0.4 to 1 for different combinations of  $(c_{u1}, c_{d1})$  at the frequencies of 8.4 GHz, 9.2 GHz, and 12.1 GHz, by letting  $\Delta = 0.06$ . The coefficients  $c_{u1}$  and  $c_{d1}$  are changed in the ranges of 2 - 4.5 and 2.5 - 5, respectively, in an ascending manner accordingly. The phase range is found to be optimum for  $c_{u1} = 4.0$  and  $c_{d1} = 4.5$ , providing a broad and more linear phase range over the frequency range. It should be mentioned that a phase range of  $360^\circ$  is usually sufficient for designing a full-fledge reflectarray.



(a)



(b)

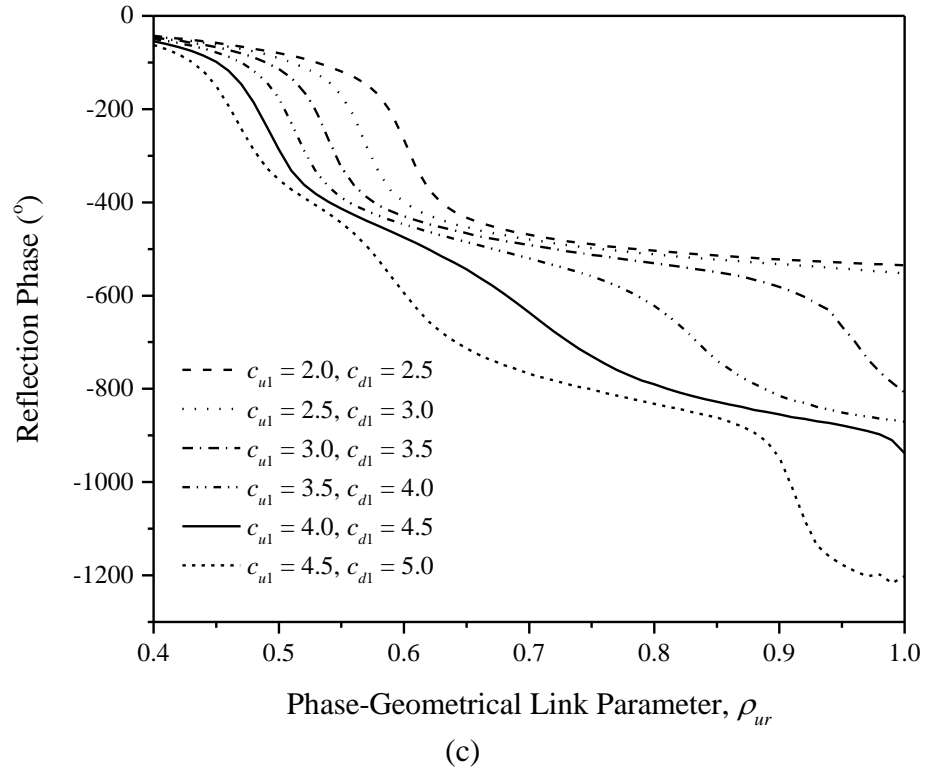


Figure 6.3: Reflection phase responses as a function of  $\rho_{ur}$  at different frequencies: (a) 8.4 GHz, (b) 9.2 and (c) 12.1 GHz.

An optimisation scheme is then employed for analysing the parameter's changes and obtaining the optimum phase curve so that it can cover the broadest frequency range. Since the required phase shift is a relative quantity, the reflection phase curves in Figure 6.3 are normalized to  $0^\circ$  at  $\rho_{ur} = 0.9$ . The normalized phase curve for the combination of coefficients  $(c_{u1}, c_{d1})$  at  $f_o = 9.2$  GHz is first selected and denoted as  $\varphi(f_o)$ . With the same combination of coefficients  $(c_{u1}, c_{d1})$  for other frequencies  $f_i$ , the phase curve is denoted as  $\varphi(f_i)$ . The difference between  $\varphi(f_i)$  and  $\varphi(f_o)$  is then monitored for  $N$  data points of  $\rho_{ur}$ , which is taken in the range of 0.6 – 0.9. This range provides the even phase response curve changes within the entire frequency range of 8.4 GHz – 12.4 GHz, with a sufficient phase range of  $> 360^\circ$ . A cost function, which denotes



the mean phase difference, is finally defined in Equation (6.2) by averaging the differences over the  $N$  points, where Figure 6.4 shows its values across the frequencies. A maximum threshold is set for controlling the cost function below  $50^\circ$ . By controlling the mean phase difference below the threshold, a linear and broad phase range can be attained across frequencies. A lower threshold provides better element bandwidth performance (Bozzi et al., 2003). The maximum reflection amplitude is also plotted within the same figure. Finally, as seen in Figure 6.4, the combination ( $c_{u1} = 4.5$  and  $c_{d1} = 5$ ) is selected as it can keep the cost function below  $50^\circ$  with a reasonably low reflection amplitude of better than  $-1$  dB across the broadest frequency range from 8.4 GHz to 12.1 GHz.

$$\overline{\delta\varphi} = \frac{1}{N} \sum_{n=1}^N |\varphi_n(f_i) - \varphi_n(f_o)| \quad (6.2)$$

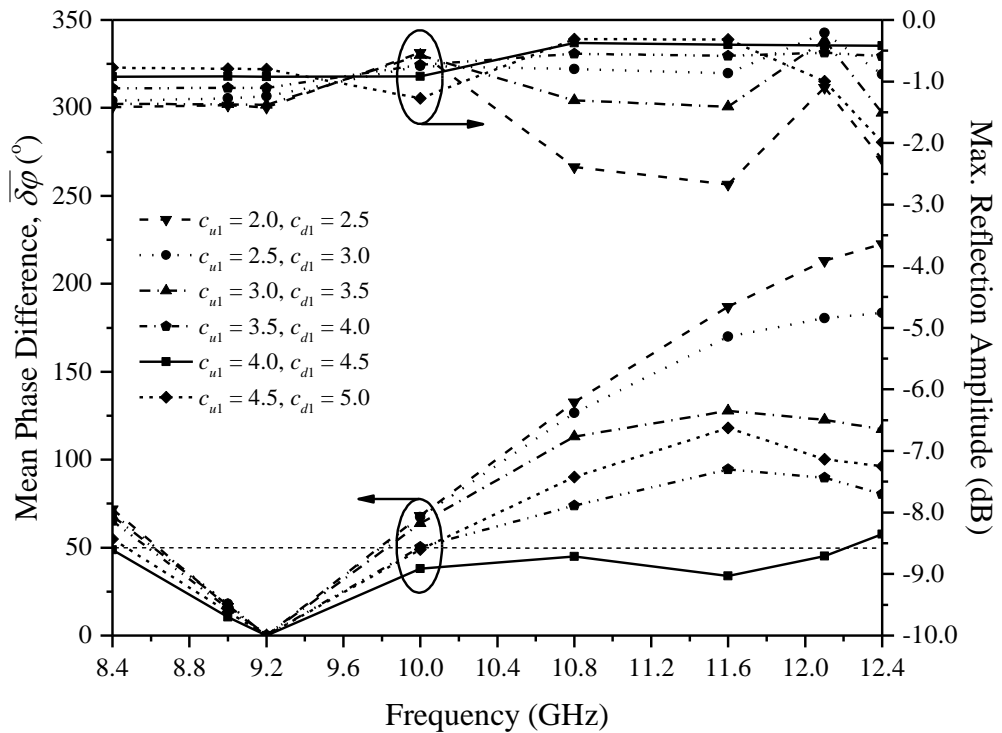


Figure 6.4: Mean phase difference  $\overline{\delta\varphi}$  and maximum reflection amplitude for different combinations of ( $c_{u1}$ ,  $c_{d1}$ ).

More studies have also been conducted to analyse the design parameters further. Figure 6.5 shows the effect of changing  $c_{d1}$ , while keeping the coefficient  $c_{u1} = 4$ . As seen in Figure 6.5,  $c_{d1} = 4.5$  can keep the cost function well below  $50^\circ$  across the frequency, with low reflection amplitude of below -1 dB. By keeping this optimum combination ( $c_{u1} = 4.5$  and  $c_{d1} = 5$ ), the effect of  $\Delta$  is further analysed in Figure 6.6.  $\Delta = 0.06$  is found to be the optimum value for keeping the cost function below  $50^\circ$  while maintaining the reflection amplitude below -1 dB covering the broadest frequency range.

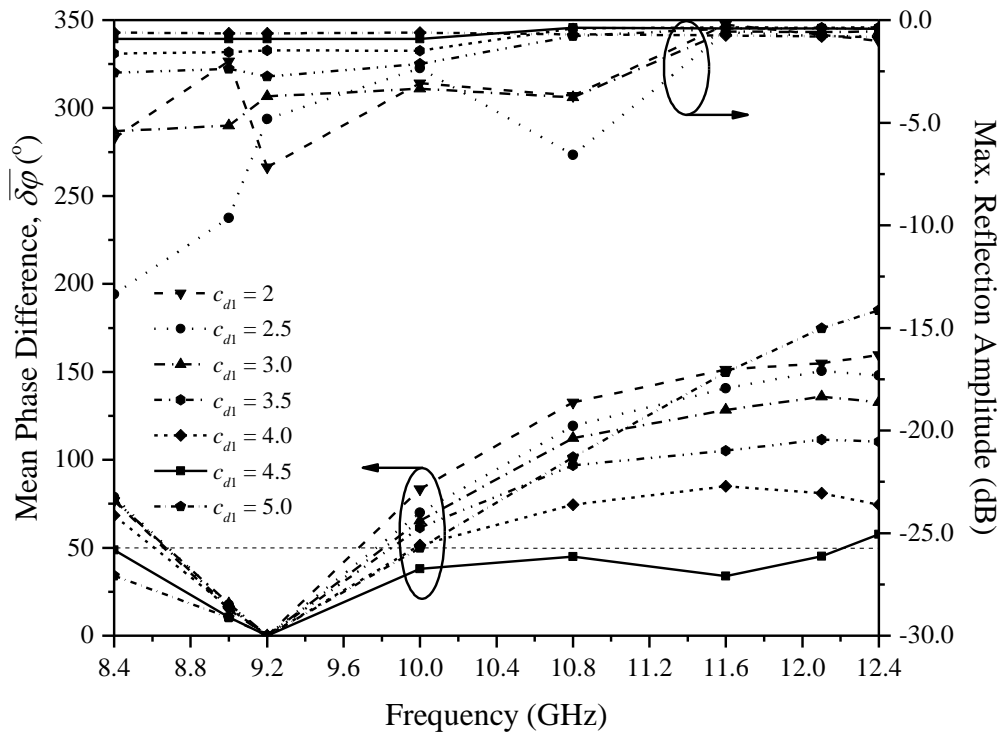


Figure 6.5: Mean phase difference  $\overline{\delta\varphi}$  and maximum reflection amplitude for different values of  $c_{d1}$ .

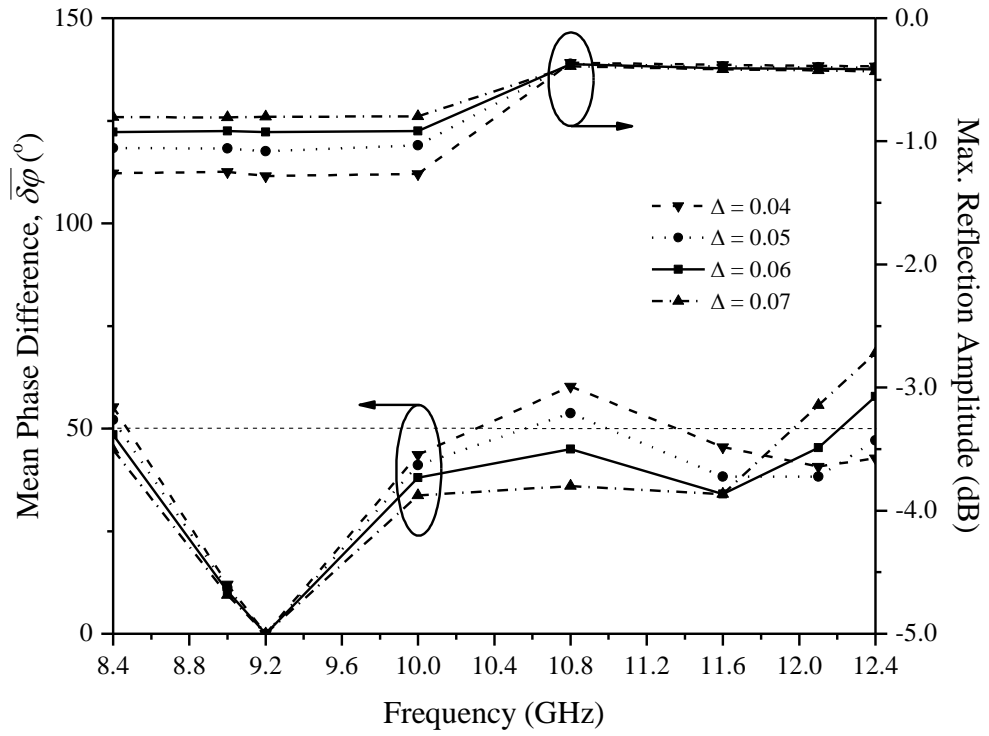


Figure 6.6: Mean phase difference  $\overline{\delta\varphi}$  and maximum reflection amplitude for different values of  $\Delta$ .

Figure 6.7 shows the reflection amplitude and phase responses of the optimised unit element at 8.4, 9.2, 10.0, 10.8, 11.6, and 12.4 GHz. The corresponding phase ranges are found to be  $510^\circ$ ,  $527^\circ$ ,  $475^\circ$ ,  $403^\circ$ ,  $391^\circ$ , and  $366^\circ$ . A broad reflection phase of  $527^\circ$  is achievable at  $f_0 = 9.2$  GHz. The phase curves are found to be linear in all cases, with losses of less than 1 dB.

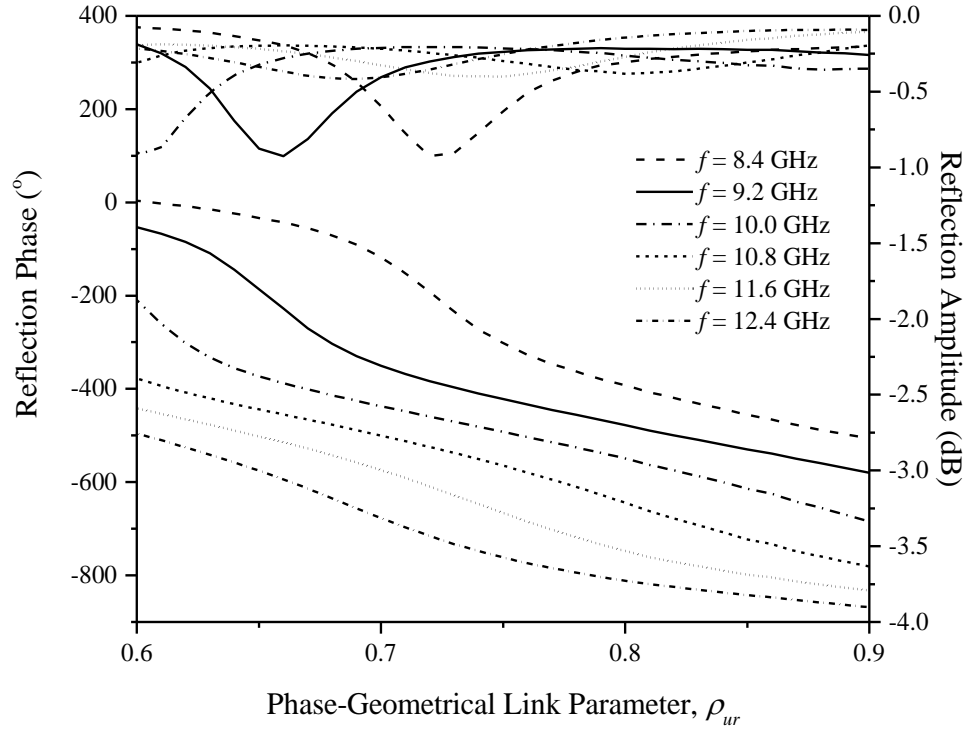


Figure 6.7: Reflection amplitude and phase responses of the proposed unit element for different frequencies at  $\theta_i = 15^\circ$ .

For reflectarray design, the reflection phase response of the unit element is not only dependent on the geometry of the individual element but is also affected by the mutual coupling between the adjacent elements (Karnati et al., 2012). Low mutual coupling between the elements is crucial for maintaining good reflection phase linearity and enhancing large bandwidth performance. Figures 6.8 (a) and (b) are the electric field distributions of the radiating element for the cases of ( $\rho_{ur} = 0.66$ ) and ( $\rho_{ur} = 0.9$ ), respectively, at  $f_o = 9.2$  GHz. The large reflection phase is mainly contributed by the strong inter-layer coupling between the concentric ring-patches. It is observed that the fields are mostly distributed around the inter-layer ring-slot regions, where the mutual coupling between the neighbouring elements is very low. The result suggests that the unequal mutual coupling caused by the abrupt geometrical variation of the

adjacent elements can be minimised. It has improved the bandwidth performance of the reflectarray (Chen et al., 2013). Besides, low field intensity in the central region beneath the circular patch leads to low reflection loss of less than 1 dB (Ethier et al., 2012).

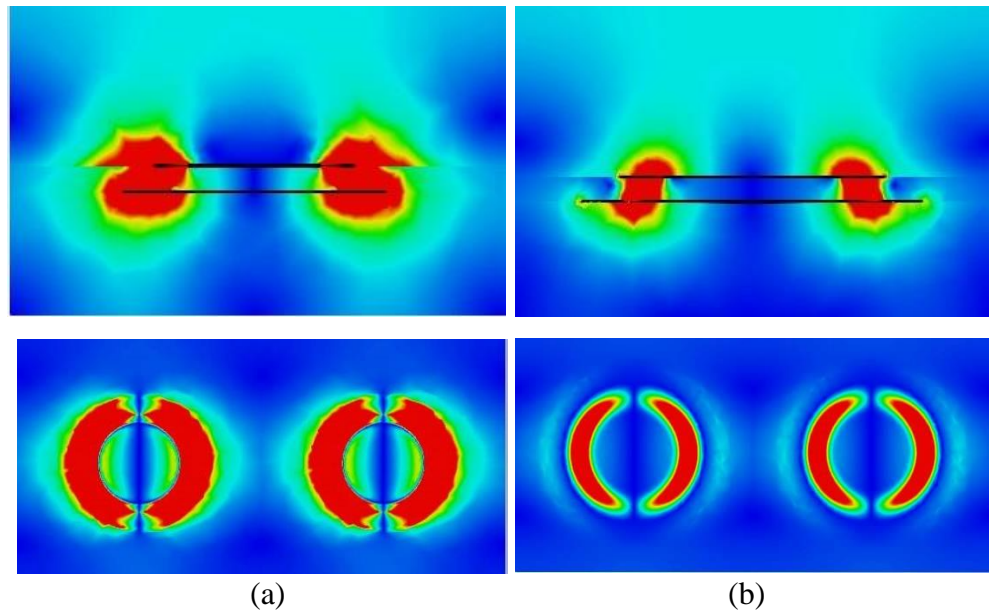
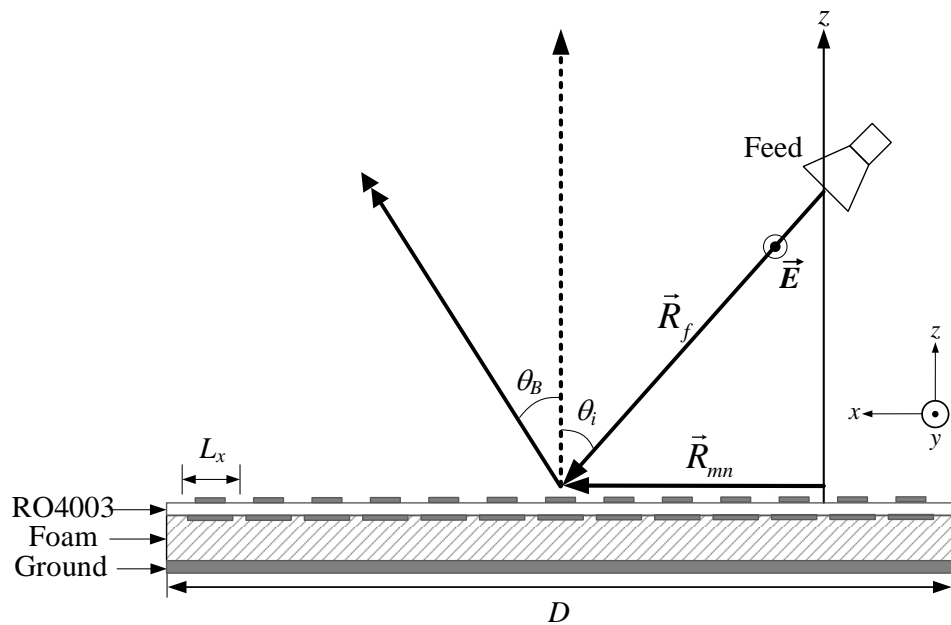


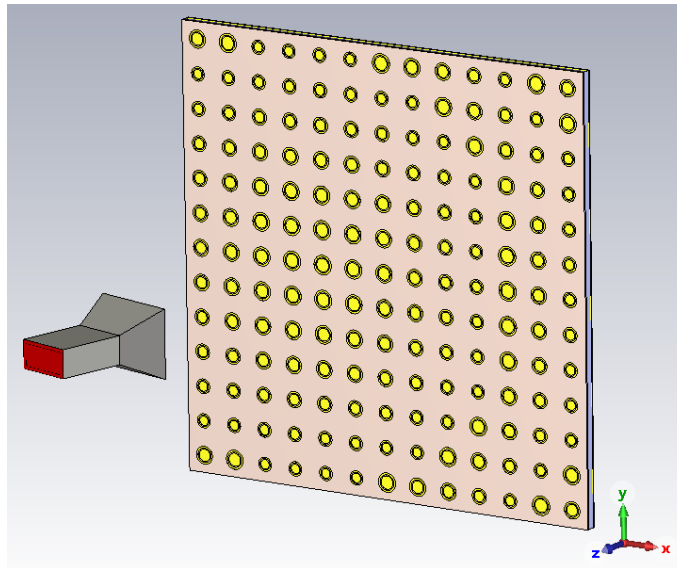
Figure 6.8: Electric field distributions (side and top views) of the radiating element at  $f_o = 9.2$  GHz. (a)  $\rho_{ur} = 0.66$  and (b)  $\rho_{ur} = 0.9$ .

### 6.3 Reflectarray Design Configuration and Analysis

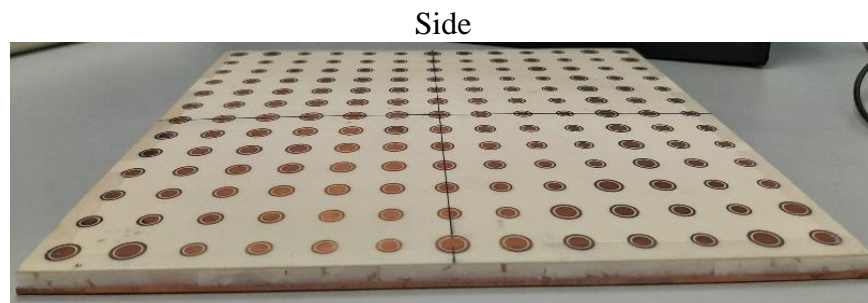
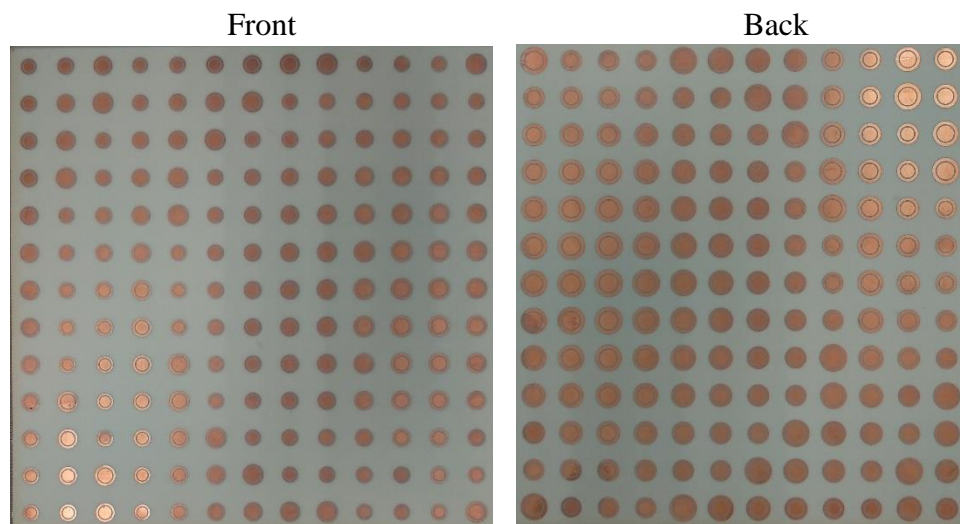
The proposed reflectarray element is then employed to design a  $13 \times 13$  reflectarray, which composes 169-unit elements. Figure 6.9 (a) shows the side view of the proposed reflectarray antenna with the simulation model shown in Figure 6.9 (b). The reflectarray aperture is square in shape with an overall dimension  $D = 13L_x = 208$  mm. A similar linearly polarized X-band pyramidal horn (8.2 GHz – 12.5 GHz) in CHAPTER 5 Section 5.3 is employed to illuminate the reflectarray. The location of the feeding horn is optimised following the recommendation in Yu's work (Yu et al., 2010) to achieve good aperture efficiency. As shown in Figure 6.9 (a), the feed horn is placed at a far-field distance of  $F = 150$  mm from the centre point at an incident angle of  $\theta_i = 15^\circ$ , giving an  $F/D$  ratio of 0.72. The offset feeding method can minimise the feeder blockage while maintaining a small incident angle to prevent the grating lobes formation.



(a)



(b)

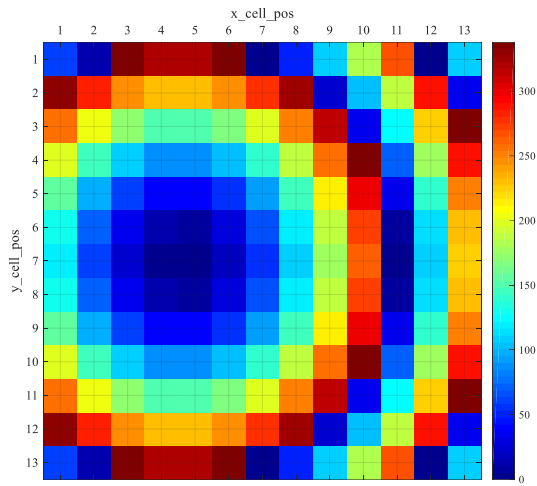


(c)

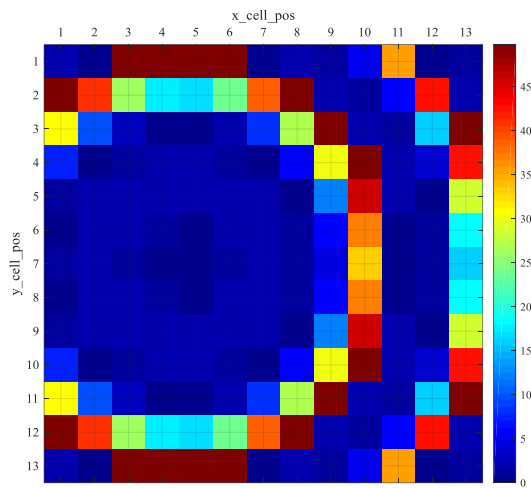
Figure 6.9: (a) Side view of the proposed reflectarray with a feeding horn suspended at  $\theta$ . (b) Simulation model of the reflectarray in CST Microwave Studio<sup>®</sup>, and (c) front, back, and side views of the fabricated prototype.

Figure 6.9 (c) shows the prototype of the proposed reflectarray. The fabrication is carried out using the double-layer photoetching method, which is commonly used in printed circuit board (PCB) prototyping. The substrate is placed over a polystyrene foam with a thickness of  $h = 4.0$  mm and a dielectric constant of  $\epsilon_r \sim 1$ . A flat copper plate is held below the foam as the ground plane. The proposed linearly polarized reflectarray is designed to radiate in the boresight direction ( $\theta_b = 0^\circ$ ). With the use of the ray-tracing method (Rajagopalan et al., 2012), the desired phase shift for each element can be calculated using Equation (2.6). The corresponding dimensions for all the elements can then be extracted from the reflection phase curve in Figure 6.7. The elements are arranged using the conventional topology without special arrangement to achieve low cross-polarization. Figure 6.10 (a) shows the normalised phase distributions used to synthesise the reflectarray. The required phases are determined at the design frequency  $f_0 = 9.2$  GHz. Figures 6.10 (b) and (c) show the normalised phase difference of each element between the two ends of the passband with reference to the design frequency. The maximum phase differences are all observed to be less than  $50^\circ$ , which implies a wideband reflectarray performance (Bozzi et al., 2003).

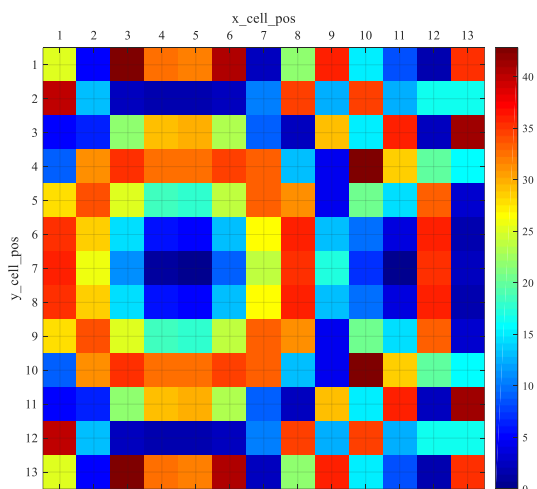




(a)



(b)

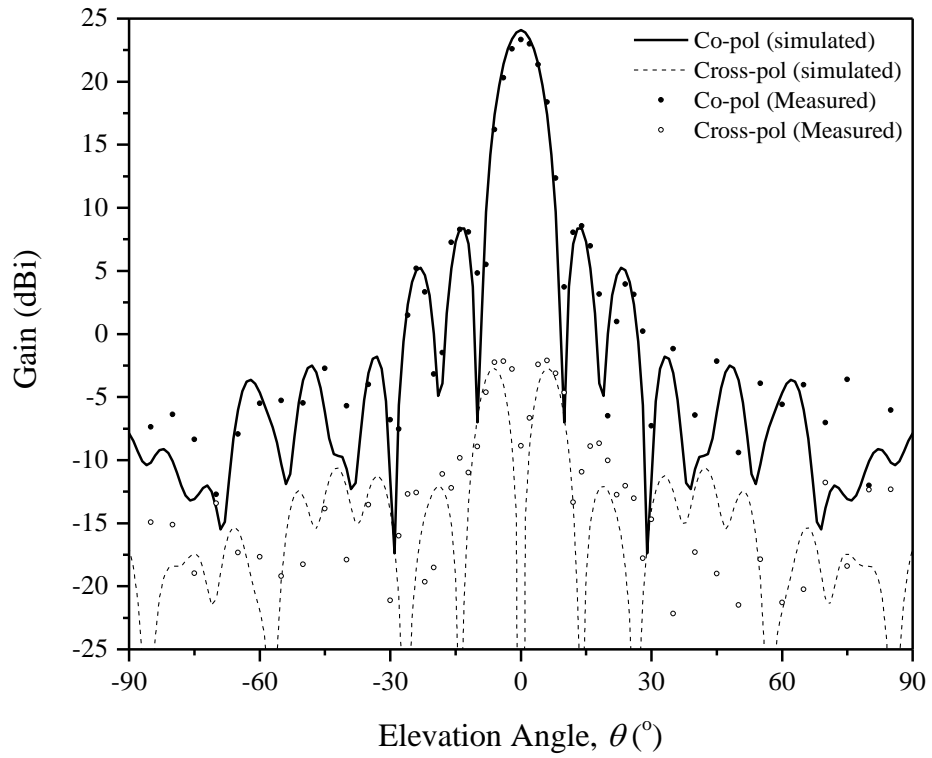


(c)

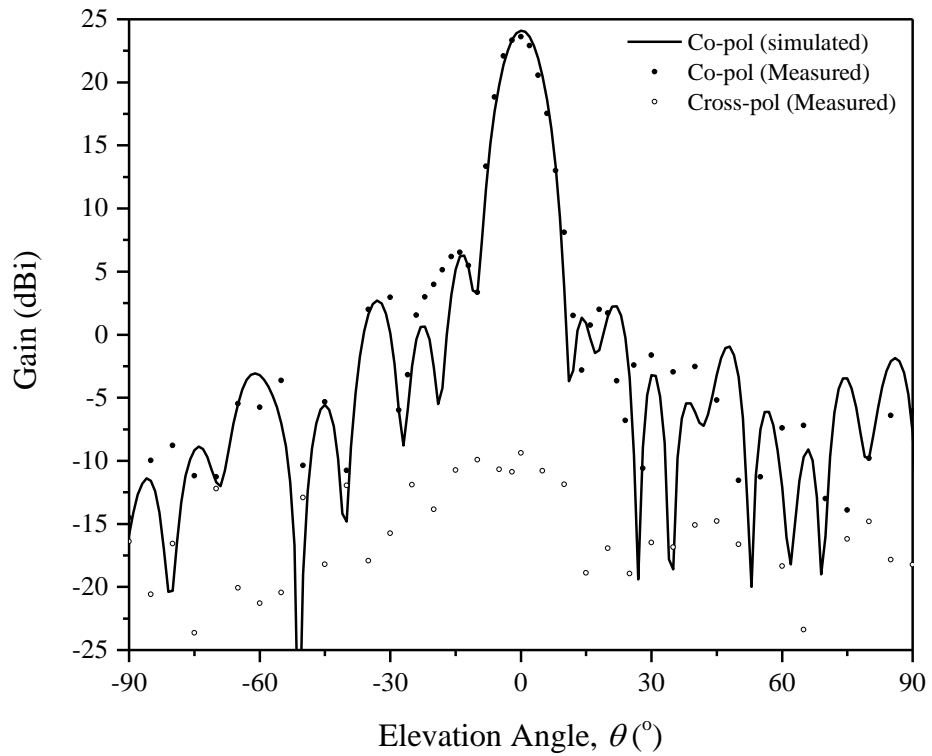
Figure 6.10: (a) The required phase distributions at  $f_o = 9.2$  GHz. Phase difference of each unit element at (b)  $f_i = 9.0$  GHz, and (c)  $f_i = 12.1$  GHz, with reference to the design frequency of  $f_o = 9.2$  GHz.

## 6.4 Results and Discussion

The fabricated prototype is measured using the measurement setup described in Section 5.3. The farfield distance  $R = 7.5$  m, and the reflectarray is directed facing  $+z$ , and it is rotated in the  $\theta$  direction to enable measurement of radiation patterns in all angles. Figure 6.11 shows the measured and simulated radiation patterns of the proposed reflectarray in  $E$ - ( $yz$ -plane) and  $H$ - ( $xz$ -plane) planes, respectively, at 9.2 GHz. As can be seen, the measured patterns show good agreement with the simulated ones. The measured sidelobe levels (SLL) are at least 15 dB lower than the main beam. It is also noted that the cross-polarized level is  $> 20$  dB lower than the co-polarised counterpart. The simulated  $H$ -plane cross-polarized fields are not plotted in Figure 6.11 (b), as all the data points are below -80 dB. The measured and simulated antenna gain together with the aperture efficiency of the proposed reflectarray, are plotted in Figure 6.12. It shows that the measured peak gain is 23.6 dBi at 9.3 GHz, corresponding to an aperture efficiency of 43.8% (simulation: 24.3 dBi, 52%). The proposed reflectarray can achieve a -1-dB gain bandwidth of 33.2%, covering 9.05 GHz – 12.1 GHz (simulation: 33.7% covering 9.0 GHz – 12.1 GHz). Moreover, the aperture efficiency can maintain above 25% within the -1-dB gain bandwidth. The discrepancy between the measured and simulated results can be caused by fabrication tolerances and misalignments, which are unavoidable during the experiment processes.



(a)



(b)

Figure 6.11: Measured and simulated (a) *E*- and (b) *H*-plane radiation patterns of the proposed reflectarray at 9.2 GHz.

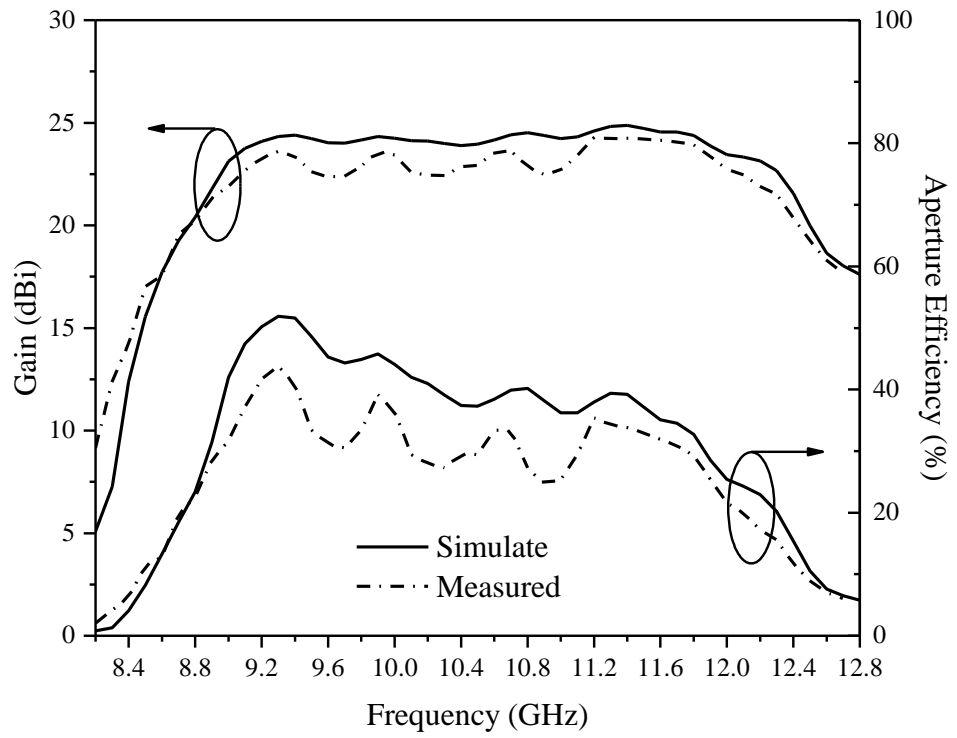


Figure 6.12: Measured and simulated antenna gains of the proposed reflectarray as a function of frequency.

## 6.5 Parametric Analysis

Parametric analysis is performed to study the characteristics of the proposed unit element and reflectarray to achieve optimum performance. Details of their analysis will be discussed in the following Section 6.5.1 and Section 6.5.2, respectively.

### 6.5.1 Unit Element Reflection Phase

To begin with, the incident angle ( $\theta_i$ ), slot width ( $S_w$ ), and air layer ( $h$ ) are analysed at  $f_0 = 9.2$  GHz to study their effects on the reflection phase responses. Figure 6.13 shows that the reflection phase curves are not sensitive to the incident angle up to  $30^\circ$ , which is desired for designing a reflectarray. As can be seen from Figure 6.14, the slot width does not affect the phase range much. Figure 6.15 shows that the reflection response varies with the air layer thickness. It can be seen that increasing the air layer thickness can improve the phase linearity and reflection loss. However, as the air thickness exceeds 4.7 mm, the phase linearity worsens, and the reflection loss increases. The optimum thickness is found to be 4 mm as it can provide good phase linearity with the lowest reflection loss.

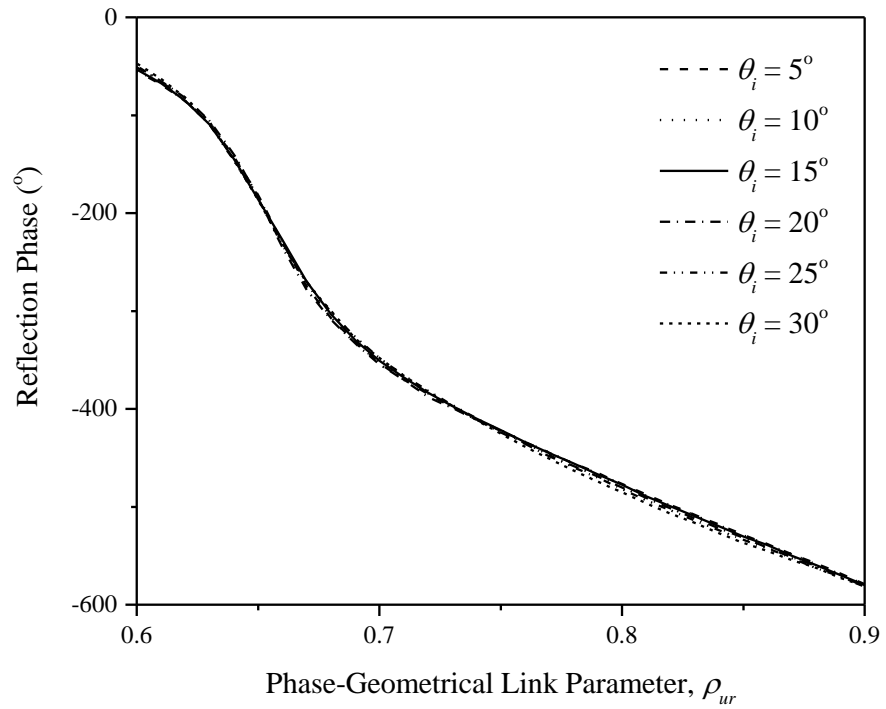


Figure 6.13: Effect of different incident angles ( $\theta_i$ ) on the reflection phase responses at  $f_o = 9.2$  GHz.

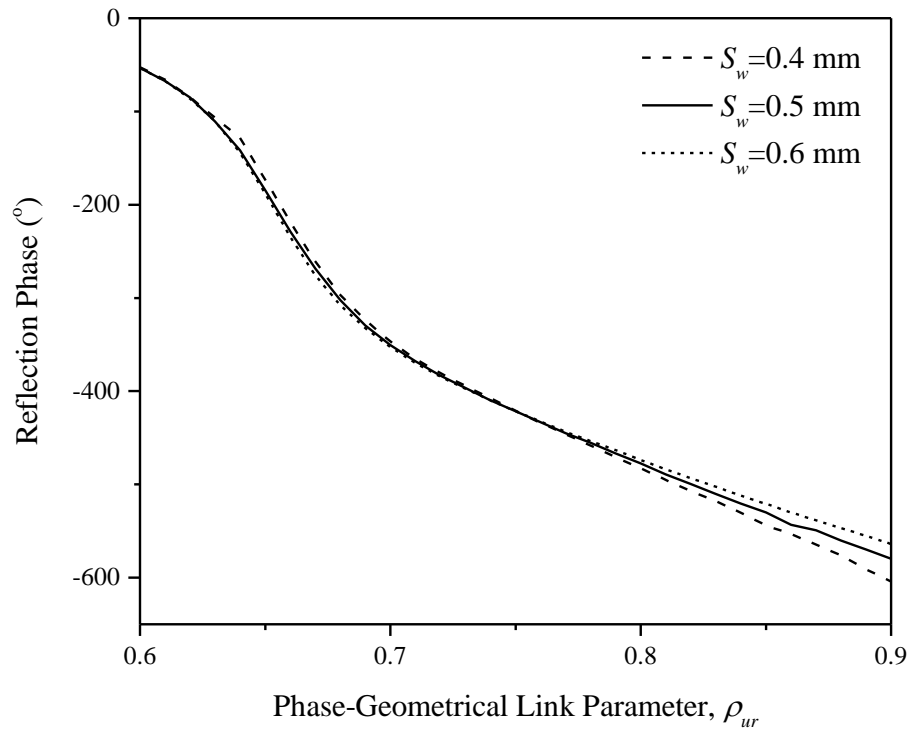


Figure 6.14: Effect of varying slot width,  $S_w$  on the reflection phase responses at  $f_o = 9.2$  GHz.

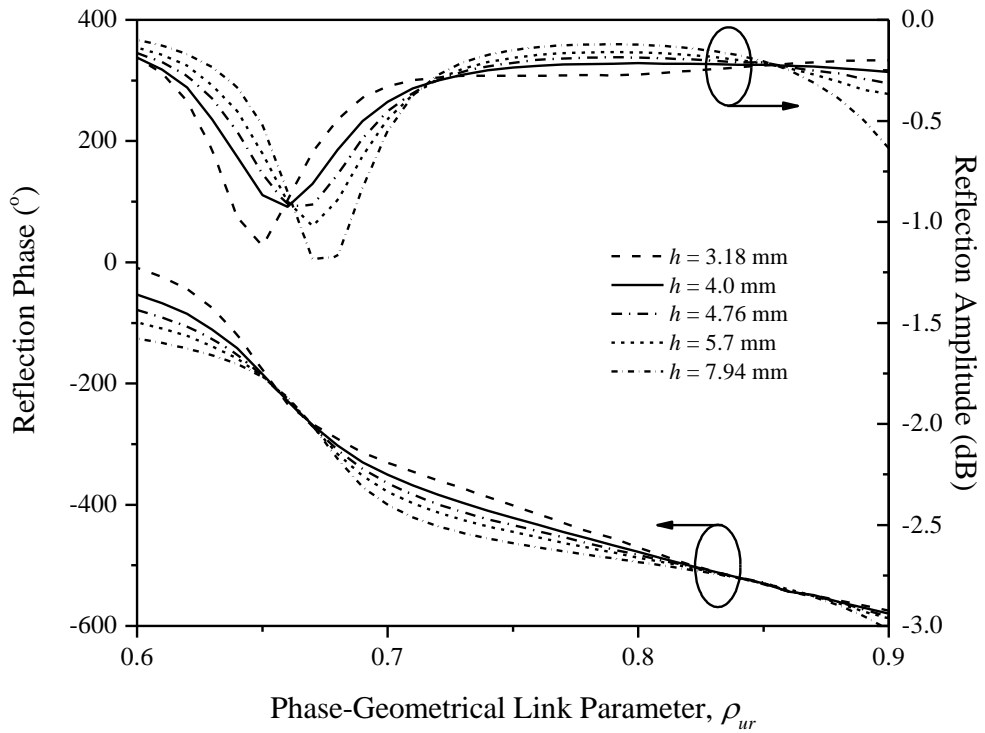
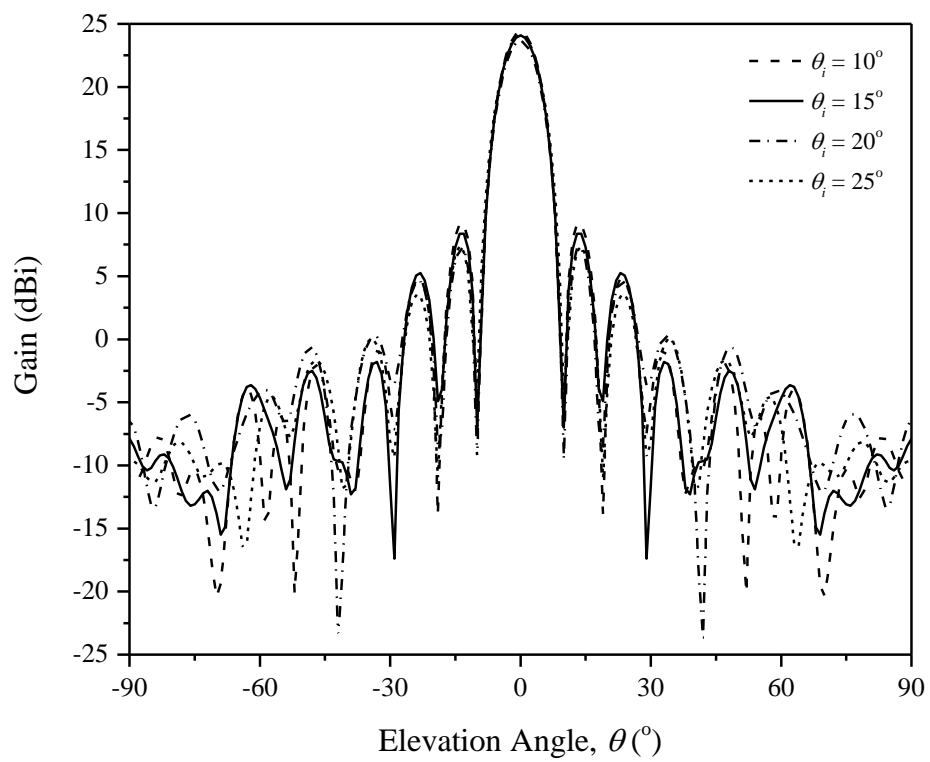


Figure 6.15: Effect of the air layer  $h$  on the reflection amplitude and phase responses at  $f_o = 9.2$  GHz.

### 6.5.2 Reflectarray Performance

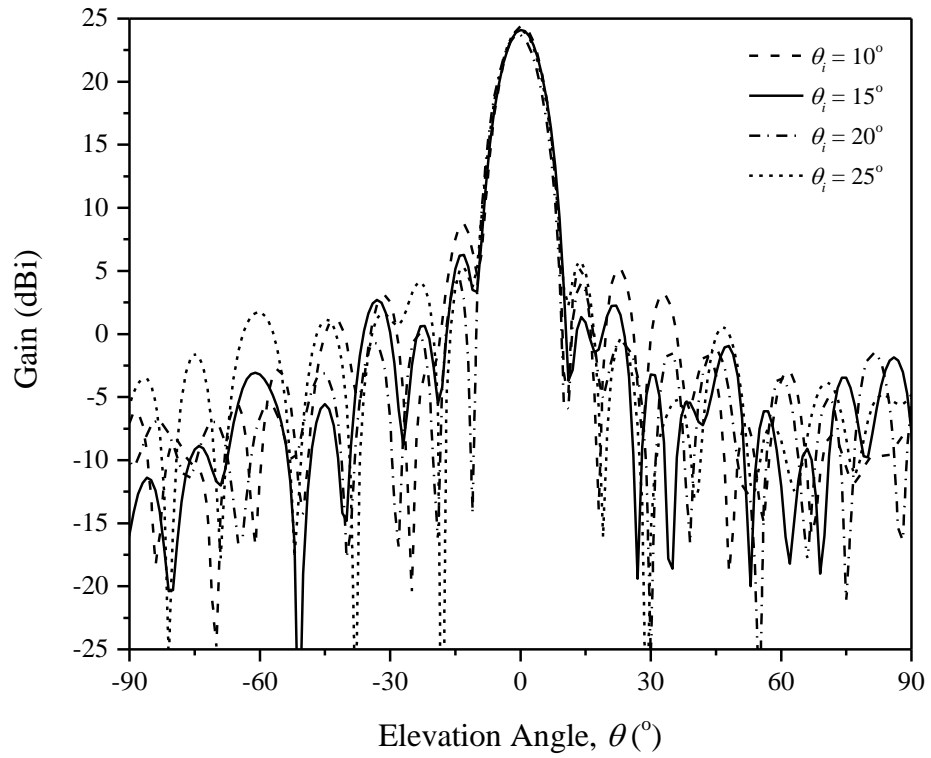
The performance of the proposed reflectarray on the radiation field at the design frequency  $f_o = 9.2$  GHz, as well as the gain-frequency relationship, are examined for various feed incident angles ( $\theta_i$ ) and focal ratios ( $F/D$ ). Figure 6.16 indicates that the main beam maintains almost similar for  $\theta_i \leq 25^\circ$  with a low side lobes level (SLL) of at least 15 dB. As seen in Figure 6.17, a lower incident angle provides wider gain bandwidth. A higher gain and aperture efficiency can be obtained when  $\theta_i = 10^\circ$ . However, due to the feed horn blockage, it introduces a higher SLL. Hence, the optimum -1-dB bandwidth of 33.7% is achievable at  $\theta_i = 15^\circ$  with an aperture efficiency of 52%. For the case of  $F/D$  on the radiation field, as shown in Figure 6.18, decreasing the  $F/D$  value

helps to improve the main beam gain accordingly. As seen in Figure 6.19, a closer feed distance improves the antenna gain and associated aperture efficiency. However, it has a relatively trivial effect on the antenna bandwidth. The antenna gain and aperture efficiency are optimum at the  $F/D$  ratio of 0.72. Further reduction in the  $F/D$  or feed distance does not improve the gain performance.



(a)





(b)

Figure 6.16: Simulated (a) *E*- and (b) *H*- plane radiation patterns of the proposed reflectarray at 9.2 GHz for different incident angles.

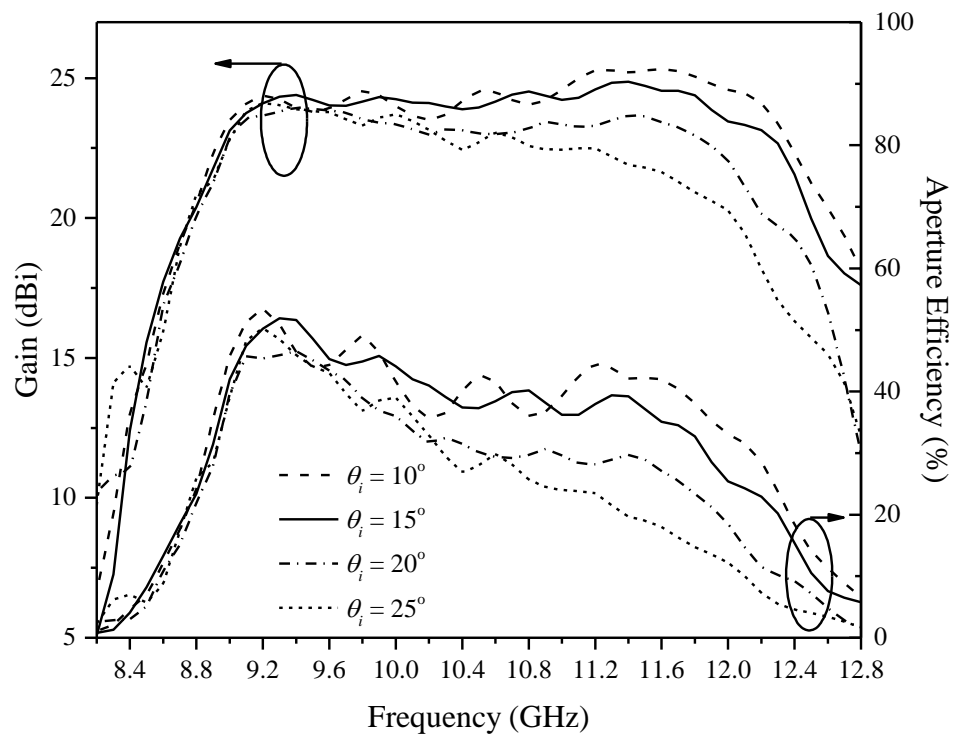
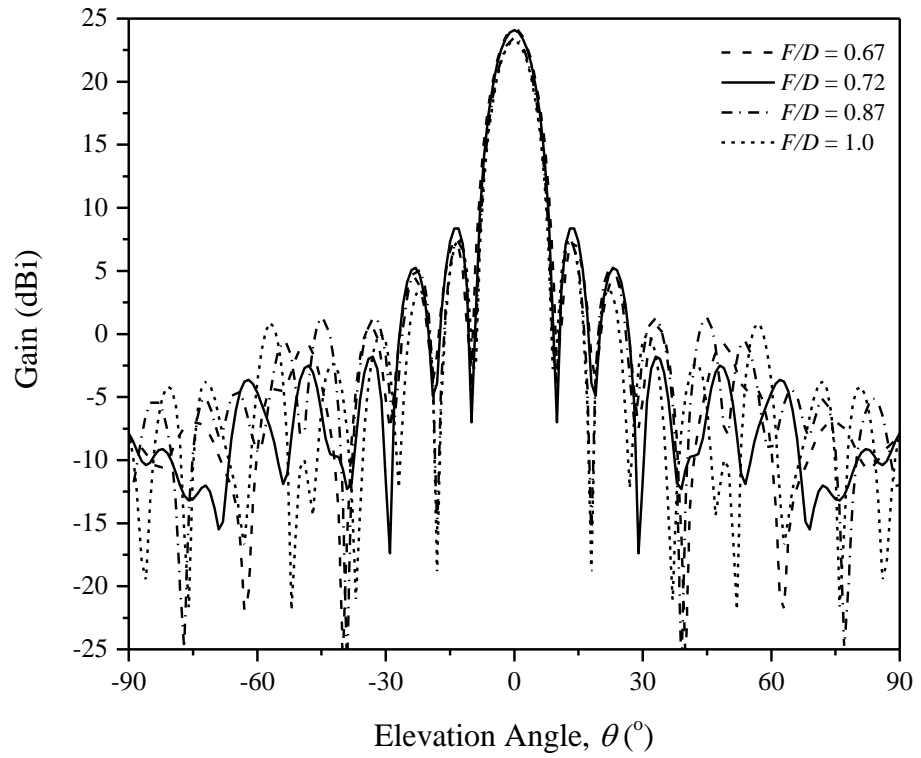
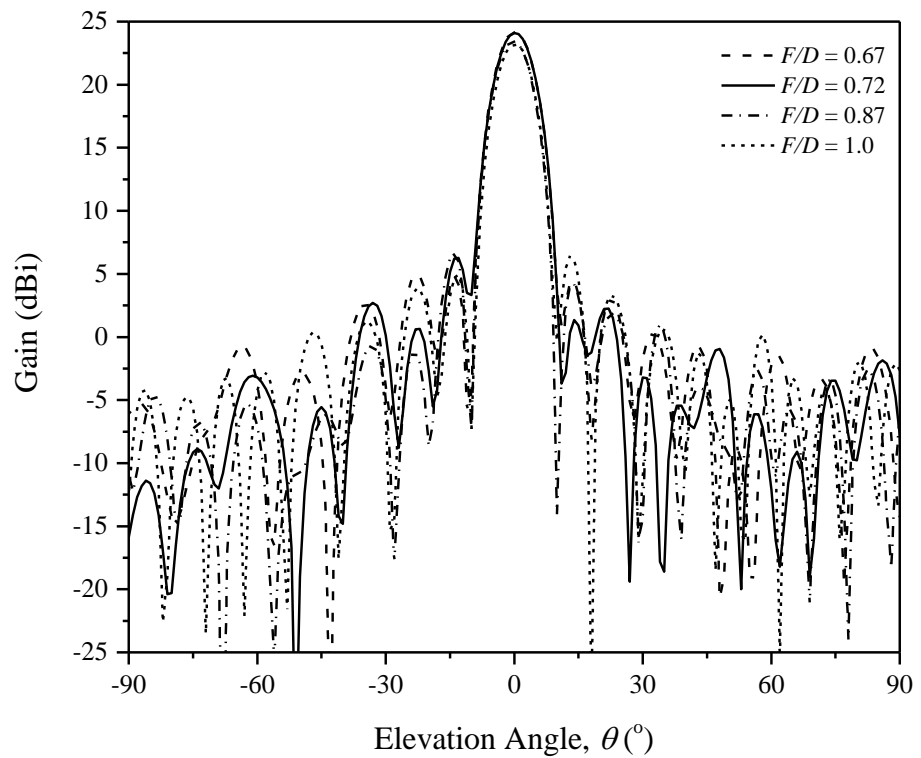


Figure 6.17: Simulated antenna gains of the proposed reflectarray as a function of frequency for different incident angles.



(a)



(b)

Figure 6.18: Simulated (a) *E*- and (b) *H*- plane radiation patterns of the proposed reflectarray at 9.2 GHz for different  $F/D$  ratios.

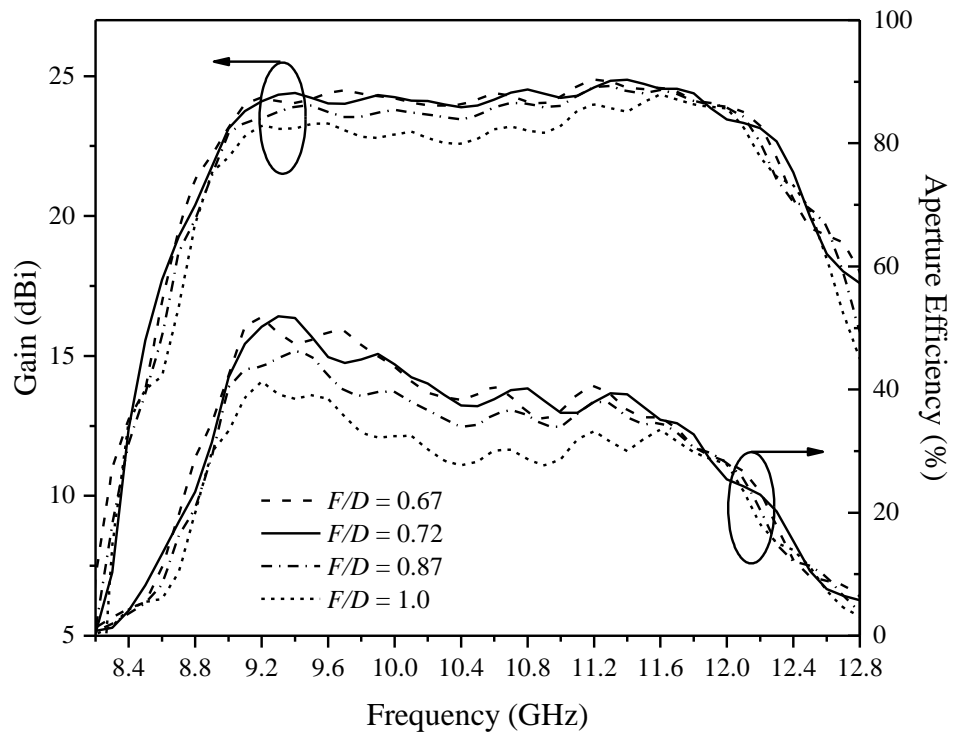


Figure 6.19: Simulated antenna gains of the proposed reflectarray as a function of frequency for different  $F/D$  ratios.

## 6.6 Comparative Study

Table 6.2 illustrates the comparison between the proposed reflectarray with other published X-band antennas. Superior performance is observed for the proposed double-layer reflectarray in terms of bandwidth and cross-polarization. Compared with the conventional patch type reflectarray (Encinar, 2001) and with that of enhanced performance (Mohammadi et al., 2018), the gain bandwidth of the proposed reflectarray shows significant superiority. The proposed reflectarray also outperforms in terms of -1-dB gain bandwidth when it is compared with those designed using the phase delay lines (Han et al., 2017; Su et al., 2019) and equal geometric elements (Nayeri et al., 2011; Ning et al., 2021). Results show that a reasonably wide bandwidth is achievable in this

proposed reflectarray. The proposed reflectarray has a small aperture size. It has a better or comparable performance in terms of gain bandwidth, aperture efficiency, sidelobe, and cross-polarization.

Table 6.2: Comparison of the Proposed Reflectarray Performance with Other Published Designs.

Ref. No.	This Work	(Han et al., 2017)	(Su et al., 2019)	(Mohammedi et al., 2018)	(Yu and Guo, 2019)	(Encinar, 2001)	(Ning et al., 2021)
Design Frequency [GHz]	9.2	10.0	8.5	10	10	11.95	10
Element Size [ $\lambda_0$ ]	0.54	0.47	0.43	0.33	0.3	0.56	0.3
Num. of Elements	169	277	225	~900	529	~685	1058
Phase Range [°]	527	600	360	423	~360	~400	~360
Aperture Size [ $\lambda$ ]	6.4	8.9	7.2	10.2	6.9	16.2	6.9
Layers	Double	single	Single	Single +FR4	Single	Double-stacked	Single
-1-dB Gain Bandwidth [%]	33.2	31.5	20.7	23.3	30	16.7	31
Peak Gain [dBi]	23.6	25.8	22.9	26.6	25	31	~26
Measured cross-Pol Level [dB]	<-30	<-26	<-24	-31.7	<-32	<-25	<-30
Measured Side Lobe Level [dB]	<-15	-20	<-13	-20.7	<-17.5	<-15	<-17
Maximum AE [%]	43.8	50	40	44.6	58.3	35	62.7

## 6.7 Conclusion

For the first time, a double-layer reflectarray structure built using two closely coupled inter-layer ring-patches has been proposed to design a broadband reflectarray. The inter-layer coupling has been employed for mitigating the mutual coupling between the reflectarray element. By properly designing the geometries and sizes of the ring-patches, the mutual coupling variation of the adjacent elements can be minimised. Here, the reflection phase curve of the reflectarray element is generated in a unique way from two linear equations that are related to the radii ( $R_{u1}$ ,  $R_{u2}$ ,  $R_{d1}$ ,  $R_{d2}$ ) of the top and bottom ring-patches. A broad and linear phase range of  $527^\circ$  with a reflection loss of less than 1 dB has been achieved. A phase optimisation scheme has been established with the employment of a cost function for optimising the reflection phase and amplitude across a large bandwidth. The proposed reflectarray can achieve an antenna gain of 23.6 dBi with a broad -1-dB gain bandwidth of 33.2%. It also has an aperture efficiency of 43.8%, with a cross-polarization level of  $< -30$  dB.

## CHAPTER 7

### CONCLUSIONS

#### 7.1 Summary

In the process of designing a reflectarray, it is crucial to obtain a good phase-shifting element that can provide a broad phase range with a linear phase curve, and it is responsible for achieving broad bandwidth and high efficiency. In this work, the design procedures for reflectarray elements and synthesis of full-fledged reflectarray have been established and laid out in detail. Three unique designs have been demonstrated to overcome the narrowband behaviour of the reflectarray elements and improve the broadband performance of the reflectarrays.

A novel reflectarray element is designed by combining a Vivaldi tapered slot antenna with a dumbbell-shaped microstrip ring resonator. The use of the travelling-wave radiator has enabled the proposed reflectarray element to achieve full phase range and low phase sensitivity simultaneously. A phase range of  $371^\circ$ , with a phase sensitivity of  $64.6^\circ/\text{mm}$ , is achieved. A linearly polarized  $13 \times 13$  reflectarray with an aperture size of 325 mm is designed and fabricated. The reflectarray is working in the C-band, and it has achieved an antenna gain of 24.1 dBi with a -1-dB bandwidth of 10.6%. It has also achieved 40.4% aperture efficiency. In addition, the antenna gain can be easily enhanced by elongating the profile length of the tapered slot antenna without the need to

increase the number of elements. Such advantages are not possible with the conventional reflectarray elements.

In order to further improve the phase tuning ability and achieve low profile configuration, a simple single-layer circular patch reflectarray element loaded with a pair of unequal slots is designed. This unique element design allows the linearity of the phase curve to be easily optimised by adjusting the ratio of the two unequal slots changeable according to a simple design equation. Such an approach provides more degrees of freedom to optimise the phase curve so that it can achieve a broad phase range with low phase sensitivity. Here, the patch radius has been employed as a phase-shifting geometrical parameter for generating a large phase range of  $458^\circ$  and a low reflection loss of less than 0.5 dB. In addition, the reflection phase curve can be made linear and smooth through the simple optimisation equation. A linearly polarized  $13 \times 13$  reflectarray with an aperture size of 208 mm is designed and fabricated. The reflectarray is operated in X-band, and a broad -1-dB gain bandwidth of 11.8% with an antenna gain of 23.4 dBi is realised. It has also achieved 42% aperture efficiency.

Lastly, a double-layer reflectarray structure that is built using two closely coupled inter-layer ring-patches is designed to enhance the bandwidth of the reflectarray. The inter-layer coupling has been employed for mitigating the mutual coupling between the reflectarray element. By properly designing the geometries and sizes of the ring-patches, the mutual coupling variation of the adjacent elements can be minimised. Here, the reflection phase curve of the

reflectarray element is generated in a unique way from two linear equations that are related to the radii ( $R_{u1}$ ,  $R_{u2}$ ,  $R_{d1}$ ,  $R_{d2}$ ) of the top and bottom ring-patches. The operational bandwidth of the phase-shifting element, which is responsible for the bandwidth performance of the reflectarray, can be further improved. A broad and linear phase range of  $527^\circ$  with a reflection loss of less than 1 dB has been achieved. A phase optimisation scheme has been established with the employment of a cost function for optimising the reflection phase and amplitude across a large bandwidth. A linearly polarized  $13 \times 13$  reflectarray with an aperture size of 208 mm is designed and fabricated. The reflectarray operates in the X-band and features a wider -1-dB bandwidth of 33.2%, with a maximum aperture efficiency of 43.8% and a low cross-polarization of  $< -30$  dB simultaneously.



## 7.2 Future Work

The use of microstrip technology is largely responsible for the rapid development in this research field. Finding new structures and materials for designing novel elements can still generate substantial interest in the research community, and it is foreseen to have an important role to play in the years to come.

Typically, the element design and the reflectarray synthesis can be performed using the commercial software packages, being benefited from the current high computing power. The advantage is that it can reduce the design cycle when developing the prototypes. Optimising the reflectarray element is crucial in the process of designing a full-fledged reflectarray. However, obtaining an optimum phase-shifting element is still a tedious and complex process. Therefore, one of the possible future works would be building customised machine-learning routines for analysing the phase responses and the element performance, such as the use of Particle Swarm Optimisation (Oliveri et al., 2019) and Genetic Algorithm (X. Chen et al., 2016). Such optimisation schemes can facilitate the design process significantly.

In this thesis, all the reflectarrays are designed with an offset feeding, and it reflects the main beam in the broadside direction. Due to the nature of the specular reflection from the ground plane is not in the same direction as the desired main beam, energy in these specular reflections will be wasted (Budhu and Rahmat-Samii, 2011). However, the desired main beam can be tilted away

from the boresight of the reflectarray aperture, which can fully take advantage of the specular reflection. This can be achieved by considering the progressive phase distribution in the phase shift calculation, which has been discussed in CHAPTER 2, Section 2.6. In addition, making the offset angle of the main beam equal to the feed offset angle has the advantage of minimizing the beam squint with frequency (Targonski and Pozar, 1996). Such consideration can be incorporated to enhance the reflectarray performance in the future.

Finally, a square aperture shape has been employed throughout the work due to fabrication simplicity. However, the nature of the spherical wavefront of the symmetric feed pattern cannot be matched to a square aperture shape, which limits the aperture efficiency. The aperture efficiency of the reflectarray antenna can be further enhanced by using a circular aperture (Nayeri et al., 2018). Hence, the current design method can be further improved by utilising the circular aperture in the future.

## REFERENCES

- Balanis, C.A., 2005. *Antenna theory: analysis and design* 3rd ed., John Wiley & Sons, Inc., Hoboken, NJ, USA.
- Berry, D., Malech, R. and Kennedy, W., 1963. The reflectarray antenna. *IEEE Transactions on Antennas and Propagation*, 11(6), pp.645–651.
- Bhattacharyya, A.K., 2005. *Phased array antennas: floquet analysis, synthesis, BFNS, and active array systems*, John Wiley & Sons, Inc., Hoboken, NJ, USA.
- Bialkowski, M.E. and Encinar, J.A., 2007. Reflectarrays: Potentials and Challenges. *International Conference on Electromagnetics in Advanced Applications. ICEAA 2007*. September 2007 pp. 1050–1053.
- Bialkowski, M.E. and Sayidmarie, K.H., 2008. Investigations into phase characteristics of a single-layer reflectarray employing patch or ring elements of variable size. *IEEE Transactions on Antennas and Propagation*, 56(11), pp.3366–3372.
- Bodur, H., Ünalı, S., Çimen, S. and Çakır, G., 2018. Broadband single-layer reflectarray antenna for X-band applications. *IET Microwaves, Antennas & Propagation*, 12(10), pp.1609–1612.
- Bozzi, M., Germani, S. and Perregrini, L., 2004. A figure of merit for losses in printed reflectarray elements. *IEEE Antennas and Wireless Propagation Letters*, 3(1), pp.257–260.
- Bozzi, M., Germani, S. and Perregrini, L., 2003. Performance comparison of different element shapes used in printed reflectarrays. *IEEE Antennas and Wireless Propagation Letters*, 2(1), pp.219–222.
- Budhu, J. and Rahmat-Samii, Y., 2011. Understanding the appearance of specular reflection in offset fed reflectarray antennas. *2011 IEEE International Symposium on Antennas and Propagation (APSURSI)*. July 2011 pp. 97–100.

- Carrasco, E., Barba, M. and Encinar, J.A., 2006. Aperture-coupled reflectarray element with wide range of phase delay. *Electronics Letters*, 42(12), p.667.
- Carrasco, E., Encinar, J.A. and Barba, M., 2008. Bandwidth Improvement in Large Reflectarrays by Using True-Time Delay. *IEEE Transactions on Antennas and Propagation*, 56(8), pp.2496–2503.
- Chaharmir, M.R., Shaker, J., Cuhaci, M. and Ittipiboon, A., 2006. Broadband reflectarray antenna with double cross loops. *Electronics Letters*, 42(2), pp.65–66.
- Chaharmir, M.R., Shaker, J., Cuhaci, M. and Sebak, A., 2003. Reflectarray with variable slots on ground plane. *IEE Proceedings - Microwaves, Antennas and Propagation*, 150(6), pp.436–439.
- Chaharmir, M.R., Shaker, J. and Legay, H., 2009. Broadband design of a single layer large reflectarray using multi cross loop elements. *IEEE Transactions on Antennas and Propagation*, 57(10), pp.3363–3366.
- Chang, D.C. and Huang, M.C., 1992. Microstrip reflectarray antenna with offset feed. *Electronics Letters*, 28(16), pp.1489–1491.
- Chang, K. and Hsieh, L.H., 2004. Ring antennas and frequency-selective surfaces. In: *Microwave Ring Circuits and Related Structures*. John Wiley & Sons, Inc., pp. 297–329.
- Chen, Q.Y. et al., 2013. An X-band reflectarray with novel elements and enhanced bandwidth. *IEEE Antennas and Wireless Propagation Letters*, 12, pp.317–320.
- Chen, X., Chen, Q., Feng, P. and Huang, K., 2016. Efficient design of the microstrip reflectarray antenna by optimizing the reflection phase curve. *International Journal of Antennas and Propagation*, 2016, p.e8764967.
- Chen, Z.N. et al. eds., 2016. *Handbook of antenna technologies*, Springer Nature, Singapore.

Costa, F. and Monorchio, A., 2012. Closed-form analysis of reflection losses in microstrip reflectarray antennas. *IEEE Transactions on Antennas and Propagation*, 60(10), pp.4650–4660.

CST MSW, *CST Studio Suite 3D EM simulation and analysis software, 3DS Dassault Systemes* [Online]. Available at: <https://www.3ds.com/products-services/simulia/products/cst-studio-suite/> [Accessed: 11 December 2021].

CST MSW VBA macro language, *CST MICROWAVE STUDIO VBA macro language* [Online]. Available at: [https://www.mathworks.com/products/connections/product\\_detail/cst-microwave-studio.html](https://www.mathworks.com/products/connections/product_detail/cst-microwave-studio.html) [Accessed: 30 January 2022].

Dahri, M.H. et al., 2020. Aspects of efficiency enhancement in reflectarrays with analytical investigation and accurate measurement. *Electronics*, 9(11), p.1887.

Encinar, J.A., 2001. Design of two-layer printed reflectarrays using patches of variable size. *IEEE Transactions on Antennas and Propagation*, 49(10), pp.1403–1410.

Encinar, J.A. and Zornoza, J.A., 2003. Broadband design of three-layer printed reflectarrays. *IEEE Transactions on Antennas and Propagation*, 51(7), pp.1662–1664.

Encinar, J.A. and Zornoza, J.A., 2004. Three-layer printed reflectarrays for contoured beam space applications. *IEEE Transactions on Antennas and Propagation*, 52(5), pp.1138–1148.

Eriksson, A., Linner, P. and Gevorgian, S., 2001. Mode chart of electrically thin parallel-plate circular resonators. *Microwaves, Antennas and Propagation, IEE Proceedings*, 148(1), pp.51–55.

Ethier, J., Chaharmir, M.R. and Shaker, J., 2012. Loss reduction in reflectarray designs using sub-wavelength coupled-resonant elements. *IEEE Transactions on Antennas and Propagation*, 60(11), pp.5456–5459.

- Gibson, P.J., 1979. The Vivaldi Aerial. *1979 9th European Microwave Conference*. September 1979 pp. 101–105.
- Han, C., Zhang, Y. and Yang, Q., 2017. A broadband reflectarray antenna using triple gapped rings with attached phase-delay lines. *IEEE Transactions on Antennas and Propagation*, 65(5), pp.2713–2717.
- Hasani, H., Kamyab, M. and Mirkamali, A., 2010. Broadband reflectarray antenna incorporating disk elements with attached phase-delay lines. *IEEE Antennas and Wireless Propagation Letters*, 9, pp.156–158.
- Huang, J., 1995a. Analysis of a microstrip reflectarray antenna for microspacecraft applications. *TDA Progress Report*, 153173. Available at: [ftp://www-a.agso.gov.au/geodesy-outgoing/vlbi/Documents/huang\\_1995.pdf](ftp://www-a.agso.gov.au/geodesy-outgoing/vlbi/Documents/huang_1995.pdf) [Accessed: 17 November 2014].
- Huang, J., 1995b. Bandwidth study of microstrip reflectarray and a novel phased reflectarray concept. *Antennas and Propagation Society International Symposium, 1995. AP-S. Digest*. June 1995 IEEE, pp. 582–585 vol.1.
- Huang, J., 1991. Microstrip reflectarray. *IEEE Antennas Propag. Soc. Int. Symp.* June 1991 London, Ont., Canada, pp. 612–615.
- Huang, J. and Encinar, J.A., 2008. *Reflectarray antennas*, John Wiley & Sons, Inc., Hoboken, NJ, USA.
- Huang, J. and Pogorzelski, R.J., 1998. A Ka-band microstrip reflectarray with elements having variable rotation angles. *IEEE Transactions on Antennas and Propagation*, 46(5), pp.650–656.
- Karnati, K., Ebadi, S. and Gong, X., 2012. Effects of inter-element spacing on mutual coupling and resonant properties in reflectarray unit cell design. *2012 IEEE Radio and Wireless Symposium (RWS)*. January 2012 pp. 83–86.
- Lee, S.R., Lim, E.H. and Lo, F.L., 2017. Broadband single-layer E-patch reflectarray. *Radioengineering*, 26(1), pp.97–106.

- Li, J.F., Chen, Q., Yuan, Q.W. and Sawaya, K., 2011. Reflectarray element using interdigital gap loading structure. *Electronics Letters*, 47(2), p.83.
- Li, Q.Y., Jiao, Y.C. and Zhao, G., 2009. A novel microstrip rectangular-patch/ring- combination reflectarray element and its application. *IEEE Antennas and Wireless Propagation Letters*, 8, pp.1119–1122.
- Liu, Y., Wang, H., Xue, F. and Dong, X., 2017. A new single-layer reflectarray using circular patch with semicircular ring slots. *Progress In Electromagnetics Research Letters*, 66, pp.105–111.
- Lo, Y.T. and Lee, S.W., 1993. *Antenna Handbook: Antenna Fundamentals and Mathematical Techniques*, Springer, US.
- Mailloux, R.J., 2005. *Phased array antenna handbook* 2nd ed., Artech House, Boston, London.
- Malagisi, C.S., 1978. Microstrip disc element reflect array. *Electronics and Aerospace Systems Convention, EASCON '78*. 1 January 1978 Institute of Electrical and Electronics Engineers, Inc., Arlington, Va., pp. 186-192.
- Malfajani, R.S. and Atlasbaf, Z., 2014. Design and implementation of a dual-band single layer reflectarray in X and K bands. *IEEE Transactions on Antennas and Propagation*, 62(8), pp.4425–4431.
- Mohammadi, B. et al., 2018. Enhanced reflectarray antenna using elements with reduced reflection phase sensitivity. *IEEE Antennas and Wireless Propagation Letters*, 17(7), pp.1334–1338.
- Moustafa, L. et al., 2011. The phoenix cell: a new reflectarray cell with large bandwidth and rebirth capabilities. *IEEE Antennas and Wireless Propagation Letters*, 10, pp.71–74.
- Munson, R.E., Haddad, H.A. and Hanlen, J.W., 1987. *Microstrip reflectarray for satellite communication and radar cross-section enhancement or reduction*, US4684952A

- Nasimuddin, Esselle, K. and Verma, A.K., 2005. Fast and accurate model for circular microstrip antennas on suspended and composite substrates. *IEEE Transactions on Antennas and Propagation*, 53(9), pp.3097–3100.
- Nayeri, P., Elsherbeni, A.Z. and Yang, F., 2013. Radiation analysis approaches for reflectarray antennas. *IEEE Antennas and Propagation Magazine*, 55(1), pp.127–134.
- Nayeri, P., Yang, F. and Elsherbeni, A.Z., 2011. Bandwidth improvement of reflectarray antennas using closely spaced elements. *Progress In Electromagnetics Research C*, 18, pp.19–29.
- Nayeri, P., Yang, F. and Elsherbeni, A.Z., 2010. Broadband reflectarray antennas using double-layer subwavelength patch elements. *IEEE Antennas and Wireless Propagation Letters*, 9, pp.1139–1142.
- Nayeri, P., Yang, F. and Elsherbeni, A.Z., 2018. *Reflectarray antennas: theory, designs, and applications*, John Wiley & Sons, Inc., Chichester, UK.
- Ning, P., Min, M., Guo, L. and Feng, W., 2021. On the use of half-cut elements for single-layer wideband reflectarrays. *IEEE Antennas and Wireless Propagation Letters*, 20(6), pp.943–947.
- Oh, S.W., Ahn, C.H. and Chang, K., 2009. Reflectarray element using variable ring with slot on ground plane. *Electronics Letters*, 45(24), pp.1206–1207.
- Oliveri, G., Salucci, M., Gelmini, A. and Massa, A., 2019. Computationally-Efficient Synthesis of Advanced Reflectarrays through a System-by-Design Tool. *13th European Conference on Antennas and Propagation (EuCAP 2013)*. March 2019 pp. 1–4.
- Pozar, D.M., 2003. Bandwidth of reflectarrays. *Electronics Letters*, 39(21), p.1490.
- Pozar, D.M. and Metzler, T.A., 1993. Analysis of a reflectarray antenna using microstrip patches of variable size. *Electronics Letters*, 29(8), pp.657–658.



Pozar, D.M., Targonski, S.D. and Syrigos, H.D., 1997. Design of millimeter wave microstrip reflectarrays. *IEEE Transactions on Antennas and Propagation*, 45(2), pp.287–296.

Rajagopalan, H. and Rahmat-Samii, Y., 2010. On the reflection characteristics of a reflectarray element with low-loss and high-loss substrates. *IEEE Antennas and Propagation Magazine*, 52(4), pp.73–89.

Rajagopalan, H., Xu, S. and Rahmat-Samii, Y., 2012. On Understanding the Radiation Mechanism of Reflectarray Antennas: An Insightful and Illustrative Approach. *IEEE Antennas and Propagation Magazine*, 54(5), pp.14–38.

Sakotic, Z., Crnojevic-Bengin, V. and Jankovic, N., 2017. Compact circular-patch-based bandpass filter for ultra-wideband wireless communication systems. *AEU - International Journal of Electronics and Communications*, 82, pp.272–278.

Sayidmarie, K.H. and Bialkowski, M.E., 2011. Fractal unit cells of increased phasing range and low slopes for single-layer microstrip reflectarrays. *IET Microwaves, Antennas and Propagation*, 5(11), pp.1371–1379.

Schaubert, D.H. et al., 1985. Endfire tapered slot antennas on dielectric substrates. *IEEE Transactions on Antennas and Propagation*, 33(12), pp.1392–1400.

Shin, J. and Schaubert, D.H., 1999. A parameter study of stripline-fed Vivaldi notch-antenna arrays. *IEEE Transactions on Antennas and Propagation*, 47(5), pp.879–886.

Stutzman, W.L. and Thiele, G.A., 1998. *Antenna theory and design* 2nd ed., John Wiley & Sons, Inc., New York.

Su, T., Yi, X. and Wu, B., 2019. X/Ku dual-band single-layer reflectarray antenna. *IEEE Antennas and Wireless Propagation Letters*, 18(2), pp.338–342.

Sze, K.Y. and Shafal, L., 1998. Analysis of phase variation due to varying patch length in a microstrip reflectarray. *IEEE Antennas and Propagation Society*

*International Symposium, 1998*. June 1998 IEEE, Atlanta, GA, USA, pp. 1134–1137.

Tahseen, M.M. and Kishk, A.A., 2017. C-Band Linearly Polarised Textile-Reflectarray (TRA) Using Conductive Thread. *IET Microwaves, Antennas and Propagation*, 11(7), pp.982–989.

Targonski, S.D. and Pozar, D.M., 1996. Minimization of beam squint in microstrip reflectarrays using an offset feed. *Antennas and Propagation Society International Symposium, 1996. AP-S. Digest*. 1996 IEEE, Baltimore, MD, USA, pp. 1326–1329.

Tienda, C. et al., 2013. Design, manufacturing and test of a dual-reflectarray antenna with improved bandwidth and reduced cross-polarization. *IEEE Transactions on Antennas and Propagation*, 61(3), pp.1180–1190.

Vosoogh, A., Keyghobad, K., Khaleghi, A. and Mansouri, S., 2014. A high-efficiency Ku-band reflectarray antenna using single-layer multiresonance elements. *IEEE Antennas and Wireless Propagation Letters*, 13, pp.891–894.

Wang, M., Wu, W. and Shen, Z., 2010. Bandwidth enhancement of antenna arrays utilizing mutual coupling between antenna elements. *International Journal of Antennas and Propagation*, 2010, p.e690713.

Wang, S. et al., 2008. Design of compact broadband TSA arrays by using element mutual coupling. *Electronics Letters*, 44(18), pp.1049–1051.

Wolff, I. and Knoppik, N., 1974. Rectangular and circular microstrip disk capacitors and resonators. *IEEE Transactions on Microwave Theory and Techniques*, 22(10), pp.857–864.

Wu, G. et al., 2018. Reflectarray antenna design with arbitrary incident and reflection beam angle. *IEEE Transactions on Antennas and Propagation*, pp.1–1.

Xia, X. et al., 2017. Wideband millimeter-wave microstrip reflectarray using dual-resonance unit cells. *IEEE Antennas and Wireless Propagation Letters*, 16, pp.4–7.

Yang, X. et al., 2018. A mechanically reconfigurable reflectarray with slotted patches of tunable height. *IEEE Antennas and Wireless Propagation Letters*, 17(4), pp.555–558.

Yoon, J.H. et al., 2014. Single-layer reflectarray with combination of element types. *Electronics Letters*, 50(8), pp.574–576.

Yoon, J.H., Yoon, Y.J., Lee, W. and So, J., 2015. Square ring element reflectarrays with improved radiation characteristics by reducing reflection phase sensitivity. *IEEE Transactions on Antennas and Propagation*, 63(2), pp.814–818.

Yu, A. et al., 2010. Aperture efficiency analysis of reflectarray antennas. *Microwave and Optical Technology Letters*, 52(2), pp.364–372.

Yu, H. and Guo, L., 2019. Broadband single-layer reflectarray antenna employing circular ring elements dented with sectorial slits. *IEEE Access*, 7, pp.165814–165819.